Chromosome organization by one-sided and two-sided loop extrusion

Edward J. Banigan[1,2]*, Aafke A. van den Berg[1,2]*, Hugo B. Brandão[3,]*, John F. Marko[4], and Leonid A. Mirny[1,2,†]

[1]Institute for Medical Engineering & Science, Massachusetts Institute of Technology

[2]Department of Physics, Massachusetts Institute of Technology

[3]Harvard Graduate Program in Biophysics, Harvard University

[4]Departments of Molecular Biosciences and Physics & Astronomy, Northwestern University

*These authors contributed equally

[†]To whom correspondence should be addressed: leonid@mit.edu

Abstract

SMC complexes organize chromatin throughout the cell cycle across many cell types. Experiments indicate that this is achieved by an energy-consuming process known as loop extrusion, in which SMC complexes, such as condensin or cohesin, reel in DNA/chromatin, extruding and progressively growing a DNA/chromatin loop. Theoretical modeling assuming two-sided loop extrusion has successfully reproduced key features of chromatin organization across different organisms. Recent *in vitro* single-molecule experiments confirmed that yeast condensins extrude loops. However, condensins remain anchored to their initial loading sites, so that they extrude loops in an asymmetric, “one-sided” manner. This raises the question of whether such “one-sided” complexes are able to perform the many functions that are commonly attributed to “two-sided” loop-extruding factors *in vivo*, such as mitotic chromosome compaction, interphase topologically associated domain formation, and bacterial chromosomal arm juxtaposition. We simulated one-sided loop extrusion and its variants in 3D models of chromosome organization in these scenarios. We found that while pure one-sided loop extrusion is unable to reproduce these phenomena, variants of one-sided extrusion that approximate two-sided extrusion can recover *in vivo* observations. We propose experiments that can test our quantitative predictions, and we predict that SMC complexes *in vivo* may constitute effectively two-sided motors and/or exhibit biased loading. Our work suggests that loop extrusion remains a viable general mechanism of chromatin organization.

Introduction

Structural Maintenance of Chromosomes (SMC) complexes are ring-like protein complexes that are integral to chromosome organization in organisms ranging from bacteria to humans. SMC complexes linearly compact mitotic chromosomes in eukaryotic cells (Gibcus et al., 2018; Hirano et al., 1997; Hirano and Mitchison, 1994; Ono et al., 2003; Shintomi et al., 2017, 2015), maintain topologically associated domains (TADs) in interphase mammalian cells (Gassler et al., 2017; Haarhuis et al., 2017; Rao et al., 2017; Sanborn et al., 2015; Schwarzer et al., 2017;

Wutz et al., 2017), and juxtapose the arms of circular chromosomes in bacteria (Marbouty et al., 2015; Tran et al., 2017; Wang et al., 2017, 2015). In each of these processes, SMC complexes form chromatin loops. These diverse chromosome phenomena are hypothesized to be driven by a common underlying physical mechanism by which SMC complexes processively extrude chromatin or DNA loops (Alipour and Marko, 2012; Bürmann and Gruber, 2015; Fudenberg et al., 2017, 2016; Goloborodko et al., 2016a, 2016b; Nasmyth, 2001; Riggs, 1990; Sanborn et al., 2015; Wang et al., 2017, 2015). However, it is not known what molecular-level requirements loop extrusion must satisfy in order to robustly reproduce the 3D chromosome structures observed in these *in vivo* phenomena.

The loop extrusion model posits that a loop-extruding factor (LEF), such as condensin, cohesin, or a bacterial SMC complex (bSMC) is comprised in part by two connected motor subunits that bind to chromatin and form a small chromatin loop by bridging two proximal chromatin segments. The SMC complex progressively enlarges the loop by reeling chromatin from outside the loop into the growing loop (Alipour and Marko, 2012; Nasmyth, 2001; Riggs, 1990). To reel in chromatin from both sides of the complex, each motor subunit of the LEF translocates in opposite directions, away from the initial binding site (Alipour and Marko, 2012; Fudenberg et al., 2016; Goloborodko et al., 2016a, 2016b; Sanborn et al., 2015). This “two-sided” extrusion model recapitulates experimental observations of mitotic chromosome compaction and resolution, interphase TAD and loop formation, and juxtaposition of bacterial chromosome arms (Alipour and Marko, 2012; Fudenberg et al., 2016; Goloborodko et al., 2016a, 2016b; Miermans and Broedersz, 2018; Sanborn et al., 2015; Wang et al., 2017, 2015). However, until recently, loop extrusion by SMC complexes had not been directly observed.

Recent *in vitro* single-molecule experiments have imaged loop extrusion of DNA by individual SMC condensin complexes, demonstrating that yeast and human condensin complexes extrude DNA loops in an ATP-dependent, directed manner at speeds of order 1 kb/s. Strikingly, however, yeast condensins (Ganji et al., 2018) and a significant fraction of human condensins (Kong et al., 2019) reel in DNA from only one side, while the other side remains anchored to its DNA loading site. This contrasts with prior observations in bacteria demonstrating the direct involvement of SMC complexes in two-sided loop extrusion *in vivo* (Tran et al., 2017; Wang et al., 2017). One-sided extrusion also conflicts with existing versions of the loop extrusion model, which generally assume that extrusion is two-sided (Alipour and Marko, 2012; Fudenberg et al., 2016; Goloborodko et al., 2016a, 2016b; Miermans and Broedersz, 2018; Sanborn et al., 2015). Furthermore, recent theoretical work shows that purely “one-sided” loop extrusion, as it has been observed *in vitro* so far, is intrinsically far less effective in linearly compacting DNA than two-sided extrusion (Banigan and Mirny, 2019). Thus, we investigated the extent to which one-sided loop extrusion might impact the 3D structure of chromosomes and whether variants of one-sided loop extrusion can recapitulate *in vivo* observations. In particular, we focus on three chromosome organization phenomena driven by SMC complexes: 1) mitotic chromosome compaction and resolution, 2) interphase chromosome domain formation, and 3) juxtaposition of bacterial chromosome arms.

Mitotic chromosome compaction and resolution- The SMC condensin complex in eukaryotes plays a central role in mitotic chromosome compaction and segregation (Charbin et al., 2014; Hagstrom et al., 2002; Hirano, 2016; Hirano et al., 1997; Hirano and Mitchison, 1994; Hudson et al., 2003; Nagasaka et al., 2016; Ono et al., 2003; Piskadlo et al., 2017; Saka et al., 1994; Shintomi et al., 2017, 2015; Steffensen et al., 2001; Strunnikov et al., 1995). In mitotic chromosomes, electron microscopy reveals that chromatin is arranged in arrays of loops (Earnshaw and Laemmli, 1983; Maeshima et al., 2005; Marsden and Laemmli, 1979; Paulson and Laemmli, 1977). This results in dramatic linear compaction of the chromatin fiber into a polymer brush with a >100-fold shorter backbone (Guacci et al., 1994; Lawrence et al., 1988). Fluorescence imaging and Hi-C show that these loops maintain the linear ordering of the genome (Gibcus et al., 2018; Naumova et al., 2013; Trask et al., 1993). Together, these features may facilitate the packaging, resolution, and segregation of chromosomes during mitosis by effectively shortening and disentangling chromatids (Brahmachari and Marko, 2019; Eykelenboom et al., 2019; Goloborodko et al., 2016a; Green et al., 2012; Marko, 2009; Nagasaka et al., 2016; Sakai et al., 2018, 2016). Each of these experimental observations is reproduced by the two-sided loop extrusion model, in which dynamic loop-extruding condensins collectively form arrays of reinforced loops by locally extruding chromatin until encountering another condensin (Goloborodko et al., 2016a, 2016b). The simplest one-sided loop extrusion process, in contrast, can only linearly compact chromosomes 10-fold because it leaves unlooped (and thus, uncompacted) polymer gaps between loop extruders (Banigan and Mirny, 2019); it is unclear whether 10-fold compaction is sufficient for robust chromosome segregation. Nonetheless, variants of one-sided loop extrusion in which loop extruders are effectively two-sided may robustly compact mitotic chromosomes (Banigan and Mirny, 2019). This raises the question of what abilities an individual one-sided loop extruder must possess to compact and spatially resolve chromosomes.

Interphase domain formation- In interphase in vertebrate cells, Hi-C reveals that the SMC cohesin complex is responsible for frequent but transient loop formation, which results in regions of high intra-chromatin contact frequency referred to as TADs (Dixon et al., 2012; Gassler et al., 2017; Haarhuis et al., 2017; Nora et al., 2012; Rao et al., 2017, 2014; Schwarzer et al., 2017; Sexton et al., 2012; Sofueva et al., 2013). These regions are bordered by convergently oriented CTCF protein binding sites (de Wit et al., 2015; Guo et al., 2015; Rao et al., 2014; Sanborn et al., 2015; Vietri Rudan et al., 2015), which may act as obstacles to loop extrusion and translocation of cohesin (Busslinger et al., 2017; de Wit et al., 2015; Fudenberg et al., 2016; Nora et al., 2017; Sanborn et al., 2015; Wutz et al., 2017). The two-sided loop extrusion model explains the emergence of TADs and their “corner peaks” (or “dots”) and “stripes” in Hi-C maps as an average collective effect of multiple cohesins dynamically extruding chromatin loops and stopping at the CTCF boundaries (Fudenberg et al., 2016; Sanborn et al., 2015) (reviewed in (Fudenberg et al., 2017)). Existing models for loop extrusion during interphase have assumed LEFs with two mobile subunits, whether they be active or inactive (Alipour and Marko, 2012; Benedetti et al., 2017; Brackley et al., 2017; Fudenberg et al., 2016; Sanborn et al., 2015; Yamamoto and Schiessel, 2017). While it is clear that a one-sided LEF will necessarily leave an unlooped gap between its initial loading site and one of the CTCF

boundary elements, the extent to which one-sided loop extrusion can recapitulate the experimental observations remains entirely unexplored.

Bacterial chromosome arm juxtaposition- In bacteria, SMC complexes and homologs play an important role in the maintenance of proper chromosome organization and efficient chromosomal segregation ((Britton et al., 1998; Jensen and Shapiro, 1999; Moriya et al., 1998; Sullivan et al., 2009) and others). In *Bacillus subtilis* and *Caulobacter crescentus*, the circular chromosome exhibits enhanced contact frequency between its two chromosomal arms (often called “replichores”), as shown by Hi-C (Le et al., 2013; Marbouty et al., 2015). This signal is dependent on the bacterial SMC complex (bSMC) (Marbouty et al., 2015; Wang et al., 2015). Experiments show that bSMC is loaded at a bacterial *parS* site near the origin of replication, and then, while bridging the two arms, actively and processively moves along the chromosome, thus juxtaposing or “zipping” the arms together (Minnen et al., 2016; Tran et al., 2017; Wang et al., 2018, 2017). The symmetry of the juxtaposed chromosome arms implies that bSMC should be a two-sided LEF (Brandão et al., 2019; Wang et al., 2017). Indeed, previous modeling has shown that pure one-sided loop extrusion produces contact maps that differ from experimental observations (Miermans and Broedersz, 2018). However, it is unknown whether variations of one-sided extrusion can properly juxtapose the arms of a circular bacterial chromosome.

Two-sided loop extrusion models (Brandão et al., 2019; Fudenberg et al., 2017, 2016; Goloborodko et al., 2016a, 2016b; Sanborn et al., 2015) can account for the various chromosome organization phenomena described above, but *in vitro* single-molecule experiments suggest that at least some SMC complexes are one-sided LEFs. We therefore investigate whether a mechanism of one-sided loop extrusion can account for *in vivo* observations of 3D chromatin organization, as listed above, namely vertebrate mitotic chromosome compaction and resolution, interphase chromatin organization in higher eukaryotes, and juxtaposition of bacterial chromosome arms. To study these processes, we construct a model for one-sided loop extrusion and simulate the collective dynamics of SMC complexes and chromatin in these three distinct scenarios. We also explore several one-sided extrusion variants. By comparing our results to experimental data, we find that pure one-sided loop extrusion fails to capture *in vivo* phenomenology. However, simple variants of the one-sided model that make loop extrusion effectively two-sided or otherwise suppress the formation of unlooped chromatin gaps can restore the emergent features of chromatin organization observed in experiments.

Model

Model for loop extrusion

In our model, loop extrusion is performed by loop-extruding factors (LEFs), which may be a single SMC complex, a dimer of SMC complexes, or any other oligomer of SMC complexes. A LEF is comprised of two subunits, which can either be active or inactive. Each active subunit

can processively translocate along the chromatin fiber, thus creating and enlarging the chromatin (or DNA) loop between the subunits (**Figure 1 a**). An inactive subunit can either be anchored or passively slide/diffuse along the fiber, depending on the specific model (see below).

In existing simulation models of loop extrusion (Alipour and Marko, 2012; Brandão et al., 2019; Fudenberg et al., 2016; Goloborodko et al., 2016a, 2016b; Miermans and Broedersz, 2018; Sanborn et al., 2015), LEFs are "two-sided," *i.e.*, they have two active subunits that on average grow a chromatin loop by translocating in opposing directions (**Figure 1 b**). Here, we consider "one-sided" LEFs that have one active subunit and one inactive (passive) subunit.

LEFs in our one-sided extrusion model have binding and translocation dynamics that mimic turnover and translocation of SMC complexes, as has been observed in experiments (Ganji et al., 2018; Gerlich et al., 2006a, 2006b; Hansen et al., 2017; Kleine Borgmann et al., 2013; Stigler et al., 2016; Terakawa et al., 2017; Tran et al., 2017; Walther et al., 2018; Wang et al., 2017). In our model, LEFs bind to chromatin with association rate k_{bind} and unbind from chromatin with dissociation rate k_{unbind} (mean residence time $\tau=1/k_{\text{unbind}}$). A LEF's active subunit translocates at speed v along the chromosome, away from its passive subunit, thus growing the chromatin loop. Furthermore, LEF subunits cannot translocate through other LEF subunits unless otherwise stated; extrusion by an active LEF subunit halts when it encounters another LEF subunit. Extrusion may continue if the obstacle is removed (for example, by unbinding). This constraint is relaxed for one model variant, as described in the Results section.

The pure one-sided and two-sided loop-extrusion models are primarily controlled by two length scales, λ and d (Banigan and Mirny, 2019; Fudenberg et al., 2016; Goloborodko et al., 2016b). The LEF processivity λ is given by $\lambda=qv/k_{\text{unbind}}$, where q=1 or 2 for one- and two-sided, respectively; thus, one-sided LEFs with extrusion velocity v grow loops at half the speed of two-sided LEFs with the same v (see arch diagrams in **Figure 1 b** and **c,** bottom). $d=L/N_b$, is the mean distance between the N_b LEFs bound to the fiber of length L (where $N_b=N\,k_{\text{bind}}/(k_{\text{bind}}+k_{\text{unbind}})$). For $\lambda<d$, LEFs are sparse and on average do not meet. For $\lambda>d$, LEFs are densely loaded on the chromatin, and a translocating LEF typically encounters other LEFs.

While there are many possible variants of the one-sided loop extrusion model, we mainly focus on three general variants of one-sided loop extrusion that differ by LEF subunit translocation dynamics.

Pure one-sided extrusion

In pure one-sided loop extrusion, the passive subunit of the bound LEF remains stationary on the chromatin fiber for the entire residence time of the LEF, while the active subunit translocates at speed v away from the passive subunit. LEFs bind with a random orientation. Individual LEFs asymmetrically extrude loops, as observed in (Ganji et al., 2018). **Figure 1 c** shows a typical trajectory and corresponding arch diagram for LEF subunits in the pure one-sided extrusion model.

Semi-diffusive model

We also considered a model in which the active LEF subunit translocates at speed v, while the inactive LEF subunit stochastically diffuses (slides) along the fiber. This model is motivated by the experimental observation of the yeast condensin "safety belt" (Kschonsak et al., 2017). This condensin component is thought to anchor the LEF in place as it extrudes loops in a one-sided manner, but the safety belt can be released via protein alterations (Ganji et al., 2018; Kschonsak et al., 2017). The inactive subunit stochastically translocates by taking diffusive steps in either direction. The stepping rate in each direction is modulated by the entropic penalty for polymer loop formation (see Methods). As a result of this effect, the sliding tends to shrink small loops, while having little effect on large loops. A typical trajectory and arch diagram for the subunits of a semi-diffusive LEF are shown in **Figure 1 d**.

To evaluate the importance of passive extrusion as compared to active extrusion, we study loop extrusion as a function of the scaled diffusive stepping rate. This quantity is the ratio, v_{diff}/v, of the characteristic diffusive stepping rate, v_{diff}, to the active loop extrusion speed, v. $v_{diff}/v<1$ indicates that diffusive stepping is slow as compared to active stepping, while $v_{diff}/v>1$ indicates that diffusive stepping is relatively rapid**.**

Switching model

As another alternative model, we consider a scenario in which LEFs are instantaneously one-sided (*i.e.*, one subunit is active and the other is inactive and stationary), but stochastically switch which subunit actively translocates. This model captures the dynamics of a proposed mechanism dubbed "asymmetric strand switching" (see Figure 2 d in (Hassler et al., 2018)). In our model, switches occur at rate k_{switch}; by switching, inactive subunits become active and vice versa. Thus, LEF subunits have trajectories similar to the one shown in **Figure 1 e,** top panel, and loops grow as shown in the arch diagram at the bottom of **Figure 1 e**. Although not yet observed experimentally, we hypothesize that switching activity of SMC complexes could potentially be induced by exchange of subunits within the SMC complex, different solution conditions, or post-translational or genetic modifications, all of which can alter SMC complex behavior in experiments (Eeftens et al., 2017; Elbatsh et al., 2019; Ganji et al., 2018; Keenholtz et al., 2017; Kleine Borgmann et al., 2013; Kschonsak et al., 2017).

We explore the switching model by varying the switching rate scaled by either the dissociation rate k_{unbind} (for the eukaryotic chromosome models) or the chromosome traversal rate v/L (for the bacterial chromosome model). For eukaryotes, the dimensionless ratio k_{switch}/k_{unbind} determines the mean number of switches before a LEF unbinds from the chromatin fiber (Banigan and Mirny, 2019). For $k_{switch}/k_{unbind}<1$, switches rarely occur and LEF trajectories typically appear to be pure one-sided. In contrast, for $k_{switch}/k_{unbind}>1$, the active and inactive LEF subunits may frequently switch before unbinding chromatin, and trajectories appear as in **Figure 1 e,** top panel. For bacteria, the dimensionless quantity $k_{switch}L/v$ is a dimensionless measure of the switching rate, chosen because chromosome-traversing bacterial SMC complexes (like *B.*

subtilis SMC complexes) do not have a well defined unbinding rate. When this ratio is large, switching occurs many times during chromosome traversal; when it is small, switching is rare.

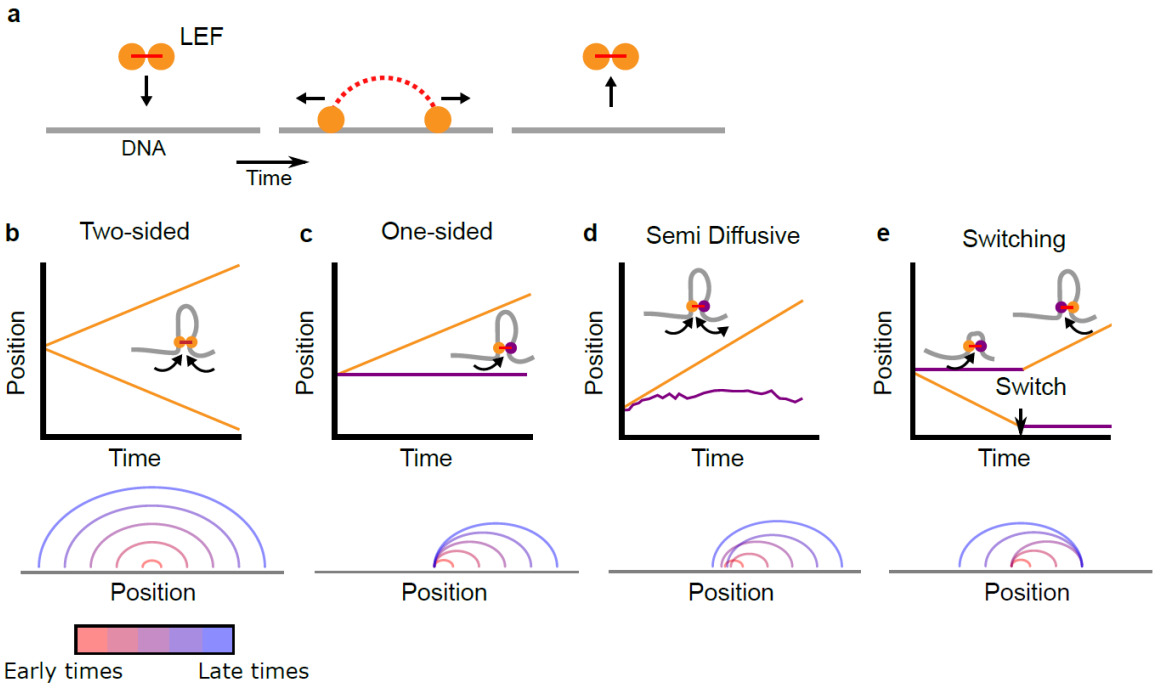

Figure 1. Two-sided loop extrusion and variants of one-sided loop extrusion. (a) A schematic of the loop extrusion model. The two subunits of the LEF bind to sites on a one-dimensional lattice representing DNA/chromatin. Over time, the subunits may translocate along DNA, and the LEF eventually unbinds from DNA. In 3D polymer simulations, the two subunits remain in spatial proximity (in 3D) while translocating along DNA (in 1D), thereby extruding loops. **(b)** *Top:* The positions of the two LEF subunits versus time for a two-sided LEF. *Inset:* Cartoon of a two-sided LEF on DNA extruding a loop. *Bottom*: Arch diagram showing the positions of the LEF subunits from early times (red) to late times (blue). **(c)** *Top:* Time trace of a one-sided LEF with inset schematic. In the example in the schematic, the active subunit is on the left, but in the model LEFs are loaded with random orientations. *Bottom:* Arch diagram for a one-sided LEF, where the left subunit is stationary (passive). **(d)** *Top:* The positions of the two LEF subunits versus time for the semi-diffusive model. The speed of loop growth increases as the loop grows because the entropic cost of loop growth most strongly affects small loops. *Bottom:* Arch diagram for the semi-diffusive model, where the left subunit is diffusive. **(e)** *Top:* Schematic and a time-trace of the switching model. *Bottom:* Example of an arch diagram for a LEF in the switching model (note that the arch diagram does not correspond to the time trace).

Models for 3D chromosome conformations

We investigated the degree to which the above models reproduce physiological chromosome structures via 3D polymer simulations. To do this, we coupled each of the 1D loop-extrusion models in **Figure 1** to a 3D model of a polymer chain (Fudenberg et al., 2016; Goloborodko et

al., 2016a) and performed molecular dynamics simulations using OpenMM (see Methods for details) (Eastman et al., 2017, 2013; Eastman and Pande, 2010). In this coupled model, LEFs act as a bond between the two sites (monomers) to which the LEF subunits are bound; these bonds have the dynamics described for LEFs above. We simulated each of the three models, as well as several other variants, for various values of λ, d, v_{diff}/v, and either k_{switch}/k_{unbind} or $k_{switch}L/v$. From these simulations, we obtain 3D polymer structures, images of compacted chromosomes and/or contact frequency (Hi-C-like) maps. By analyzing these data, we compare the models to experiments.

In addition to 3D polymer simulations, we generated contact maps semi-analytically from the 1D models of the underlying SMC dynamics (the two methods are compared in **Supplemental File 1**). This allowed us to explore a broad range of parameter values and assess the resulting Hi-C-like maps.

We analyze these models for three chromosome phenomena that depend on SMC complexes. Each of the following results sections briefly describes the scenario, explains the relevant model observables, and subsequently, explores each model variant.

Results

Compaction and resolution of mitotic chromosomes

Model and observables

We determined whether variants of the one-sided loop extrusion model can explain mitotic chromosome compaction and the spatial resolution of connected sister chromatids. Experimentally, it has been shown that these phenomena are driven by the condensin complex (Eykelenboom et al., 2019; Hagstrom et al., 2002; Hirano, 2016; Hirano et al., 1997; Hirano and Mitchison, 1994; Hudson et al., 2003; Nagasaka et al., 2016; Ono et al., 2003; Piskadlo et al., 2017; Shintomi et al., 2017, 2015; Steffensen et al., 2001). During mitosis, mammalian chromosomes are linearly compacted ~1000-fold, leading to the formation of rod-like chromatids. Such compaction is thought to facilitate the spatial resolution of sister chromatids, which are connected at their centromeres.

Previous work suggests that the two-sided loop extrusion model can rapidly achieve 1000-fold linear compaction in the regime in which LEFs are densely loaded on the chromosome ($\lambda/d \approx 10$), which is expected for mitotic chromosomes of higher eukaryotes (Goloborodko et al., 2016b). With a loop extrusion speed of $v \approx 1$ kb/s (Ganji et al., 2018), two-sided extrusion can achieve full linear compaction within one residence time ($1/k_{unbind}$~2-10 min (Gerlich et al., 2006a; Terakawa et al., 2017; Walther et al., 2018)) and full 3D compaction and loop maturation occurs over a few (<10) residence times (Goloborodko et al., 2016a), consistent with the duration of prophase and

prometaphase and *in vivo* observations of mitotic chromosome compaction (Eykelenboom et al., 2019; Gibcus et al., 2018) and resolution (Eykelenboom et al., 2019).

In contrast, theoretical work has demonstrated that pure one-sided loop extrusion cannot linearly compact a chromatin fiber by more than ~10-fold (Banigan and Mirny, 2019). Linear compaction in these models depends only on the dimensionless ratio of length scales λ/d (Banigan and Mirny, 2019; Goloborodko et al., 2016b). However, the 3D structures of such chromosomes have not yet been studied, and compaction by the semi-diffusive model, switching model, and other model variants has not been comprehensively investigated. Furthermore, sister chromatid resolution by variations of the one-sided loop extrusion model has not been investigated.

We therefore performed simulations to measure linear compaction and characteristics of 3D chromosome organization of individual, compacted chromosomes. To measure linear compaction, we define the compacted fraction, f, as the fraction of chromosome length that is contained within looped regions and the resulting linear fold compaction as $FC=1/(1-f)$. We measure the resulting 3D compaction by computing chromosome volume, V, which is expected to decrease by >2-fold during mitotic compaction (Daban, 2003; Hihara et al., 2012; Liang et al., 2015; Nagasaka et al., 2016; Sumner, 1991). We thus look for scenarios in which chromosomes are linearly compacted ~1000-fold and form the spatially compact rod-like arrays of chromatin loops observed in experiments (Earnshaw and Laemmli, 1983; Gibcus et al., 2018; Guacci et al., 1994; Lawrence et al., 1988; Maeshima et al., 2005; Marsden and Laemmli, 1979; Ono et al., 2003; Paulson and Laemmli, 1977; Walther et al., 2018).

We also characterize the ability of one-sided loop extrusion models to resolve sister chromatids connected at their centromeres. We quantify chromatid resolution by measuring the median inter-chromatid backbone distance, ΔR, scaled by the polymer backbone length, R_b. As a supplementary metric, we also compute the inter-chromatid overlap volume, V_o, compared to the overlap volume without loop extrusion, $V_o^{(0)}=3.6\ \mu m^3$. Larger distances, $\Delta R/R_b>1$, indicates that typical inter-chromatid distances are sufficient to prevent contacts between backbones. Median distance and overlap are expected to contribute to the disentanglement of chromatids (Piskadlo et al., 2017; Sen et al., 2016), which facilitates chromosome segregation by preventing anaphase bridge formation (Charbin et al., 2014; Green et al., 2012; Hagstrom et al., 2002; Nagasaka et al., 2016; Piskadlo et al., 2017; Steffensen et al., 2001). Models are thus evaluated on the basis of whether compacted chromatids are fully spatially resolved.

Pure one-sided extrusion can neither compact nor resolve chromatids

Mean-field theory predicts that pure one-sided loop extrusion can achieve at most ≈10-fold linear compaction, 100-fold less than expected for mammalian mitotic chromosomes. **Figure 2 c (i)** shows linear fold compaction, FC, as a function of λ/d in the simulations, and results for $\lambda/d \gg 1$ are consistent with the theoretical predictions (Banigan and Mirny, 2019). The compaction limit is due to the unavoidable presence of “gaps” of uncompacted (unlooped) chromatin

between some adjacent loops (**Figure 2 c (ii)**); of the four possible orientations of adjacent translocating LEFs, →→, ←←, →←, and ←→, the last one necessarily leaves an unlooped gap (Banigan and Mirny, 2019); the mechanistic connection between gaps and deficient compaction is illustrated by simulations broadly spanning λ/d (**Figure 2 c (ii)**).

We find that the presence of unlooped gaps along the chromatin fiber additionally has severe consequences for the 3D conformations of simulated mitotic chromosomes. As shown in **Figure 2 b** (left), chromosomes compacted by one-sided LEFs are more spherical, and compacted regions are interspersed with uncompacted (unlooped) chromatin fibers. Moreover, compaction by one-sided LEFs only reduces the volume, V, by up to 2-fold from the uncompacted volume of $V^{(0)}$=3.6 μm^3 (**Figure 2 c (iii)**). This contrasts with the structures observed and >2.5-fold 3D compaction in the two-sided loop extrusion model (**Figure 2 a**, left). Moreover, adding a small number of two-sided LEFs does not close a sufficient number of gaps to achieve 1000-fold linear compaction (**Figure 2 - figure supplement 2 a)** (Banigan and Mirny, 2019) or 2.5-fold volumetric compaction (**Figure 2 - figure supplement 2 c**) because even a small number of gaps prevents full compaction **(Figure 2 - figure supplement 2 b**). A fraction of >80% of two-sided LEFs is necessary for sufficient compaction and resolution. One-sided extrusion thus leads to loosely compacted chromosomes that are qualitatively different from mitotic chromosomes observed in both the two-sided loop extrusion model and *in vivo*.

We therefore investigated whether the inability of one-sided LEFs to compact chromosomes also impacted their ability to resolve sister chromatids. We find that one-sided LEFs can spatially resolve chromosomes that are physically linked at their centromeres, but far less effectively than two-sided LEFs. With one-sided extrusion, there is a small relative separation between chromatid backbones ($\Delta R/R_b$<1, **Figure 2 c (iv)**) and large overlap of chromatids ($V_o/V_o^{(0)}$≈0.3; **Figure 2 - figure supplement 1 c**)**.** In contrast, with two-sided extrusion, there is a larger distance between chromatid backbones ($\Delta R/R_b$>10), and consequently, less overlap of chromatids ($V_o/V_o^{(0)}$ ≈ 0.1). The resulting linked chromatids are reminiscent of microscopy images of mitotic chromosomes (**Figure 2 a,** right panel, and *e.g.*, (Maeshima et al., 2005)), as has been observed in previous simulations (Goloborodko et al., 2016a). Thus, we find that chromatin gaps left by pure one-sided extrusion inhibit the spatial resolution of linked chromosomes; moreover, determining the presence or lack of unlooped chromatin gaps in 1D is sufficient to predict the effects on 3D compaction. Together, these results indicate that while the two-sided loop extrusion model can explain condensin-mediated vertebrate mitotic chromosome resolution, the pure one-sided loop extrusion model cannot.

Semi-diffusive one-sided extrusion does not efficiently compact chromosomes

We next investigated the semi-diffusive one-sided extrusion model, in which the inactive LEF subunit may passively diffuse. We find that semi-diffusive LEFs can compact chromatin to a greater extent than pure one-sided LEFs in some scenarios, but are unable to achieve 1000-fold linear compaction for a plausible values of λ/d (*i.e.*, λ/d<1000, which is expected from experimental measurements (Fukui and Uchiyama, 2007; Ganji et al., 2018; Gerlich et al.,

2006a; Kong et al., 2019; Takemoto et al., 2004; Terakawa et al., 2017; Walther et al., 2018) (**Figure 2 d (i)**). The enhanced compaction by semi-diffusive one-sided LEFs arises from their ability to close some unlooped gaps (**Figure 2 d (ii)**). LEFs may suppress gaps in two ways: 1) inactive but diffusive LEF subunits may stochastically slide toward each other and 2) diffusion of an inactive subunit of a "parent" LEF may be rectified if a "child" LEF is loaded within the loop so that the active subunit of the child LEF moves toward the inactive subunit of the parent LEF, leading to Brownian ratcheting (**Figure 2 - figure supplement 3 a)**. The first mechanism is ineffective in eliminating gaps because it is opposed by the conformational entropy of the extruded loop (Brackley et al., 2017), and the LEFs may also diffuse apart, causing the unlooped gap to reappear. The second mechanism can be enhanced by the active subunit of the child LEF actively "pushing" the parent's inactive subunit (**Figure 2 - figure supplement 4** and **Supplemental File 1**). These active processes are more effective at closing gaps. Nonetheless, Brownian ratcheting by nested LEFs does not sufficiently linearly compact chromosomes for all $\lambda/d<1000$, while active pushing can only achieve a high degree of compaction if the active subunit can simultaneously reel chromatin through multiple inactive subunits and $\lambda/d\approx1000$.

To understand how semi-diffusive LEFs enhance linear compaction in some particular scenarios, we investigated how compaction depends on the scaled diffusion speed, v_{diff}/v. For $v_{diff}/v\ll1$, the inactive subunit diffuses very slowly, so the LEFs behave similarly to pure one-sided LEFs; moreover, thermal ratcheting by nested LEFs is very slow since the translocation speed of the active subunit of the child LEF is effectively limited by the diffusion of the inactive subunit of the parent LEF. Interestingly, in the case with rapid diffusion, $v_{diff}/v>1$, semi-diffusive LEFs linearly compact chromosomes even less effectively than pure one-sided LEFs. Because conformational entropy favors shrinkage of parent loops, the diffusive subunit shrinks loops more rapidly than the active subunit grows loops. Since loops remain small, nesting of loops (*i.e.*, LEFs extruding loops within loops) becomes less likely (**Figure 2 - figure supplement 3).** Thus, gaps remain because they are not closed by Brownian ratcheting. Intriguingly, our simulations reveal that $v_{diff}/v\approx1$ is an optimal case in which diffusion is sufficiently slow to permit loops to grow large enough to allow loop nesting, but fast enough to promote loop growth by thermal ratcheting. However, even this "optimal" case leaves a large number of gaps. Thus, we find that for all v_{diff}/v unlooped gaps remain (**Figure 2 d (ii)**) and 1000-fold compaction cannot be achieved with $\lambda/d<1000$ (**Figure 2 d (i)).**

In the semi-diffusive model, as in the pure one-sided model, the limited ability to linearly compact chromosomes impairs 3D compaction. Simulated chromosomes are generally not rod-like (**Figure 2 d (iii)**, inset), and the loop architecture remains gapped and weakly reinforced. Consequently, for optimal scaled diffusion speeds, $v_{diff}/v\approx1$, the volume, V, is reduced by less than in the case of two-sided extrusion (≤2-fold vs. >2.5-fold, **Figure 2 d (iii)**). Similarly, modest linear compaction of chromatids leads to only a slight increase in inter-chromatid distance (**Figure 2 d (iv)**) and moderate overlap volume ($V_o/V_o^{(0)}\approx0.2$). Thus, 3D compaction and sister chromatid resolution in the semi-diffusive model can exceed that of the pure-one sided model, but still fall short of the far more dramatic compaction and distinct resolution

expected for mitotic chromosomes *in vivo* and reproduced by the two-sided loop extrusion model. The failure of this one-sided loop extrusion variant is again due to the inability to robustly eliminate unlooped gaps.

One-sided loop extrusion with switching recapitulates mitotic compaction

The results of the previous sections suggest that robust mitotic chromosome compaction and chromatid resolution requires LEFs that consistently and irreversibly eliminate unlooped gaps. We therefore consider a variation of the one-sided extrusion model in which only one LEF subunit translocates at a time, but the LEFs stochastically switch which subunit is active at rate k_{switch}. In principle, in this scenario, LEFs may be "effectively two-sided," which allows LEFs initially in a divergent orientation (←→) to eliminate the initially unlooped gap (Banigan and Mirny, 2019).

To study mitotic chromosome compaction within the switching model, we vary both λ/d and the scaled switching rate, k_{switch}/k_{unbind}. The scaled switching rate determines the number of times that a LEF will switch before unbinding; each switch allows a LEF to attempt to close a gap (Banigan and Mirny, 2019). Accordingly, we observe that the ability of LEFs to linearly compact chromatin increases with k_{switch}/k_{unbind}. For very slow switching rates ($k_{switch}/k_{unbind} \ll 1$, or roughly $k_{switch} \ll 1$ min^{-1} for experimentally observed k_{unbind} (Ganji et al., 2018; Gerlich et al., 2006a; Terakawa et al., 2017; Walther et al., 2018)), loop extrusion is effectively one-sided because switches rarely occur and gaps are not closed, so linear compaction is limited to ~10-fold (**Figure 2 e (i), (ii),** cyan). For faster scaled switching rates ($0.1<k_{switch}/k_{unbind}<1$), switches are more likely to occur during each LEF's residence time, so greater numbers of LEFs are effectively two-sided and more gaps are can be closed (**Figure 2 e (i), (ii),** purple). In these cases, LEFs linearly compact chromosomes 10- to 100-fold. For very fast switching ($k_{switch}/k_{unbind}>1$ or $k_{switch}>1$ min^{-1}), many switches occur per residence time. Thus, all LEFs are effectively two-sided so that all unlooped gaps are eliminated for large λ/d, and 1000-fold linear compaction can be achieved (**Figure 2 e (i), (ii)**, magenta).

Concordantly with observations for linear compaction, we find that 3D chromosome compaction and resolution varies from the one-sided to two-sided phenotypes with increasing scaled switching rate, k_{switch}/k_{unbind}. Chromosomes with rapidly switching LEFs can undergo a large reduction in volume, V (>2.5-fold, **Figure 2 e (iii)**), comparable to what is observed for two-sided extrusion. Similarly, sister chromatid resolution can be achieved in the switching model for $k_{switch}/k_{unbind}>1$. The distance between chromatid backbones increases ($\Delta R/R_b>8$, **Figure 2 e (iv)**), and overlap is greatly reduced ($V_o/V_o^{(0)}\approx 0.1$), comparable to what is achieved in the two-sided model. We thus conclude that the switching model with fast switching rates, k_{switch}~1 min^{-1}, can reproduce the experimentally observed 3D compaction and resolution of mammalian mitotic chromosomes.

Of the three main variants of one-sided loop extrusion that we tested, only the switching model can reproduce mammalian mitotic chromosome compaction and resolution. In each of these

models, the ability of LEFs to eliminate unlooped gaps governs compaction and resolution. Chromatin segments that are not linearly compacted into loops are longer, and thus have a larger 3D size. Therefore, the average number of unlooped gaps that remain, a 1D quantity, determines the 3D structure and organization of simulated mitotic chromosomes. Effectively two-sided LEFs are required to eliminate these gaps, and of the models considered here, this physical mechanism is reliably present in only the switching model.

Attractive interactions between LEFs cannot rescue one-sided extrusion

As an alternative to the models above, which are dominated by the effects of extrusion-driven linear compaction, we performed polymer simulations to determine whether gaps created by one-sided loop extrusion could be eliminated by 3D attractive interactions between LEFs or between different polymer segments (*e.g.*, poor solvent). Moreover, we explored whether such interactions could volumetrically compact chromosomes and generate rod-like mitotic chromosomes, as previously suggested (Sakai et al., 2018). We find that 3D attractions can volumetrically compact polymers (**Figure 2 - figure supplement 5 a**), but the resulting structures do not resemble mitotic chromosomes. When LEFs attract each other, compacted chromosomes form extended, clumpy structures (**Figure 2 - figure supplement 5 b**, top), and chromatin gaps remain visible. Moreover, sister chromatids do not spatially segregate (**Figure 2 - figure supplement 5 b**, bottom). When the simulated chromosomes are instead treated as polymers in poor solvent, chromosomes are compacted into spherical structures and sister chromatids cannot be spatially resolved (**Figure 2 - figure supplement 5 c**). Attractive interactions have little effect on chromosome structure when the interaction strength, ε, is low, but when ε is large, the chromosome is compacted into a spherical globule. These findings are consistent with previous theoretical and computational work on polymer combs (Fytas and Theodorakis, 2013; Sheiko et al., 2004), showing that 3D attractive interactions lead to a coil-globule transition. Altogether, we find that 3D attractive interactions cannot be the mechanism of gap closure for mitotic chromosomes.

LEF traversal might rescue one-sided extrusion

Recent single-molecule experiments report the first observations of effectively two-sided loop extrusion that results from the coordinated activity of two one-sided loop extruders (Kim et al., 2019). Single-molecule experiments have shown that yeast condensins can form “Z-loops” that act as an effectively two-sided extruder. In this scenario, condensins can pass each other as they translocate along DNA, thus forming structures that reel in DNA from two directions. To analyze this possibility, we simulated chromosomes compacted by LEFs that can freely traverse each other. In this model, linear chromosome compaction, as quantified by loop coverage, increases exponentially with λ/d, as expected from theory (**Figure 2 f** and **Supplemental File 1**). Correspondingly, we observe that chromosomes in this model form compact, rod-like structures (**Figure 2 g**). We find that ~1000-fold linear compaction is achieved for λ/d~7, which can be satisfied with reasonable physiological values of loop sizes, $\ell=\lambda$~140 kb (Earnshaw and Laemmli, 1983; Gibcus et al., 2018; Naumova et al., 2013; Paulson and Laemmli, 1977) and densities of one LEF per d~20 kb (Fukui and Uchiyama, 2007; Takemoto et al., 2004; Walther et

al., 2018). In addition, LEFs in this model can spatially resolve sister chromatids (**Figure 2 h**). Thus, one-sided LEFs that can freely traverse each other may be sufficient to compact and resolve mitotic chromosomes.

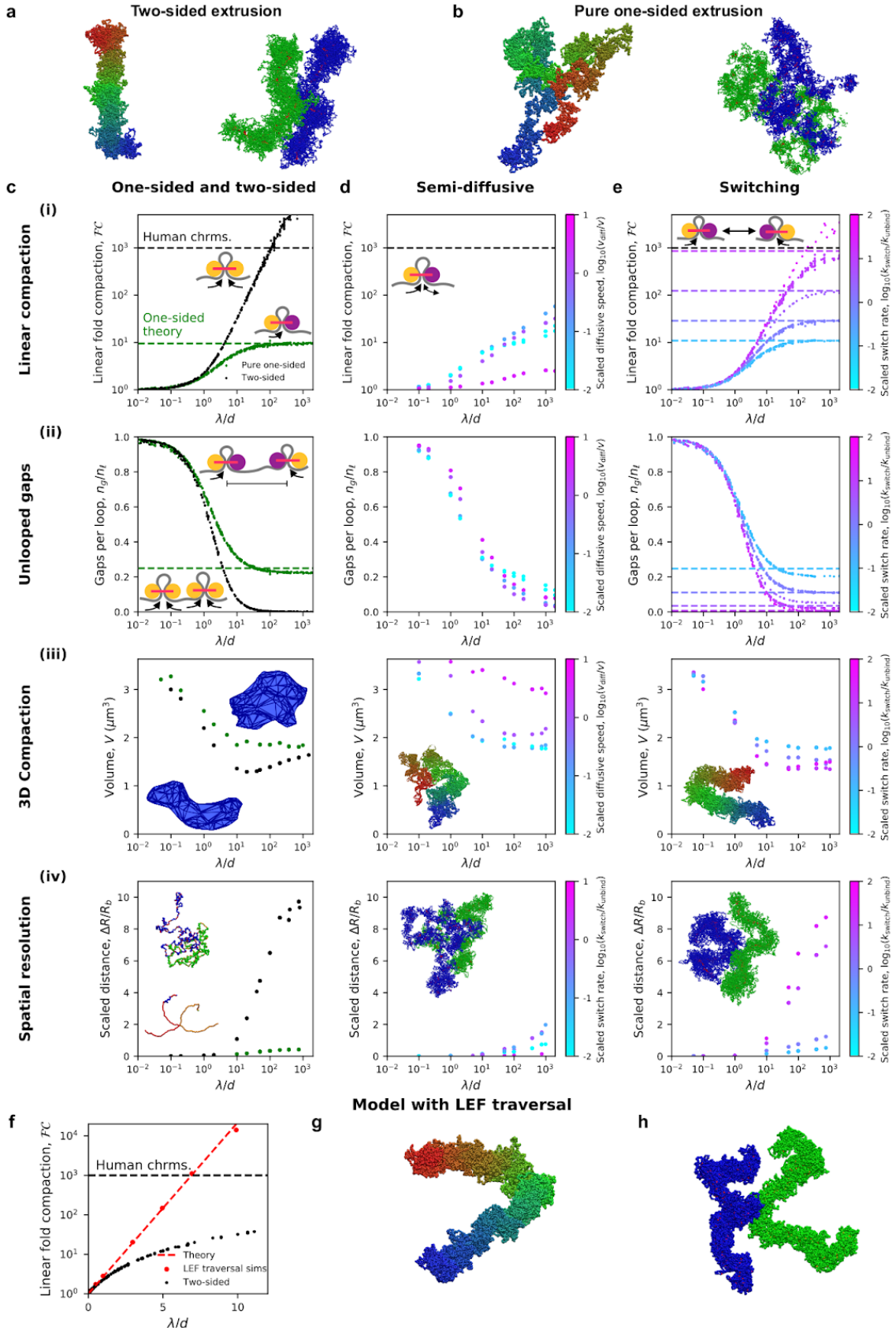

Figure 2. Chromosome compaction and structure in the one-sided loop extrusion model and model variants. (a) Simulation snapshots of chromosomes compacted (left) and spatially resolved (right) by two-sided extrusion. **(b)** Simulation snapshots showing deficient compaction (left) and resolution (right) of chromosomes with pure one-sided loop extrusion. **(c)** One-sided loop extrusion model, as compared to the two-sided model. ***(i)*** Linear fold compaction, *FC*, as a function of the dimensionless ratio, λ/d, of the processivity to the mean distance between LEFs. Pure one-sided extrusion (green) saturates at ≈10-fold compaction for large λ/d, as predicted by mean-field theory (green dashed line). *FC* by two-sided extrusion (black) surpasses the 1000-fold linear compaction expected for human chromosomes (black dashed line) for $\lambda/d>50$. Inset cartoons illustrate extrusion of chromatin (gray) by active LEF subunits (yellow). Stationary passive subunit for one-sided LEF is purple. ***(ii)*** Number of gaps per parent loop, n_g/n_ℓ, saturates at ≈0.25 (dashed line) as λ/d increases in the pure one-sided model (green), as expected from theory. For two-sided extrusion, n_g/n_ℓ approaches 0 (black). Insets illustrate the mechanisms of gap formation and closure. ***(iii)*** Chromosome volume, *V*, decreases as λ/d increases. *V* can achieve smaller values, in the two-sided model (black) than in the one-sided model (green). Insets: Images of concave hulls of simulated chromosomes compacted by one- and two-sided extrusion (top and bottom, respectively). ***(iv)*** Scaled distance, $\Delta R/R_b$, between sister chromatid backbones in one- or two-sided models. Insets show chromatid backbones in simulations of one- and two-sided extrusion (top and bottom, respectively). **(d)** Semi-diffusive model. ***(i)*** $FC<1000$ for $\lambda/d<1000$. Color from cyan to magenta indicates increasing scaled diffusive stepping speed, v_{diff}/v. Inset shows a semi-diffusive LEF. ***(ii)*** Number of gaps per loop, n_g/n_ℓ versus λ/d. ***(iii)*** Compacted chromosome volume, *V*, versus λ/d. Inset shows chromosome compacted by semi-diffusive LEFs with $v_{diff}/v=1$. ***(iv)*** Scaled distance, $\Delta R/R_b$, between chromatid backbones. Inset shows image of spatial resolution with $v_{diff}/v=1$. **(e)** Switching model. ***(i)*** *FC* can surpass 1000-fold linear compaction for rapid scaled switching rates, $k_{switch}/k_{unbind}>10$ (magenta). Simulations with large λ/d match mean-field theoretical predictions (colored dashed lines). Inset illustrates the model. ***(ii)*** Number of gaps per loop, n_g/n_ℓ, with mean-field theoretical predictions (dashed lines). ***(iii)*** Compacted chromosome volume, *V*. Inset image shows compacted chromosome with $k_{switch}/k_{unbind}=30$. ***(iv)*** Scaled distance, $\Delta R/R_b$, between chromatid backbones. Inset shows spatial resolution in simulations. **(f)** Linear fold-compaction for a chromosome with LEFs that are able to traverse each other. Dashed line shows theoretical fold compaction, as quantified by loop coverage, $FC=e^{\lambda/d}$. **(g)** Simulation snapshot of chromosome compacted by LEFs that may traverse each other. **(h)** Simulation snapshot of chromatids resolved by LEFs that may traverse each other.

Figure supplement 1. Measures of compaction and segregation with different densities of LEFs.

Figure supplement 2. Compaction in model with a mix of one- and two-sided LEFs.

Figure supplement 3. Loop sizes and LEF nesting explain the ineffectiveness of the semi-diffusive model.

Figure supplement 4. Models in which the active subunits of nested LEFs can push passive LEF subunits.

Figure supplement 5. Defective compaction and segregation with 3D attractive interactions.

Formation of interphase chromosome TADs, stripes, and dots

Model and observables

Next, we determined whether one-sided extrusion can recapitulate prototypical features in Hi-C and micro-C maps (Krietenstein et al., 2019) of higher eukaryotes during interphase, such as TADs, “stripes” (or “lines”), and particularly, the “dots” (or “corner peaks”) found at the boundaries of TADs (**Figure 3 a**). Dots are foci on Hi-C maps that reflect enriched contact frequency between specific loci, often found at the corners of TADs and/or between proximal (<1-2 Mb) CTCF sites (Krietenstein et al., 2019; Rao et al., 2014). TADs, stripes, and dots are cohesin-mediated, and they can be modulated by changes to cohesin and/or CTCF. Thus, we evaluate extrusion models based on whether they can generate these hallmarks of interphase chromosome organization.

We perform polymer simulations for each model, sweeping λ and d (Cattoglio et al., 2019; Fudenberg et al., 2016; Holzmann et al., 2019), as well as model-specific parameters. CTCF barriers are modeled as partially permeable loop-extrusion barriers (Fudenberg et al., 2016; Nuebler et al., 2018). We use the contact probability curve, $P_c(s)$, to optimize the simulation parameters for wild-type (WT) conditions (Methods and **Figure 3 - figure supplement 1**). We compute and visualize contact maps from these simulations and quantify the dot strength by the enhancement of dot contact frequency over background, as in **Figure 3 - figure supplement 2** (Gassler et al., 2017).

Pure one-sided extrusion can reproduce some but not all features of interphase organization

In models of two-sided loop extrusion in interphase, a TAD arises due to the formation of extruded loops within a particular region, usually bounded by convergently oriented CTCF sites. A stripe emerges if one extruding subunit of a LEF is stalled by CTCF while the other subunit continues extruding (**Figure 3 - figure supplement 3**). A dot arises when two barriers to extrusion (*e.g.*, convergently oriented CTCF sites) are brought together by one or a few LEFs that close a gap between two barriers (**Figure 3 - figure supplement 3**) (Fudenberg et al., 2016; Sanborn et al., 2015).

While two-sided extrusion can reproduce TADs, stripes, and dots, we found that the simplest model of one-sided extrusion can recapitulate only some of these features. When LEFs are uniformly loaded onto chromatin, pure one-sided extrusion can form the bodies of TADs and stripes, but does not form dots (**Figure 3 b**, right panel). For one-sided extrusion, stripes are an average effect of LEFs loading at different loci and extruding up to a barrier (**Figure 3 - figure supplement 3**), while dots are not formed because only one-sided LEFs loaded at a barrier can pair two barriers (**Figure 3 - figure supplement 3**). This problem cannot be resolved by increasing the processivity, λ, or decreasing the separation between LEFs, d (**Figure 3 - figure supplement 4**). In contrast, two-sided extrusion with increased processivity generates the

strong dots seen in wild-type data as well as the "extended dots" (**Figure 3 b** and **Figure 3 - figure supplement 5**) seen in Wapl knockout (KO) data (Gassler et al., 2017; Haarhuis et al., 2017; Wutz et al., 2017). This failure to form dots is due to inevitable gaps that one-sided extrusion leaves between LEFs and between LEFs and CTCF barriers (**Figure 3 c**).

Semi-diffusive one-sided extrusion cannot produce Hi-C dots

The semi-diffusive model creates a phenotype that is similar to that of pure one-sided extrusion for simulations of WT conditions (**Figure 3 d**); it can generate TAD bodies and stripes, but not dots. We conclude that the semi-diffusive one-sided model works similarly to pure one-sided model, and it is also limited by its inability to close gaps between LEFs and between LEFs and barriers.

One-sided extrusion with preferential loading at TAD boundaries

Next, we considered variations of the model in which one-sided LEFs are loaded nonuniformly, with increased probability of loading at barriers (Nichols and Corces, 2015; Rubio et al., 2008) (**Figure 3 d**). Each barrier has two loading sites and one-sided LEFs are loaded directionally so that they translocate away from the boundary. Loading of LEFs at CTCF sites increases both the primary and extended dot strengths, qualitatively reproducing both wild-type conditions (λ=200 kb, d=200 kb) (**Figure 3 d**) and Wapl KO (λ=2 Mb, d=200 kb) conditions (**Figure 3 - figure supplement 6**). To clearly observe dots, however, LEFs must have a strong loading bias, *i.e.*, >100-fold preference to bind barrier sites as compared to body sites. While contacts within the TAD body are reduced for this large bias (**Figure 3 d**), it is possible to find a loading bias and LEF density such that both dots and the TAD body are clearly visible (**Figure 3 - figure supplement 6**). Although current experimental evidence does not support preferential loading of cohesin at CTCF sites in mammals (Busslinger et al., 2017; Fudenberg et al., 2017; Nora et al., 2017; Parelho et al., 2008; Wendt et al., 2008), such a mechanism of TAD, stripe, and dot formation is feasible and may be operational in other species.

One-sided extrusion with switching reproduces all features of interphase organization

We hypothesized that mechanisms other than loading at CTCF could enable one-sided extrusion to reproduce interphase Hi-C features. We considered the switching model because a LEF, when switching frequently enough, might bring two barriers together, even if it is not loaded at a barrier. Moreover, switching could eliminate gaps between nearby LEFs.

The switching model for slow switching rates approximates the pure one-sided model; primary and extended dots are not present (**Figure 3 d**, third column) and they do not appear with increased λ (**Figure 3 - figure supplement 2**). For faster switching rates, primary and extended dots appear (and loop strengths increase with λ, **Figure 3 - figure supplement 2**), as they do in the two-sided model (**Figure 3 d**, third column). The switching model approaches the two-sided extrusion model, as quantified by primary and extended dot strengths for $k_{switch}/k_{unbind}\approx10$ (**Figure 3 - figure supplement 2**). Thus, the model suggests that cohesin must undergo a switch once per minute for characteristic residence times of ~10-20 minutes (Gerlich et al., 2006b; Hansen

et al., 2017; Kueng et al., 2006; Stigler et al., 2016). In addition to dots, switching generates a high frequency of intra-TAD contacts and stripes (**Figure 3 d**, third column). Thus, one-sided LEFs that switch sufficiently fast can account for features of interphase chromosome organization.

A mix of one- and two-sided extrusion can reproduce features of interphase organization

A mix of one- and two-sided LEFs approaches either the one-sided or the two-sided phenotype depending on the percentage of two-sided LEFs (**Figure 3 d**, right column). Dots are visible, but weak for a mix with 20% two-sided LEFs, while a mix with 60% two-sided LEFs approaches the two-sided dot strength and generates stripes and intra-TAD contacts (**Figure 3 d**, right column). A lower percentage of two-sided extruders, however, is needed to reproduce interphase organization (~50%) than to achieve strong mitotic compaction (>80%). While even a small fraction of gaps can be detrimental to mitotic compaction, gaps between LEFs are less damaging for the interphase, in which LEFs are more sparse along the chromosome (**Figure 3 c**).

Taken together our simulations show that features of interphase chromosome organization can be reproduced by variants of one-sided extrusion where (a) extruders can switch their directionality approximately every minute; (b) one-sided extruders are mixed with two-sided extruders; or (c) extruders have a >100-fold preference for loading at CTCF sites.

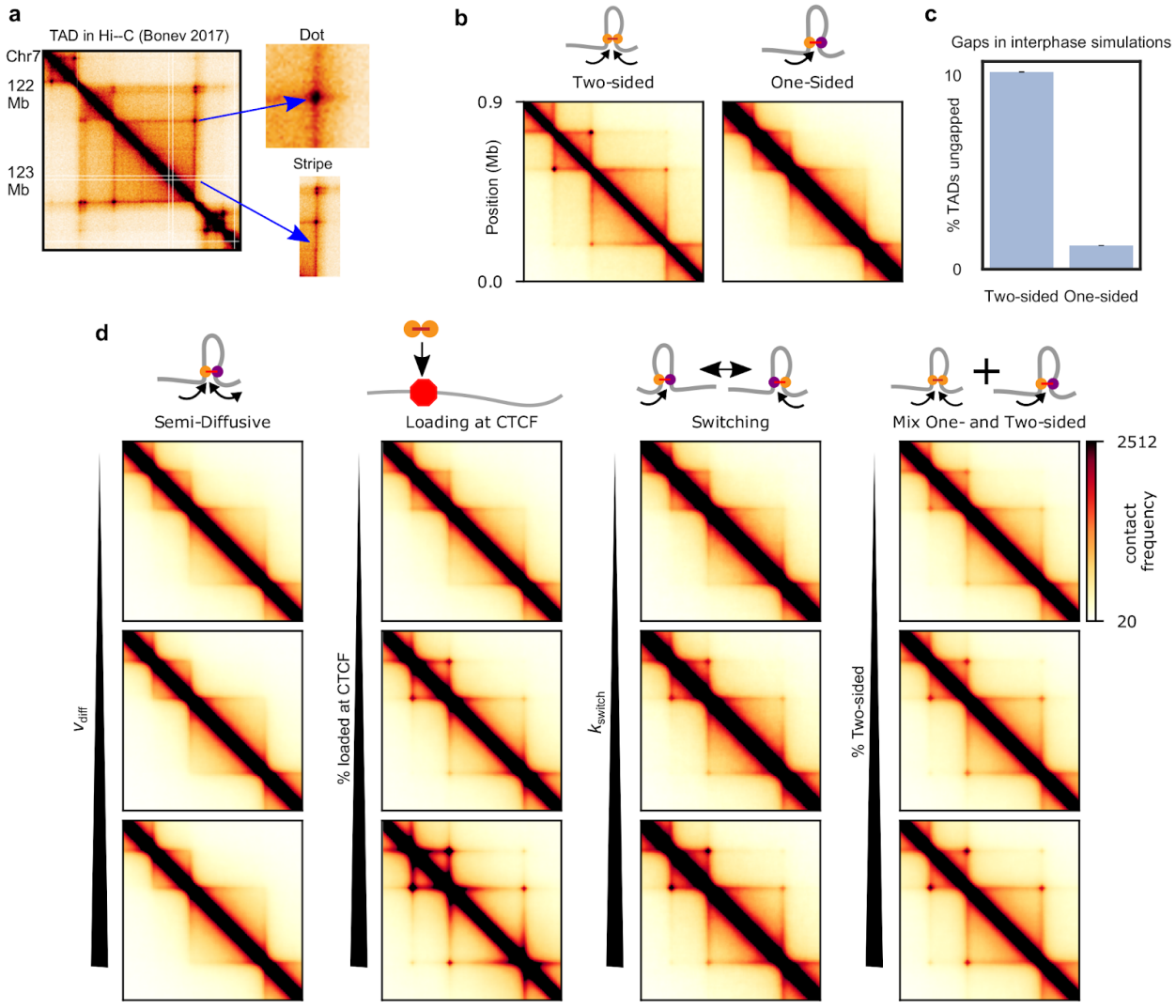

Figure 3. TADs and corner peaks for variations on one-sided loop extrusion. (a) A TAD in Hi-C of cortical neurons (Bonev et al., 2017), visualized by HiGlass (Kerpedjiev et al., 2018) at a resolution of 8 kb. Two characteristic features of TADs, stripes and dots, are indicated. **(b)** Contact maps computed from polymer simulations with two-sided (left) and one-sided (right) LEFs. The residence time and density of LEFs have been chosen to match WT conditions (d=λ=200 kb) (Methods and **Figure 3 - figure supplement 1**). **(c)** Percentage of ungapped TADs for the same LEF separation and processivity as in (b). The percentage of ungapped TADs is computed over 100,000 LEF turnover times, for a system of 20 TADs of size 400 kb, the same size as the largest TAD in the contact maps. The standard error in the mean of the percentage of ungapped TADs is less than 0.05%. **(d)** Contact maps computed from polymer configurations for the semi-diffusive model, the one-sided model with biased loading, the switching model, and the model with a mix of one- and two-sided LEFs. WT values of d and λ are used for every map. The parameter values, from top to bottom and from left to right, are: v_{diff}/v=0.1, 1, and 3.5, bias for loading at CTCF=10, 100, and 1000, k_{switch}/k_{unbind}=0.1, 1, and 10 and percentage two-sided=20, 40, and 60.

Figure supplement 1. Contact probability as a function of genomic distance for both experimental data (Haarhuis et al., 2017) and simulations, showing that simulation parameter values that best match well with wild type are λ=d=200 kb and parameters that match Wapl KO data are λ=2 Mb, d=200 kb.
Figure supplement 2. The definition of dot strength and dot strengths computed from simulations for various models and LEF processivities.
Figure supplement 3. A sketch of how dots and stripes are formed by one- and two-sided LEFs
Figure supplement 4. Sweep of the separation between LEFs, d, and the processivity of LEFs, for one-sided LEFs.
Figure supplement 5. Sweep of the separation between LEFs, d, and the processivity of LEFs, λ, for two-sided LEFs.
Figure supplement 6. Sweep of the separation between LEFs, d and the processivity of LEFs, λ, for one-sided extruders with a loading bias at CTCF.

Juxtaposition of bacterial chromosome arms

Model and observables

The bacterial SMC complex (bSMC) plays a direct role in juxtaposing the arms of the circular bacterial chromosome. In bacteria such as *B. subtilis*, the strong site-specific loading of bSMC followed by loop extrusion forms a distinctive pattern (Minnen et al., 2016; Tran et al., 2017; Wang et al., 2017) different from the case of uniform loading (assumed for eukaryotic systems). The bSMC loading sites (*i.e., parS* sites) are typically located near the origin of replication (<100 kb away). A secondary diagonal is visible emanating from the *parS* site in the bacterial Hi-C maps; it indicates long-ranged, high frequency contacts between chromosomal loci on opposite sides of the replichore (**Figure 4 a**) (Le et al., 2013; Marbouty et al., 2015; Wang et al., 2015). This secondary diagonal arises due to the high processivity of bSMCs (λ>4 Mb), which brings together DNA segments approximately equidistant from the origin-proximal *parS* loading sites. Recent modeling studies show that the shape and trajectory of the secondary diagonal can be theoretically predicted by a stochastic model of bSMC two-sided loop extrusion (Brandão et al., 2019; Miermans and Broedersz, 2018). In light of these recent models and data, we explore the extent to which variations of one-sided extrusion might recapitulate these results.

We compare the models for one-sided extrusion as follows. We perform 1D simulations of LEF dynamics, and then use our semi-analytical approach (see **Methods** and **Supplemental File 1**) to produce Hi-C-like contact maps. In contrast to the previous sections, we only consider the limit of large λ/d>1 as suggested by experiments (*i.e.,* d < 4 Mb < λ; see **Supplemental File 1**) (Tran et al., 2017; Wang et al., 2017; Wilhelm et al., 2015). We evaluate the model by visually comparing the width, intensity, and length of the experimental secondary diagonals to what is produced by our models.

Pure one-sided extrusion does not produce symmetric arm juxtaposition

It was recently shown by 3D polymer simulations that the pure one-sided loop extrusion model can not reproduce the secondary diagonals visible by Hi-C (Miermans and Broedersz, 2018). In contrast, two-sided loop extrusion qualitatively reproduced the experimentally observed secondary diagonal (Miermans and Broedersz, 2018), with an intensity that depends on the number of LEFs (**Figure 4 - figure supplement 3**, left column).

Using our semi-analytical approach, we recapitulate these previous results (**Figure 4 b**) and explore a broader range of parameter values. As seen in **Figure 4 b** (right panel), with bSMC loading only at a predetermined site (with up to 30 bSMCs per origin of replication (Graham et al., 2014; Wilhelm et al., 2015)), one-sided extrusion fails to yield the secondary diagonal that is characteristic of the chromosome contact maps of *B. subtilis* (**Figure 4 a**) and other bacteria (Böhm et al., 2019; Le et al., 2013; Marbouty et al., 2014; Umbarger et al., 2011; Wang et al., 2015). Instead, pure one-sided extrusion exhibits a "+"-shaped pattern overlaid on the main diagonal, which indicates contacts of the *parS* loading site with all other chromosomal loci. This results from the fact that in pure one-sided loop extrusion, one LEF subunit is fixed at the *parS* loading site, while the other subunit translocates away from it. Thus, we conclude that pure one-sided loop extrusion fails to reproduce the symmetric chromosome arm juxtaposition that is characteristic of many bacterial Hi-C maps.

Semi-diffusive one-sided extrusion does not properly juxtapose chromosome arms

We next considered the semi-diffusive case in which one subunit of the LEF actively translocates, while the other diffuses. Despite the increased mobility of the inactive subunit, the qualitative patterns of the contact map remained largely unchanged from the pure one-sided model (**Figure 4 c**). Increasing the scaled subunit diffusion rate, v_{diff}/v, broadened the "+"-shaped pattern and did not produce the secondary diagonal (**Figure 4 c** and **Figure 4 - figure supplement 4**). Interestingly, for high enough values of v_{diff}/v (**Figure 4 c**, right panel**)**, the "+"-shaped pattern is replaced by a square TAD-like structure, reminiscent of two large macrodomains separating each sister replichores from each other. No secondary diagonal was observed even when the number of LEFs that is present on the chromosome is changed (**Figure 4 - figure supplement 1**). Thus, the semi-diffusive loop-extrusion model does not explain the available Hi-C data for *B. subtilis* and *C. crescentus* (and other bacteria with a secondary diagonal).

One-sided extrusion with directional switching can juxtapose chromosome arms

We next tested whether one-sided LEFs that stochastically switch which subunit is active can recapitulate the available data. We performed a parameter sweep over a range of numbers of bSMCs and scaled switching rates, $k_{switch}L/v$, and we generated Hi-C contact maps (**Figure 4 d** and **Figure 4 - figure supplement 2**). The width of the experimentally observed secondary diagonal constrains the possible values of $k_{switch}L/v$ in our model. In experiments, the secondary diagonal is narrow, with a width of ~100 kb across the entire map. This suggests that there is

very little variance in the extrusion speeds along each chromosome arm. With more frequent switches (larger $k_{switch}L/v$), the progression of each extruding subunit along each arm varies less relative to the mean extrusion trajectory (**Figure 4 d**). We found that fast enough switching rates ($k_{switch}L/v$>200) can produce the secondary diagonal (**Figure 4 d**), irrespective of the number of bSMCs (**Figure 4 - figure supplement 2**). For *B. subtilis and C. crescentus*, we calculate that the upper bound on the mean time between switches is approximately 2-10 seconds and 10-20 seconds, respectively, with v=50 kb/min in *B. subtilis* and v=25 kb/min in *C. crescentus* as measured experimentally (**Figure 4 d**, right panel) (Tran et al., 2017; Wang et al., 2017).

Thus, in contrast to other models that we considered, one-sided extrusion with switching can juxtapose chromosomal arms, as demonstrated by the presence of the Hi-C secondary diagonal that is prominent in many bacterial maps. In our model, this requires a relatively fast switching rate, which effectively makes a one-sided LEF behave like a two-sided LEF at the physiologically relevant time-scales of a few minutes. Other variants of one-sided mechanism cannot achieve juxtaposition of bacterial arms due to tethers that remain between distal chromosome loci and the LEF loading site, indicating that bSMC is an effectively two-sided extruder.

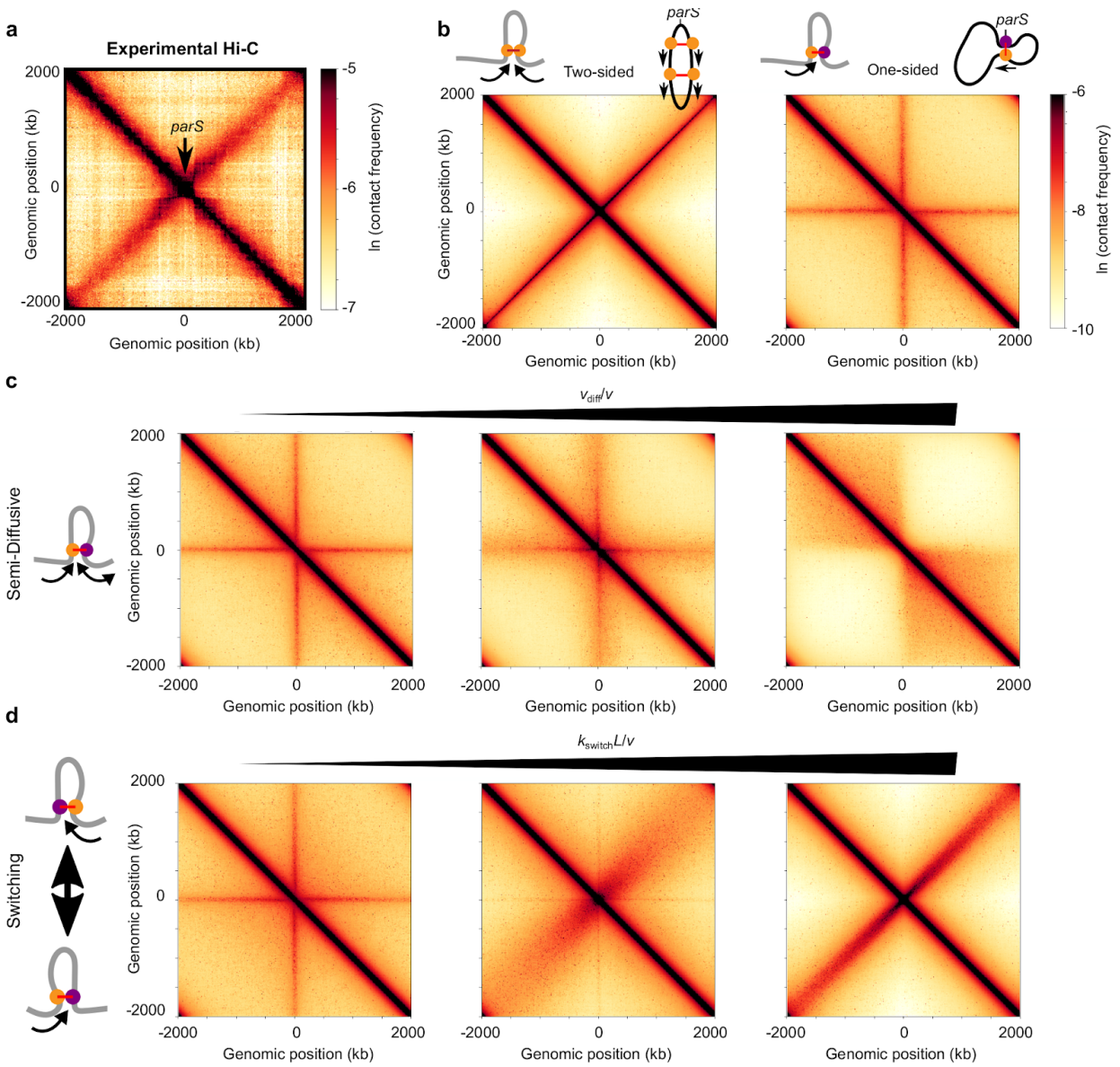

Figure 4. Effect of different extrusion rules on bacterial contact maps. (a) Experimental Hi-C map for *B. subtilis* with a single *parS* site (SMC complex loading site) near the *ori* (strain BDR2996 in (Wang et al., 2015)). Simulations of **(b)** the pure two-sided model (left map, and schematic of a single two-sided LEF and a chromosome extruded by two-sided LEFs) and the pure one-sided model (right map and schematic). **(c)** Simulations of the semi-diffusive model (with diffusive stepping rates, from left to right, of v_{diff}/v= 0.005, 0.1, and 3.5), and **(d)** the switching model (with switching rates, from left to right, of $k_{switch}L/v$=4, 40, and 400, or k_{switch}=0.001, 0.01, and 0.1 s^{-1}, respectively) of loop extrusion. All simulations displayed were performed with N=5 LEFs per chromosome.

Figure supplement 1. Sweep of the diffusive stepping rate and the number of LEFs for bacterial chromosomes.

Figure supplement 2. Contact maps from simulations for scaled switching rates and numbers of LEFs for bacterial chromosomes.

Figure supplement 3. Contact maps from simulations for different mixes of one- and two-sided LEFs and numbers of LEFs for bacterial chromosomes.

Figure supplement 4. Sweep of the active subunit stepping rates and diffusive stepping rates.

	Pure 1-sided	**2-sided**	**1-sided + 2-sided mix**	**Semi-diffusive**	**1-sided + loading bias**	**Switching**	**1-sided with traversal**	**1-sided + 3D attraction**
Mitosis	No	Yes	Yes with >80% 2-sided	No	Yes with >1000-fold bias*	Yes with k_{switch}/k_{unbind}>10	Yes	No
Interphase	No	Yes	Yes with >50% 2-sided	No	Yes with >100-fold bias	Yes with k_{switch}/k_{unbind}>10	-	-
Bacteria	No	Yes	No	No	No	Yes with $k_{switch}L/v$>200	-	-

Table 1. Summary of model results. Each entry indicates whether there are parameters for the specified model (column headings) that can explain chromosome organization in the specified scenario (row headings). Dashes indicate that the model/scenario combination was not explored. *Indicates theoretical result from (Banigan and Mirny, 2019).

Discussion

SMC complexes are ubiquitously found in all domains of life, and strong evidence is emerging that SMC protein complexes function by DNA loop extrusion, which appears to be central to their function. By forming loops, SMC complexes promote chromosome contacts spanning tens of kilobases to megabases in bacteria (Le et al., 2013; Lioy et al., 2018; Marbouty et al., 2015; Wang et al., 2015) and hundreds of kilobases in eukaryotes (*e.g.*, (Busslinger et al., 2017; Gassler et al., 2017; Gibcus et al., 2018; Rao et al., 2017, 2014; Schwarzer et al., 2017; Wutz et al., 2017)). Proper function of the SMC machinery is vital to chromosome organization and compaction. Improper chromosome compaction and segregation can lead to anaphase bridges in eukaryotes (Charbin et al., 2014; Green et al., 2012; Hagstrom et al., 2002; Nagasaka et al., 2016; Piskadlo et al., 2017; Steffensen et al., 2001), and mispositioning of origins of replication in prokaryotes (Wang et al., 2014), all of which might cause aneuploidy (or anucleate cells in bacteria) and DNA damage (*e.g.*, (Fenech et al., 2011; Martin et al., 2016; Wang et al., 2013)). Additionally, the loss of interphase chromosome structure in vertebrates by loss of cohesin SMC complexes can affect gene expression (*e.g.*, (Bompadre and Andrey, 2019; Cuartero et al., 2018; Delaneau et al., 2019; Lupiáñez et al., 2015; Merkenschlager and Nora, 2016; Nora et al., 2017; Rao et al., 2017; Schoenfelder and Fraser, 2019; Schwarzer et al., 2017; Seitan et al., 2013)). Similarly, mutations that perturb cohesin or condensin can lead to human developmental

disorders, such as Cornelia de Lange syndrome (de Lange, 1933) and microcephaly (Martin et al., 2016).

Recent *in vitro* imaging studies showed that loop extrusion by *S. cerevisiae* condensin SMC complexes is purely one-sided (Ganji et al., 2018). To determine the biophysical implications and to test the generality of this striking molecular observation, we explored whether one-sided loop extrusion could explain SMC-dependent phenomena observed *in vivo* for a range of organisms beyond *S. cerevisiae*. These phenomena included mitotic chromosome compaction in vertebrates, formation of TADs and dots (corner peaks) in mammalian interphase Hi-C maps, and juxtaposition of chromosome arms in rapidly growing bacteria. Our work, along with recent theoretical modelling (Banigan and Mirny, 2019; Miermans and Broedersz, 2018), indicates that pure one-sided loop extrusion does not generically reproduce these three phenomena, except under specific conditions. Therefore, biophysical capabilities beyond those observed for yeast condensins should be present for other organisms. Indeed, recent experimental evidence suggests that pairs of yeast condensins may be able to cooperatively grow loops bidirectionally (Kim et al., 2019), while human condensins can perform either one- or two-sided loop extrusion (Kong et al., 2019; Moevus, 2019). Thus, we explored simple variations of the pure one-sided loop extrusion model and identified a class of one-sided extrusion models that can reproduce *in vivo* experimental observations (**Table 1**). Our results suggest modes of loop extrusion that might be observed in future experiments.

A framework for modeling SMC complex dynamics

We focused on several variations of the one-sided loop extrusion model and investigated the consequences for 3D chromosome organization (**Table 1**). Our aim was not to exhaustively enumerate all possible model variations of one-sided extrusion. Instead, we sought to obtain and evaluate a set of minimalistic requirements to explain experimental data. We modeled SMC complexes as LEFs with two subunits with distinct dynamics; subunits could be either active (*i.e.*, moving processively), inactive and anchored, or inactive but diffusive. Within this framework of varying the dynamics of the subunits, we primarily focused on the following models for LEFs: 1) one subunit active, the other subunit inactive and anchored (“pure one-sided”), 2) one subunit active, the other subunit inactive but diffusive (“semi-diffusive”), 3) one subunit active, the other subunit anchored, with kinetic interchange of active and anchored subunits (“switching”). We also considered several related variants for each chromosome organization scenario, such as preferential loading at CTCF by one-sided cohesins during interphase. As a point for comparison, we quantitatively compared all results with those of two-sided extrusion, which previous works have shown to recapitulate key experimental observations (Alipour and Marko, 2012; Brandão et al., 2019; Fudenberg et al., 2016; Goloborodko et al., 2016a, 2016b; Miermans and Broedersz, 2018; Sanborn et al., 2015).

Unlooped chromatin from one-sided extrusion hinders eukaryotic chromosome compaction and organization

Our modeling demonstrates that the ability to robustly eliminate unlooped gaps is essential to the chromosome-organizing role of LEFs. As a result, models in which gaps persist in steady state, such as the pure one-sided model, fail to reproduce hallmarks of chromosome organization found in several physiological scenarios. One-sided extrusion generally does not reproduce mitotic chromosome compaction and chromatid segregation or hallmarks of interphase Hi-C maps, without further assumptions beyond what has been observed experimentally. Importantly, even dynamic LEF turnover (*i.e.*, allowing dynamic chromatin unbinding with uniform rebinding) does not eliminate gaps because LEF unbinding (and even LEF binding) can introduce new gaps. Instead, chromosome compaction, resolution, and interphase organization can readily be explained by physical mechanisms that either eliminate gaps by turning one-sided extrusion into effectively two-sided extrusion (*e.g.*, as in the switching model) or suppress the creation of gaps (*e.g.*, by biased loading at boundaries).

In the case of mitotic chromosome compaction, linear compaction by pure one-sided loop extrusion is limited to ~10-fold because it unavoidably leaves gaps between SMC complexes (**Figure 2 c (i), (ii)** and (Banigan and Mirny, 2019)). By simulations, we showed that 10-fold linear compaction is not sufficient to reproduce the classical 3D shapes of mitotic chromatids and chromosomes are volumetrically compacted at most twofold in 3D (**Figure 2 b, c (iii)**). This defect in 3D compaction leads to defects in mitotic chromosome resolution (**Figure 2 b, c (iv)**). Allowing the SMC complexes' anchor points to diffuse (*i.e.*, slide) along chromosomes also does not close gaps because loop formation is opposed by the conformational entropy of the formed loop (**Figure 2 d (ii)** and **Figure 2 - figure supplement 3**), and therefore, the LEFs cannot generate a sufficient increase in linear compaction (**Figure 2 d (i)**). Uncompacted gaps are pervasive, so simply adding a small fraction of two-sided LEFs is unable to sufficiently compact chromosomes; *in vivo* levels of compaction requires >80% two-sided LEFs (**Figure 2 - figure supplement 2**, (Banigan and Mirny, 2019)). Similarly, a model in which LEFs are effectively two-sided, such as the switching model in which the active and inactive subunits dynamically switch, can generate greater than twofold 3D compaction and clear resolution of sister chromatids (**Figure 2 e (iii), (iv)**), as observed *in vivo*.

For interphase organization in higher eukaryotes, the ability of one-sided loop extrusion to reproduce major features of Hi-C maps is more complicated. We found that one-sided extrusion with uniform association and dissociation of LEFs can generate TADs (**Figure 3 b,** right) and "stripes" (or "flames," "tracks," or "lines") (Fudenberg et al., 2017, 2016; Vian et al., 2018) on Hi-C maps (**Figure 3 a**). However, one-sided extrusion cannot reliably bring CTCF barriers together, and thus, cannot generate the dots (corner peaks) that are prominent features of Hi-C and micro-C maps (Krietenstein et al., 2019) and are reproduced by two-sided extrusion (**Figure 3 b,** right and **Figure 3 - figure supplement 2**). The presence of unavoidable gaps between LEFs and between LEFs and barriers is the reason for this deficiency. This can be remedied by

introducing a comparable number of two-sided LEFs to close gaps **(Figure 3 d,** right). One-sided extrusion alone, however, can reproduce dots when undergoing frequent stochastic switches in translocation direction, turning one-sided into effectively two-sided extrusion. Other mechanisms to generate two-sided or effectively two-sided extrusion have also been proposed (Kim et al., 2019; Kong et al., 2019; Moevus, 2019), and gap closure may be achieved by several other mechanisms, as we discuss below in the subsection "Molecular evidence and plausibility of different modes of loop extrusion." Another strategy to eliminate gaps between boundaries and generate dots is to have strongly (>100-fold) biased loading of LEFs at barriers. Loading of cohesin at CTCF sites has been proposed since the two were found to colocalize (Nichols and Corces, 2015; Rubio et al., 2008). Available experimental evidence, however, argues against loading at CTCF sites; it was previously shown that CTCF is dispensable for cohesin loading (Parelho et al., 2008; Wendt et al., 2008), and more recently, CTCF-degradation experiments appear to have little effect on the levels of chromatin-associated cohesin (Busslinger et al., 2017; Nora et al., 2017) and the extent of loop extrusion (Fudenberg et al., 2017).

Bacterial data suggests an "effectively two-sided" extrusion process

In many bacteria, bSMCs loaded near the origin of replication (by the *parABS* system) generate contacts centered about the *ori-ter* axis, which is visible in Hi-C maps as a secondary diagonal (Böhm et al., 2019; Le et al., 2013; Marbouty et al., 2014; Umbarger et al., 2011; Wang et al., 2017, 2015). The challenge for one-sided loop extrusion models in bacteria is to explain how one-sided (*i.e.*, asymmetric) LEF translocation might generate symmetrically aligned contacts between chromosome arms. Pure one-sided extrusion does not work because it creates a "+"-shape on the contact map instead of a secondary diagonal (**Figure 4 c** and (Miermans and Broedersz, 2018)). Furthermore, we find that allowing diffusion of the anchor point generally does not help because this type of asymmetric extrusion cannot promote symmetric juxtaposition of the chromosome arms.

The switching model, however, with a switching time on the order of seconds (< 10 s for *B. subtilis* and < 20 s for *C. crescentus*, *i.e.*, rates $k_{switch} \gtrsim 0.1\ s^{-1}$; **Figure 4 d**) exhibits the desired effectively two-sided property and naturally creates the desired symmetry of contacts between left and right chromosome arms. Interestingly, if bSMCs function by one-sided extrusion with switching, this constraint suggests that bSMCs can switch their direction of extrusion within a few ATPase cycles (the *B. subtilis* SMC complex has an ATPase rate of 0.7 ATP/s). Switching, however, has not been observed in single-molecule experiments with yeast condensin SMC complexes, and such fast switching may appear as two-sided extrusion *in vitro*. We note that it was recently suggested that *B. subtilis* SMCs have two independent motor activities for extrusion (Brandão et al., 2019; Wang et al., 2017); this observation is consistent with either two-sided extrusion or one-sided extrusion with rapid switching. Thus, our model suggests that microscopically one-sided extrusion can explain juxtaposition of chromosome arms, provided that bSMCs act as effectively two-sided extruders.

Molecular evidence and plausibility of different modes of loop extrusion

Our work identifies two requirements for loop extrusion by SMC complexes to generate known chromosome structures. First, unlooped chromatin gaps between SMC complexes must be closed in order to compact mitotic chromosomes, and they occasionally must be closed between extrusion barriers during interphase to generate enrichment of CTCF-CTCF interactions. Second, particularly in prokaryotes, we find that extrusion must be two-sided or effectively two-sided in order to juxtapose bacterial chromosome arms. Several molecular mechanisms can give rise to such effectively two-sided, gap-closing extrusion. Based on the available experimental evidence, we also considered several physical factors and additional models, discussed below.

Time and energy requirements for compaction by loop extrusion

Whether loop extrusion can compact and resolve chromosomes within physiological limits is a persistent question for chromosome organization in higher eukaryotes. Previous work on two-sided loop extrusion (Goloborodko et al., 2016a) showed that LEFs can compact and resolve chromosomes of higher eukaryotes (~100 Mb in length) for physiological densities of LEFs (1 per d=10-30 kb (Fukui and Uchiyama, 2007; Takemoto et al., 2004; Walther et al., 2018)). Compaction and resolution are completed within a few (~5) residence times ($1/k_{unbind}$~ 2-10 min (Gerlich et al., 2006a; Terakawa et al., 2017; Walther et al., 2018)), provided that extrusion is fast, *i.e.*, v>0.2 kb/s (Goloborodko et al., 2016a). The extrusion rate of v≈1 kb/s recently observed *in vitro* (Ganji et al., 2018; Kong et al., 2019) confirms that loop extrusion is sufficiently rapid to compact eukaryotic chromosomes during prophase and prometaphase. Moreover, this rate is consistent with expectations from studies of the molecular dynamics of loop-extruding SMC complexes (Diebold-Durand et al., 2017; Marko et al., 2019).

Furthermore, we can estimate an upper bound on the energy required to compact human chromosomes. Conservatively estimating that condensin or cohesin require two ATP per extrusion step and several (~5) attempts to traverse each nucleosome (~150 bp), the ATP cost to extrude 6 Gb is of order 10 x (6 x 10^9 / 150) ~ 10^8. This upper limit estimate is still less than the ~10^9 ATP present in the cell (Traut, 1994) and less than the ~10^9 ATP/s that the cell produces (Flamholz et al., 2014). We conclude that genome compaction and organization by loop extrusion is energetically feasible.

Attractive interactions between LEFs

It has previously been suggested that 3D attractive interactions between LEFs could facilitate compaction of mitotic chromosomes (Sakai et al., 2018). Our results, along with previous work on polymer combs suggests otherwise (Fytas and Theodorakis, 2013; Sheiko et al., 2004). It is possible that SMC complexes may attract each other, but such interactions must be weak enough that the chromosome does not collapse into a spherically symmetric polymer. Even with weak interactions, however, gaps created by one-sided extrusion cannot be closed, and mitotic chromosomes cannot be formed (**Figure 2 - figure supplement 5**). Thus, 3D interactions

cannot be the mechanism of chromatin gap closure, and thus, they cannot be essential for mitotic chromosome compaction.

Oligomerization of SMC complexes

SMC complex oligomerization could facilitate chromosome organization by suppressing gap formation and/or promoting symmetric extrusion in various scenarios. In eukaryotes, *in situ* amino acid crosslinking (Barysz et al., 2015) and *in vitro* gel filtration (Keenholtz et al., 2017) suggest that condensins can oligomerize. Several experiments similarly suggest that cohesin may form oligomeric complexes *in vivo* (Cattoglio et al., 2019; Eng et al., 2015; Zhang et al., 2008). Formation of such complexes could lead to effectively two-sided extrusion and gapless chromosome compaction. In prokaryotes, such as *E. coli* (which have MukBEF complexes, SMC complex homologs), experiments show that MukBEF forms dimers of complexes (Badrinarayanan et al., 2012) linked by the kleisin molecule, MukF (Zawadzka et al., 2018). MukBEF complexes promote long-ranged contacts within *E. coli* chromosome arms (Lioy et al., 2018), and they are proposed to function by two-sided loop extrusion. Dimerization has also been suggested for other bacterial SMC complexes (Brandão et al., 2019; Diebold-Durand et al., 2017; Tran et al., 2017; Wang et al., 2018), but it is still unknown whether bSMCs in well studied organisms like *C. crescentus and B. subtilis* dimerize *in vivo*. Functional dimerization of bSMCs *in vivo* could be directly tested by photobleaching experiments with endogenous fluorescently tagged versions of bSMC*,* as in (Badrinarayanan et al., 2012). Additionally, to determine whether MukBEF dimerization is needed for DNA loop formation, we suggest a Hi-C experiment on a MukBEF mutant deficient in dimerization. If long-ranged chromosome interactions and proliferation under fast-growth conditions persist, then dimerization is not required for MukBEF function. These experiments could therefore investigate the possible functional role of SMC complex oligomerization in loop extrusion.

“Z-loops” and two-sided extrusion

Recent single-molecule experiments have reported the first observations of two-sided and effectively two-sided loop extrusion. It has been shown that a large fraction of human condensin complexes perform two-sided DNA loop extrusion *in vitro* (Kong et al., 2019). This finding is consistent with predictions of previous theory (Banigan and Mirny, 2019) and new simulations (**Figure 2 - figure supplement 2**) showing that such large fractions of two-sided LEFs are needed for 1000-fold linear chromatin compaction and robust 3D compaction of mitotic chromosomes.

Other single-molecule experiments have shown that yeast condensins can form “Z-loops” that act as effectively two-sided extruders (Kim et al., 2019). We simulated and analyzed a simple realization of this scenario, in which condensins can pass each other as they translocate along DNA. This leads to loop coverage that increases exponentially with λ/d and compacted rod-like chromosomes (**Figure 2 f-g**). However, our model for Z-loops generates many pseudoknots, and thus, linear spatial ordering of the mitotic chromosome is not maintained on length scales comparable to the loop size, $\ell \approx \lambda$, which may be >100 kb (as estimated from measured

condensin speed (Ganji et al., 2018; Kim et al., 2019) and turnover rate (Gerlich et al., 2006a; Terakawa et al., 2017; Walther et al., 2018)). Moreover, several questions remain about the compaction ability and *in vivo* relevance of Z-loops. We assumed that each LEF may traverse any other LEF that it encounters, but it is unknown how Z-loops actually interact. A more restrictive set of traversal rules could severely limit linear compaction. For example, if each active subunit can only traverse a single anchored subunit, then linear compaction is limited to 50-fold (following arguments for the "weak pushing" model, see **Supplemental File 1** and **Figure 2 - figure supplement 3**). In addition, it is unknown how Z-loop formation is altered when condensins must extrude chromatin instead of DNA. Thus, while our preliminary modeling suggests that effective two-sided extrusion by Z-loops might compact mitotic chromosomes, a number of experimental and theoretical factors remain unexplored.

Predictions and suggestions for future experiments

In **Table 1**, we list possible mechanisms of loop extrusion and whether they are able to reproduce *in vivo* experimental observations; however, many of these mechanisms have not yet been observed or tested. Single-molecule experiments (Ganji et al., 2018; Kong et al., 2019) could assay different types of SMC complexes from a range of organisms in order to establish which loop extrusion models are applicable. We predict that SMC complexes *in vivo* may constitute effectively two-sided motors or exhibit biased loading in order to robustly organize and compact chromatin. However, a variety of microscopic (molecule-level) modes of extrusion may achieve the same macroscopic organization of the chromosomal DNA.

We make several testable predictions. First, if switching of extrusion direction is observed, switching should be fast (occurring at least once per 10 s for bSMCs and at least once per minute for human SMC complexes cohesins and condensins). In addition, we predict that if a mixture of one-sided and two-sided extrusion is observed for a population of SMC complexes, then the fraction of two-sided extrusion should be at least 50% for cohesin and at least 80% for condensin (**Table 1**). We also predict that bSMCs from eubacteria are either two-sided monomeric complex or a dimer that translocates.

A few other types of experiments are critical to perform at the single-molecule level *in vitro*; these would be difficult to test *in vivo* by microscopic and biochemical methods. We suggest: 1) testing how SMC complexes interact with one another when they meet on the same chromatin/DNA substrate *in vivo*, as we show that LEF traversal can lead to effective compaction; 2) testing whether/what fraction of SMC complexes do one-sided or two-sided extrusion under different conditions, such as at various salt concentrations and/or with molecular crowding agents; and 3) testing whether specific factors, such as chromatin conformations (*e.g.*, supercoils, or Holliday junctions) or proteins (*e.g.*, other SMC complexes or CTCF), affect mechanisms of extrusion.

Finally, we note that there may be differences in functionality among condensins of different species or physiological scenarios. For example, it has been hypothesized that yeast

condensins could be one-sided because they do not need to linearly compact mitotic chromosomes 1000-fold (Banigan and Mirny, 2019). If yeast condensin is fundamentally different from human condensin in function, its use in cell-free chromosome assembly systems (Shintomi et al., 2017, 2015) should result in long, poorly folded chromosomes relative to those with condensin II only. Similarly, mutations that bias condensin activity towards one-sided extrusion could lead to catastrophic under-compaction of human chromosomes, failure to decatenate chromosomes (Martin et al., 2016), DNA damage, aneuploidy, developmental disorders (Martin et al., 2016), and cancer (Mazumdar et al., 2015; Woodward et al., 2016).

Conclusion

The loop extrusion model has been hypothesized to explain a variety of chromosome organization phenomena, but until recently had remained a hypothesis. Experimental work on yeast condensins (Ganji et al., 2018; Kim et al., 2019) has observed that loop extrusion by yeast condensins occurs in a one-sided manner. Theory and simulations of one-sided loop extrusion (Banigan and Mirny, 2019; Miermans and Broedersz, 2018) challenge the generality of this observation. We have shown that pure one-sided loop extrusion generally is unable to reproduce a variety of chromosome organization phenomena in different organisms and scenarios. Instead, loop extrusion should be “effectively two-sided” and/or have the ability to robustly eliminate unlooped chromatin gaps to organize chromosomes; in accord with this, recent experimental data indicate that human condensins are capable of acting in a two-sided loop manner (Kong et al., 2019). Additionally, among the models we explored, the switching model is an example that meets these requirements. Nonetheless, experimental evidence suggests that different organisms are likely to achieve macroscopic chromosome organization through diverse microscopic mechanisms. While loop extrusion remains a unifying model for chromosome organization across different domains of life, various to-be-determined microscopic mechanisms could underlie these phenomena.

Methods

Basic model

Stochastic simulations of loop-extrusion dynamics are performed with N LEFs on a lattice of length L. There are several types of events. LEFs bind to the chromatin lattice at rate k_{bind} by occupying two adjacent lattice sites and LEFs unbind at rate k_{unbind}. When an active subunit of a LEF makes a step, it occupies the site that was immediately adjacent to it, which frees the lattice site that it previously occupied. Directional stepping by an active subunit occurs at speed v and proceeds in the direction away from the other LEF subunit. Diffusive stepping occurs in either direction at loop-size-dependent rate $v^{\pm}_{\text{diff}}(\ell)$. When a one-sided LEF switches its active extrusion direction, the active subunit becomes passive and vice versa. Switches occur at a rate k_{switch}. In interphase simulations, LEF subunits may stall upon encountering a correctly oriented CTCF site. This occurs with probability p_{stall}. Each simulation consists of a chromatin polymer with L sites and a fixed number, N_b, of LEFs that populate the sites at low density, $N_b/L \leq 0.05$.

Event-driven (Gillespie) simulations for linear compaction

1D stochastic simulations of loop-extrusion dynamics modeling mitotic chromosome compaction for pure one-sided, two-sided, switching, and pushing models are performed with N LEFs on a lattice of length L, with L=60000 sites and 100<N<3000. Each site is taken to be a=0.5 kb.

We use the Gillespie algorithm to determine the time that each kinetic event -- binding, unbinding, directional stepping, and switching -- occurs (Gillespie, 1977; Goloborodko et al., 2016b). Events are executed in temporal order, and after an event occurs, we compute the lifetimes of new events that become permissible (*e.g.*, a LEF step that becomes possible because another LEF has moved). Simulations are run for t_{sim}=400 max((1/k_{unbind}+1/k_{bind}), L/v+1/k_{bind}), and data is recorded for the second half of the simulation, long after the onset of the steady-state, for at least three simulations per parameter combination.

Fixed-time-step simulations for LEF dynamics

For 1D simulations of chromosome compaction in the semi-diffusive model, 1D simulations of compaction with LEF traversal, 3D polymer simulations of chromosome compaction with all models, interphase TAD formation, and 1D simulations of LEF dynamics on bacterial chromosomes, we use a fixed-time-step Monte Carlo algorithm instead of the Gillespie algorithm. This algorithm facilitates coupling of LEF kinetics to the loop architecture (for the semi-diffusive model) and/or 3D polymer conformation (for polymer simulations). Here, each event is modeled as a Poisson process; at each LEF time step dt, an event is executed with probability $k_i dt$, where k_i is the rate of event i. In the semi-diffusive model, the passive diffusive stepping rate for a LEF is $v^{\pm}_{diff}(\ell)=v_{diff}\, e^{\mp(3/2)\,(a\,/\,\ell)}$, which is updated when the size of either the loop associated with the LEF or any loop in which the LEF is nested changes in size. The expression for $v^{\pm}_{diff}(\ell)$ is a discretization of $v^{\pm}_{diff}(\ell)=v_{diff}\, e^{\mp f\ a\ /\ kT}$. Here, f = -dU/dℓ =(3/2) kT ln(ℓ/a) defines the entropic force arising from loop configurational entropy (*e.g.*, see (Brackley et al., 2017)).

Simulations of mitotic chromosomes

For fixed-time-step simulations of mitotic chromosomes, L=30000, N=750, and a=0.5 kb. At least three simulations per parameter combinations are run for >40 residence times, and linear compaction is measured after 20 residence times. Probe radius r_{hull}= 600 nm was used to calculate concave hulls.

Simulations of interphase chromosomes

For simulations of interphase, we simulate a chain with three different TAD sizes of 100, 200, and 400 monomers. This system of 700 monomers in total is repeated 6 or 8 times, giving a total size of 4200 monomers (for computing dot strengths) or 5600 monomers (for computing contact maps and scalings). When LEFs encounter a CTCF site, they are stalled (i.e. they stop moving until they are unloaded), with a probability of 80% (Fudenberg et al., 2016). From the

scalings, we determined that 1 monomer corresponds to 2 kb (**Figure 3 - figure supplement 1**).

We used a total of 4000 conformations to compute contact maps, scalings or dot strengths. For computing the contact maps, we used a contact radius of 5 monomers. Dot strengths are computed as follows: first, we compute observed-over-expected of a contact map (we divide out the distance dependence, by dividing each diagonal by its average (Lieberman-Aiden et al., 2009)), then we compute the strength of a dot of a particular TAD (**Figure 3 - figure supplement 2**) and last, we compute the average of all the dots (each of which appears 6 times on one map).

In contrast to mitotic compaction, λ and d are varied separately for interphase chromosomes, because the dot strengths depend on λ and d separately, as well as the distance between two CTCF sites, d_{CTCF}. Based on contact probability scalings (**Figure 3 - figure supplement 1**) and experimental observations, we consider a separation between loop extruders of d=200 kb and a processivity of λ=200 kb (Cattoglio et al., 2019; Fudenberg et al., 2016; Holzmann et al., 2019) in the main text, and we consider other parameter values in the supplemental figures. Furthermore, we choose typical TAD sizes of 200 and 400 kb (Rao et al., 2014). For simulations of Wapl KO conditions, we use d=200 kb and λ=2 Mb (Gassler et al., 2017; Nuebler et al., 2018).

Simulations of bacterial chromosomes

We simulate loop extrusion on bacterial chromosomes using the fixed-time-step simulations for LEF dynamics described above. LEFs are allowed to randomly load on a lattice of L=4000 sites, where each lattice site corresponds to ~1 kb of DNA. LEFs have a strong bias to bind one site at the center of the lattice to mimic the effect of a single *parS* site near the origin of replication in bacterial chromosomes. The relative probability of loading at the simulated *parS* site was ~40,000 times stronger than that of every other site, *i.e.*, if the relative probability of loading at the simulated *parS* is 1, then the total relative probability to load on *any* other site is 0.1 L. As a result, the overall preference to bind the *parS* site over all other genomic loci is approximately 10-fold.

Bacterial LEFs were simulated as deterministic extruders with a stochastic dissociation rate $k_{unbind}=2/L$ to approximate the steady decrease in bSMC density away from the *ori* observed via ChIP-seq (*i.e.*, bSMC density at the *ter* region is ~1/3 of the value at *ori*) (Wang et al., 2017). In addition to a stochastic (position-independent) dissociation rate, LEFs automatically unbind if one of the subunits reached the edge of the lattice, *i.e.*, the *ter* region; *ter* was set to lattice positions 0-3 and 3996-3999 (*i.e.*, diametrically opposite to the *parS* site at lattice site 2000).

Polymer simulations with OpenMM

To model the 3D dynamics of polymers loaded with LEFs, we performed polymer molecular dynamics simulations in OpenMM (Eastman et al., 2017, 2013; Eastman and Pande, 2010)

using a custom, publicly available library, openmm-polymer (available at http://bitbucket.org/mirnylab/openmm-polymer), coupled with the fixed-time-step LEF simulations described above and in (Fudenberg et al., 2016; Goloborodko et al., 2016a).

In the polymer simulation, a LEF crosslinks the sites that it occupies together. LEF positions are evolved as described above. After each time step of LEF dynamics, the polymer simulation is evolved via Langevin dynamics for 200 or 250 time steps (for interphase and mitosis, respectively) with dt=80.

Polymers are constructed of L consecutive subunits bonded via the pairwise potential:

$$U_b(r) = \frac{k}{2}(r-b)^2$$

where $r=r_i-r_j$ is the displacement between monomers i and j, $k= 2kT / \delta^2$ is the spring constant, δ=0.1, and b is the diameter of a monomer. For mitotic chromosome simulations, b=30 nm; for other scenarios, it is unnecessary to assign a value to b. Monomers crosslinked by a LEF are held together by the same potential. Weakly repulsive excluded volume interactions between monomers are modeled as:

$$U_{exc}(r) = \frac{\varepsilon_{exc}}{\varepsilon_m}\left(\frac{r}{\sigma} r_m\right)^{12}\left(\left(\frac{r}{\sigma} r_m\right)^2 - 1\right) + \varepsilon_{exc},$$

for $r<\sigma$ with σ=1.05b, $r_m = \sqrt{6/7}$, ε_m =46656/823543, and ε_{exc} =1.5 kT. For simulations of mitotic chromosomes with 3D attractive interactions, monomers interact through the potential:

$$U_{att}(r) = -\frac{\varepsilon}{\varepsilon_m}\left(\frac{r}{\sigma} r_m\right)^{12}\left(\left(\frac{r}{\sigma} r_m\right)^2 - 1\right) + \varepsilon,$$

for $\sigma < r < 2b$ and ε is a parameter to be varied.

At the beginning of each simulation, the polymer is initialized as a random walk and monomers are initialized with normally distributed velocities, so that the temperature is T. The system is thermostatted by intermittent rescaling of velocities to maintain temperature T.

Contact probability calculations in the Gaussian chain approximation

To compute contact maps for bacterial chromosomes, the contact frequency was calculated from the equilibrium contact probability for a Gaussian chain**.** This theoretical model agrees well with polymer molecular dynamics simulations (**Supplemental File 1**)**.** Briefly, contact probability between two sites on a Gaussian chain scales with $s^{-3/2}$, where s is the linear distance between the sites, excluding any loops between the two sites. Sites within the same loop obey this scaling relation with an effective s, s_{eff}, substituted for s in the scaling relation; $s_{eff}=s(1-s/\ell)$, where ℓ is the loop size. For sites in different loops, s in the scaling relation is replaced by the sum of the effective lengths of the regions connecting the two sites (see **Supplemental File 1** for details). These relative contact probabilities are used to compute the contact maps for bacterial chromosome simulations. Contact maps are generated using contacts from 50,000-100,000 different LEF conformations.

Acknowledgements

We thank current and former members of the Mirny group for ongoing discussions and critical feedback; we particularly thank Anton Goloborodko and Maxim Imakaev for helpful discussions and sharing code and Aleksandra Galitsyna for discussions. We also thank Sergey Belan, Xavier Darzacq, Cees Dekker, and Christian Haering for helpful discussions. This work was supported by the NIH Center for 3D Structure and Physics of the Genome of the 4DN Consortium (U54DK107980) and the Physical Sciences-Oncology Center (U54CA193419). EJB, AAB, HBB, and LAM were also supported by the NIH through GM114190.

References

Alipour E, Marko JF. 2012. Self-organization of domain structures by DNA-loop-extruding enzymes. *Nucleic Acids Res* **40**:11202–11212.

Badrinarayanan A, Reyes-Lamothe R, Uphoff S, Leake MC, Sherratt DJ. 2012. In vivo architecture and action of bacterial structural maintenance of chromosome proteins. *Science* **338**:528–531.

Banigan EJ, Mirny LA. 2019. Limits of chromosome compaction by loop-extruding motors. *Physical Review X* **9**:031007.

Barysz H, Kim JH, Chen ZA, Hudson DF, Rappsilber J, Gerloff DL, Earnshaw WC. 2015. Three-dimensional topology of the SMC2/SMC4 subcomplex from chicken condensin I revealed by cross-linking and molecular modelling. *Open Biol* **5**:150005.

Benedetti F, Racko D, Dorier J, Burnier Y, Stasiak A. 2017. Transcription-induced supercoiling explains formation of self-interacting chromatin domains in S. pombe. *Nucleic Acids Res* **45**:9850–9859.

Böhm K, Giacomelli G, Schmidt A, Imhof A, Koszul R, Marbouty M, Bramkamp M. 2019. Chromosome organization by a conserved condensin-ParB system in the actinobacterium Corynebacterium glutamicum. *bioRxiv*. doi:10.1101/649749

Bompadre O, Andrey G. 2019. Chromatin topology in development and disease. *Curr Opin Genet Dev* **55**:32–38.

Bonev B, Mendelson Cohen N, Szabo Q, Fritsch L, Papadopoulos GL, Lubling Y, Xu X, Lv X, Hugnot J-P, Tanay A, Cavalli G. 2017. Multiscale 3D Genome Rewiring during Mouse Neural Development. *Cell* **171**:557–572.e24.

Brackley CA, Johnson J, Michieletto D, Morozov AN, Nicodemi M, Cook PR, Marenduzzo D. 2017. Nonequilibrium Chromosome Looping via Molecular Slip Links. *Phys Rev Lett* **119**:138101.

Brahmachari S, Marko JF. 2019. Chromosome disentanglement driven via optimal compaction of loop-extruded brush structures. *bioRxiv*. doi:10.1101/616102

Brandão HB, Wang X, Paul P, van den Berg A, Rudner DZ, Wang X, Mirny LA. 2019. RNA polymerases as moving barriers to condensin loop extrusion. *Proceedings of the National Academy of Sciences* **116**:20489–20499.

Britton RA, Lin DC, Grossman AD. 1998. Characterization of a prokaryotic SMC protein involved in chromosome partitioning. *Genes Dev* **12**:1254–1259.

Bürmann F, Gruber S. 2015. SMC condensin: promoting cohesion of replicon arms. *Nat Struct Mol Biol* **22**:653–655.

Busslinger GA, Stocsits RR, van der Lelij P, Axelsson E, Tedeschi A, Galjart N, Peters J-M. 2017. Cohesin is positioned in mammalian genomes by transcription, CTCF and Wapl. *Nature* **544**:503–507.

Cattoglio C, Pustova I, Walther N, Ho JJ, Hantsche-Grininger M, Inouye CJ, Hossain MJ, Dailey GM, Ellenberg J, Darzacq X, Tjian R, Hansen AS. 2019. Determining cellular CTCF and cohesin abundances to constrain 3D genome models. *Elife* **8**. doi:10.7554/eLife.40164

Charbin A, Bouchoux C, Uhlmann F. 2014. Condensin aids sister chromatid decatenation by topoisomerase II. *Nucleic Acids Res* **42**:340–348.

Cuartero S, Weiss FD, Dharmalingam G, Guo Y, Ing-Simmons E, Masella S, Robles-Rebollo I, Xiao X, Wang Y-F, Barozzi I, Djeghloul D, Amano MT, Niskanen H, Petretto E, Dowell RD, Tachibana K, Kaikkonen MU, Nasmyth KA, Lenhard B, Natoli G, Fisher AG, Merkenschlager M. 2018. Control of inducible gene expression links cohesin to hematopoietic progenitor self-renewal and differentiation. *Nat Immunol* **19**:932–941.

Daban J-R. 2003. High concentration of DNA in condensed chromatin. *Biochem Cell Biol* **81**:91–99.

Delaneau O, Zazhytska M, Borel C, Giannuzzi G, Rey G, Howald C, Kumar S, Ongen H, Popadin K, Marbach D, Ambrosini G, Bielser D, Hacker D, Romano L, Ribaux P, Wiederkehr M, Falconnet E, Bucher P, Bergmann S, Antonarakis SE, Reymond A, Dermitzakis ET. 2019. Chromatin three-dimensional interactions mediate genetic effects on gene expression. *Science* **364**. doi:10.1126/science.aat8266

de Lange C. 1933. Sur un type nouveau de dégénération (typus Amstelodamensis). *Arch Méd Enfants* **36**:713–19.

de Wit E, Vos ESM, Holwerda SJB, Valdes-Quezada C, Verstegen MJAM, Teunissen H, Splinter E, Wijchers PJ, Krijger PHL, de Laat W. 2015. CTCF Binding Polarity Determines Chromatin Looping. *Mol Cell* **60**:676–684.

Diebold-Durand M-L, Lee H, Ruiz Avila LB, Noh H, Shin H-C, Im H, Bock FP, Bürmann F, Durand A, Basfeld A, Ham S, Basquin J, Oh B-H, Gruber S. 2017. Structure of Full-Length SMC and Rearrangements Required for Chromosome Organization. *Mol Cell* **67**:334–347.e5.

Dixon JR, Selvaraj S, Yue F, Kim A, Li Y, Shen Y, Hu M, Liu JS, Ren B. 2012. Topological domains in mammalian genomes identified by analysis of chromatin interactions. *Nature* **485**:376–380.

Earnshaw WC, Laemmli UK. 1983. Architecture of metaphase chromosomes and chromosome scaffolds. *J Cell Biol* **96**:84–93.

Eastman P, Friedrichs MS, Chodera JD, Radmer RJ, Bruns CM, Ku JP, Beauchamp KA, Lane TJ, Wang L-P, Shukla D, Tye T, Houston M, Stich T, Klein C, Shirts MR, Pande VS. 2013. OpenMM 4: A Reusable, Extensible, Hardware Independent Library for High Performance Molecular Simulation. *J Chem Theory Comput* **9**:461–469.

Eastman P, Pande VS. 2010. OpenMM: A Hardware Independent Framework for Molecular Simulations. *Comput Sci Eng* **12**:34–39.

Eastman P, Swails J, Chodera JD, McGibbon RT, Zhao Y, Beauchamp KA, Wang L-P, Simmonett AC, Harrigan MP, Stern CD, Wiewiora RP, Brooks BR, Pande VS. 2017. OpenMM 7: Rapid development of high performance algorithms for molecular dynamics. *PLoS Comput Biol* **13**:e1005659.

Eeftens JM, Bisht S, Kerssemakers J, Kschonsak M, Haering CH, Dekker C. 2017. Real-time detection of condensin-driven DNA compaction reveals a multistep binding mechanism. *EMBO J* **36**:3448–3457.

Elbatsh AMO, Kim E, Eeftens JM, Raaijmakers JA, van der Weide RH, García-Nieto A, Bravo S,

Ganji M, uit de Bos J, Teunissen H, Medema RH, de Wit E, Haering CH, Dekker C, Rowland BD. 2019. Distinct Roles for Condensin's Two ATPase Sites in Chromosome Condensation. *Molecular Cell* **76**. doi:10.1016/j.molcel.2019.09.020

Eng T, Guacci V, Koshland D. 2015. Interallelic complementation provides functional evidence for cohesin–cohesin interactions on DNA. *MBoC* **26**:4224–4235.

Eykelenboom JK, Gierliński M, Yue Z, Hegarat N, Pollard H, Fukagawa T, Hochegger H, Tanaka TU. 2019. Live imaging of marked chromosome regions reveals their dynamic resolution and compaction in mitosis. *J Cell Biol* **218**:1531–1552.

Fenech M, Kirsch-Volders M, Natarajan AT, Surralles J, Crott JW, Parry J, Norppa H, Eastmond DA, Tucker JD, Thomas P. 2011. Molecular mechanisms of micronucleus, nucleoplasmic bridge and nuclear bud formation in mammalian and human cells. *Mutagenesis* **26**:125–132.

Flamholz A, Phillips R, Milo R. 2014. The quantified cell. *Mol Biol Cell* **25**:3497–3500.

Fudenberg G, Abdennur N, Imakaev M, Goloborodko A, Mirny LA. 2017. Emerging Evidence of Chromosome Folding by Loop Extrusion. *Cold Spring Harb Symp Quant Biol* **82**:45–55.

Fudenberg G, Imakaev M, Lu C, Goloborodko A, Abdennur N, Mirny LA. 2016. Formation of Chromosomal Domains by Loop Extrusion. *Cell Rep* **15**:2038–2049.

Fukui K, Uchiyama S. 2007. Chromosome protein framework from proteome analysis of isolated human metaphase chromosomes. *Chem Rec* **7**:230–237.

Fytas NG, Theodorakis PE. 2013. Molecular dynamics simulations of single-component bottle-brush polymers with flexible backbones under poor solvent conditions. *J Phys Condens Matter* **25**:285105.

Ganji M, Shaltiel IA, Bisht S, Kim E, Kalichava A, Haering CH, Dekker C. 2018. Real-time imaging of DNA loop extrusion by condensin. *Science* **360**:102–105.

Gassler J, Brandão HB, Imakaev M, Flyamer IM, Ladstätter S, Bickmore WA, Peters J, Mirny LA, Tachibana K. 2017. A mechanism of cohesin‐dependent loop extrusion organizes zygotic genome architecture. *EMBO J* **36**:3600–3618.

Gerlich D, Hirota T, Koch B, Peters J-M, Ellenberg J. 2006a. Condensin I stabilizes chromosomes mechanically through a dynamic interaction in live cells. *Curr Biol* **16**:333–344.

Gerlich D, Koch B, Dupeux F, Peters J-M, Ellenberg J. 2006b. Live-cell imaging reveals a stable cohesin-chromatin interaction after but not before DNA replication. *Curr Biol* **16**:1571–1578.

Gibcus JH, Samejima K, Goloborodko A, Samejima I, Naumova N, Nuebler J, Kanemaki MT, Xie L, Paulson JR, Earnshaw WC, Mirny LA, Dekker J. 2018. A pathway for mitotic chromosome formation. *Science* **359**. doi:10.1126/science.aao6135

Gillespie DT. 1977. Exact stochastic simulation of coupled chemical reactions. *J Phys Chem* **81**:2340–2361.

Goloborodko A, Imakaev MV, Marko JF, Mirny L. 2016a. Compaction and segregation of sister chromatids via active loop extrusion. *Elife* **5**. doi:10.7554/eLife.14864

Goloborodko A, Marko JF, Mirny LA. 2016b. Chromosome Compaction by Active Loop Extrusion. *Biophys J* **110**:2162–2168.

Graham TGW, Wang X, Song D, Etson CM, van Oijen AM, Rudner DZ, Loparo JJ. 2014. ParB spreading requires DNA bridging. *Genes Dev* **28**:1228–1238.

Green LC, Kalitsis P, Chang TM, Cipetic M, Kim JH, Marshall O, Turnbull L, Whitchurch CB, Vagnarelli P, Samejima K, Earnshaw WC, Choo KHA, Hudson DF. 2012. Contrasting roles of condensin I and condensin II in mitotic chromosome formation. *J Cell Sci* **125**:1591–1604.

Guacci V, Hogan E, Koshland D. 1994. Chromosome condensation and sister chromatid pairing

in budding yeast. *J Cell Biol* **125**:517–530.

Guo Y, Xu Q, Canzio D, Shou J, Li J, Gorkin DU, Jung I, Wu H, Zhai Y, Tang Y, Lu Y, Wu Y, Jia Z, Li W, Zhang MQ, Ren B, Krainer AR, Maniatis T, Wu Q. 2015. CRISPR Inversion of CTCF Sites Alters Genome Topology and Enhancer/Promoter Function. *Cell* **162**:900–910.

Haarhuis JHI, van der Weide RH, Blomen VA, Yáñez-Cuna JO, Amendola M, van Ruiten MS, Krijger PHL, Teunissen H, Medema RH, van Steensel B, Brummelkamp TR, de Wit E, Rowland BD. 2017. The Cohesin Release Factor WAPL Restricts Chromatin Loop Extension. *Cell* **169**:693–707.e14.

Hagstrom KA, Holmes VF, Cozzarelli NR, Meyer BJ. 2002. C. elegans condensin promotes mitotic chromosome architecture, centromere organization, and sister chromatid segregation during mitosis and meiosis. *Genes Dev* **16**:729–742.

Hansen AS, Pustova I, Cattoglio C, Tjian R, Darzacq X. 2017. CTCF and cohesin regulate chromatin loop stability with distinct dynamics. *Elife* **6**. doi:10.7554/eLife.25776

Hassler M, Shaltiel IA, Haering CH. 2018. Towards a Unified Model of SMC Complex Function. *Curr Biol* **28**:R1266–R1281.

Hihara S, Pack C-G, Kaizu K, Tani T, Hanafusa T, Nozaki T, Takemoto S, Yoshimi T, Yokota H, Imamoto N, Sako Y, Kinjo M, Takahashi K, Nagai T, Maeshima K. 2012. Local nucleosome dynamics facilitate chromatin accessibility in living mammalian cells. *Cell Rep* **2**:1645–1656.

Hirano T. 2016. Condensin-Based Chromosome Organization from Bacteria to Vertebrates. *Cell* **164**:847–857.

Hirano T, Kobayashi R, Hirano M. 1997. Condensins, chromosome condensation protein complexes containing XCAP-C, XCAP-E and a Xenopus homolog of the Drosophila Barren protein. *Cell* **89**:511–521.

Hirano T, Mitchison TJ. 1994. A heterodimeric coiled-coil protein required for mitotic chromosome condensation in vitro. *Cell* **79**:449–458.

Holzmann J, Politi AZ, Nagasaka K, Hantsche-Grininger M, Walther N, Koch B, Fuchs J, Dürnberger G, Tang W, Ladurner R, Stocsits RR, Busslinger GA, Novák B, Mechtler K, Davidson IF, Ellenberg J, Peters J-M. 2019. Absolute quantification of cohesin, CTCF and their regulators in human cells. *Elife* **8**. doi:10.7554/eLife.46269

Hudson DF, Vagnarelli P, Gassmann R, Earnshaw WC. 2003. Condensin is required for nonhistone protein assembly and structural integrity of vertebrate mitotic chromosomes. *Dev Cell* **5**:323–336.

Jensen RB, Shapiro L. 1999. The Caulobacter crescentus smc gene is required for cell cycle progression and chromosome segregation. *Proc Natl Acad Sci U S A* **96**:10661–10666.

Keenholtz RA, Dhanaraman T, Palou R, Yu J, D'Amours D, Marko JF. 2017. Oligomerization and ATP stimulate condensin-mediated DNA compaction. *Sci Rep* **7**:14279.

Kerpedjiev P, Abdennur N, Lekschas F, McCallum C, Dinkla K, Strobelt H, Luber JM, Ouellette SB, Azhir A, Kumar N, Hwang J, Lee S, Alver BH, Pfister H, Mirny LA, Park PJ, Gehlenborg N. 2018. HiGlass: Web-based Visual Exploration and Analysis of Genome Interaction Maps. *Genome Biology* **19**:125.

Kim E, Kerssemakers J, Shaltiel IA, Haering CH, Dekker C. 2019. DNA-loop extruding condensin complexes can traverse one another. *bioRxiv*.

Kleine Borgmann LAK, Hummel H, Ulbrich MH, Graumann PL. 2013. SMC condensation centers in Bacillus subtilis are dynamic structures. *J Bacteriol* **195**:2136–2145.

Kong M, Cutts E, Pan D, Beuron F, Kaliyappan T, Xue C, Morris E, Musacchio A, Vannini A, Greene EC. 2019. Human condensin I and II drive extensive ATP–dependent compaction of nucleosome–bound DNA. *bioRxiv*. doi:10.1101/683540

Krietenstein N, Abraham S, Venev SV, Abdennur N, Gibcus J, Hsieh T-HS, Parsi KM, Yang L, Maehr R, Mirny LA, Dekker J, Rando OJ. 2019. Ultrastructural details of mammalian chromosome architecture. *bioRxiv*. doi:10.1101/639922

Kschonsak M, Merkel F, Bisht S, Metz J, Rybin V, Hassler M, Haering CH. 2017. Structural Basis for a Safety-Belt Mechanism That Anchors Condensin to Chromosomes. *Cell* **171**:588–600.e24.

Kueng S, Hegemann B, Peters BH, Lipp JJ, Schleiffer A, Mechtler K, Peters J-M. 2006. Wapl controls the dynamic association of cohesin with chromatin. *Cell* **127**:955–967.

Lawrence JB, Villnave CA, Singer RH. 1988. Sensitive, high-resolution chromatin and chromosome mapping in situ: presence and orientation of two closely integrated copies of EBV in a lymphoma line. *Cell* **52**:51–61.

Le TBK, Imakaev MV, Mirny LA, Laub MT. 2013. High-resolution mapping of the spatial organization of a bacterial chromosome. *Science* **342**:731–734.

Liang Z, Zickler D, Prentiss M, Chang FS, Witz G, Maeshima K, Kleckner N. 2015. Chromosomes Progress to Metaphase in Multiple Discrete Steps via Global Compaction/Expansion Cycles. *Cell* **161**:1124–1137.

Lieberman-Aiden E, van Berkum NL, Williams L, Imakaev M, Ragoczy T, Telling A, Amit I, Lajoie BR, Sabo PJ, Dorschner MO, Sandstrom R, Bernstein B, Bender MA, Groudine M, Gnirke A, Stamatoyannopoulos J, Mirny LA, Lander ES, Dekker J. 2009. Comprehensive mapping of long-range interactions reveals folding principles of the human genome. *Science* **326**:289–293.

Lioy VS, Cournac A, Marbouty M, Duigou S, Mozziconacci J, Espéli O, Boccard F, Koszul R. 2018. Multiscale Structuring of the E. coli Chromosome by Nucleoid-Associated and Condensin Proteins. *Cell* **172**:771–783.e18.

Lupiáñez DG, Kraft K, Heinrich V, Krawitz P, Brancati F, Klopocki E, Horn D, Kayserili H, Opitz JM, Laxova R, Santos-Simarro F, Gilbert-Dussardier B, Wittler L, Borschiwer M, Haas SA, Osterwalder M, Franke M, Timmermann B, Hecht J, Spielmann M, Visel A, Mundlos S. 2015. Disruptions of topological chromatin domains cause pathogenic rewiring of gene-enhancer interactions. *Cell* **161**:1012–1025.

Maeshima K, Eltsov M, Laemmli UK. 2005. Chromosome structure: improved immunolabeling for electron microscopy. *Chromosoma* **114**:365–375.

Marbouty M, Cournac A, Flot J-F, Marie-Nelly H, Mozziconacci J, Koszul R. 2014. Metagenomic chromosome conformation capture (meta3C) unveils the diversity of chromosome organization in microorganisms. *Elife* **3**:e03318.

Marbouty M, Le Gall A, Cattoni DI, Cournac A, Koh A, Fiche J-B, Mozziconacci J, Murray H, Koszul R, Nollmann M. 2015. Condensin- and Replication-Mediated Bacterial Chromosome Folding and Origin Condensation Revealed by Hi-C and Super-resolution Imaging. *Mol Cell* **59**:588–602.

Marko JF. 2009. Linking topology of tethered polymer rings with applications to chromosome segregation and estimation of the knotting length. *Phys Rev E Stat Nonlin Soft Matter Phys* **79**:051905.

Marko JF, De Los Rios P, Barducci A, Gruber S. 2019. DNA-segment-capture model for loop extrusion by structural maintenance of chromosome (SMC) protein complexes. *Nucleic Acids Res*, 47 6956–6972.

Marsden MP, Laemmli UK. 1979. Metaphase chromosome structure: evidence for a radial loop model. *Cell* **17**:849–858.

Martin C-A, Murray JE, Carroll P, Leitch A, Mackenzie KJ, Halachev M, Fetit AE, Keith C, Bicknell LS, Fluteau A, Gautier P, Hall EA, Joss S, Soares G, Silva J, Bober MB, Duker A,

Wise CA, Quigley AJ, Phadke SR, Deciphering Developmental Disorders Study, Wood AJ, Vagnarelli P, Jackson AP. 2016. Mutations in genes encoding condensin complex proteins cause microcephaly through decatenation failure at mitosis. *Genes Dev* **30**:2158–2172.

Mazumdar C, Shen Y, Xavy S, Zhao F, Reinisch A, Li R, Corces MR, Flynn RA, Buenrostro JD, Chan SM, Thomas D, Koenig JL, Hong W-J, Chang HY, Majeti R. 2015. Leukemia-Associated Cohesin Mutants Dominantly Enforce Stem Cell Programs and Impair Human Hematopoietic Progenitor Differentiation. *Cell Stem Cell* **17**:675–688.

Merkenschlager M, Nora EP. 2016. CTCF and Cohesin in Genome Folding and Transcriptional Gene Regulation. *Annu Rev Genomics Hum Genet* **17**:17–43.

Miermans CA, Broedersz CP. 2018. Bacterial chromosome organization by collective dynamics of SMC condensins. *J R Soc Interface* **15**:20180495.

Minnen A, Bürmann F, Wilhelm L, Anchimiuk A, Diebold-Durand M-L, Gruber S. 2016. Control of Smc Coiled Coil Architecture by the ATPase Heads Facilitates Targeting to Chromosomal ParB/parS and Release onto Flanking DNA. *Cell Rep* **14**:2003–2016.

Moevus CJ. 2019. Nucleosome Curtains and Their Application to the Study of DNA Condensation by Condensin. Columbia University.

Moriya S, Tsujikawa E, Hassan AKM, Asai K, Kodama T, Ogasawara N. 1998. A Bacillus subtilis gene-encoding protein homologous to eukaryotic SMC motor protein is necessary for chromosome partition. *Mol Microbiol* **29**:179–187.

Nagasaka K, Hossain MJ, Roberti MJ, Ellenberg J, Hirota T. 2016. Sister chromatid resolution is an intrinsic part of chromosome organization in prophase. *Nat Cell Biol* **18**:692–699.

Nasmyth K. 2001. Disseminating the genome: joining, resolving, and separating sister chromatids during mitosis and meiosis. *Annu Rev Genet* **35**:673–745.

Naumova N, Imakaev M, Fudenberg G, Zhan Y, Lajoie BR, Mirny LA, Dekker J. 2013. Organization of the mitotic chromosome. *Science* **342**:948–953.

Nichols MH, Corces VG. 2015. A CTCF Code for 3D Genome Architecture. *Cell* **162**:703–705.

Nora EP, Goloborodko A, Valton A-L, Gibcus JH, Uebersohn A, Abdennur N, Dekker J, Mirny LA, Bruneau BG. 2017. Targeted Degradation of CTCF Decouples Local Insulation of Chromosome Domains from Genomic Compartmentalization. *Cell* **169**:930–944.e22.

Nora EP, Lajoie BR, Schulz EG, Giorgetti L, Okamoto I, Servant N, Piolot T, van Berkum NL, Meisig J, Sedat J, Gribnau J, Barillot E, Blüthgen N, Dekker J, Heard E. 2012. Spatial partitioning of the regulatory landscape of the X-inactivation centre. *Nature* **485**:381–385.

Nuebler J, Fudenberg G, Imakaev M, Abdennur N, Mirny LA. 2018. Chromatin organization by an interplay of loop extrusion and compartmental segregation. *Proc Natl Acad Sci U S A* **115**:E6697–E6706.

Ono T, Losada A, Hirano M, Myers MP, Neuwald AF, Hirano T. 2003. Differential contributions of condensin I and condensin II to mitotic chromosome architecture in vertebrate cells. *Cell* **115**:109–121.

Parelho V, Hadjur S, Spivakov M, Leleu M, Sauer S, Gregson HC, Jarmuz A, Canzonetta C, Webster Z, Nesterova T, Cobb BS, Yokomori K, Dillon N, Aragon L, Fisher AG, Merkenschlager M. 2008. Cohesins functionally associate with CTCF on mammalian chromosome arms. *Cell* **132**:422–433.

Paulson JR, Laemmli UK. 1977. The structure of histone-depleted metaphase chromosomes. *Cell* **12**:817–828.

Piskadlo E, Tavares A, Oliveira RA. 2017. Metaphase chromosome structure is dynamically maintained by condensin I-directed DNA (de)catenation. *Elife* **6**. doi:10.7554/eLife.26120

Rao SSP, Huang S-C, Glenn St Hilaire B, Engreitz JM, Perez EM, Kieffer-Kwon K-R, Sanborn AL, Johnstone SE, Bascom GD, Bochkov ID, Huang X, Shamim MS, Shin J, Turner D, Ye

Z, Omer AD, Robinson JT, Schlick T, Bernstein BE, Casellas R, Lander ES, Aiden EL. 2017. Cohesin Loss Eliminates All Loop Domains. *Cell* **171**:305–320.e24.

Rao SSP, Huntley MH, Durand NC, Stamenova EK, Bochkov ID, Robinson JT, Sanborn AL, Machol I, Omer AD, Lander ES, Aiden EL. 2014. A 3D map of the human genome at kilobase resolution reveals principles of chromatin looping. *Cell* **159**:1665–1680.

Riggs AD. 1990. DNA methylation and late replication probably aid cell memory, and type I DNA reeling could aid chromosome folding and enhancer function. *Philos Trans R Soc Lond B Biol Sci* **326**:285–297.

Rubio ED, Reiss DJ, Welcsh PL, Disteche CM, Filippova GN, Baliga NS, Aebersold R, Ranish JA, Krumm A. 2008. CTCF physically links cohesin to chromatin. *Proc Natl Acad Sci U S A* **105**:8309–8314.

Sakai Y, Mochizuki A, Kinoshita K, Hirano T, Tachikawa M. 2018. Modeling the functions of condensin in chromosome shaping and segregation. *PLoS Comput Biol* **14**:e1006152.

Sakai Y, Tachikawa M, Mochizuki A. 2016. Controlling segregation speed of entangled polymers by the shapes: A simple model for eukaryotic chromosome segregation. *Phys Rev E* **94**:042403.

Saka Y, Sutani T, Yamashita Y, Saitoh S, Takeuchi M, Nakaseko Y, Yanagida M. 1994. Fission yeast cut3 and cut14, members of a ubiquitous protein family, are required for chromosome condensation and segregation in mitosis. *EMBO J* **13**:4938–4952.

Sanborn AL, Rao SSP, Huang S-C, Durand NC, Huntley MH, Jewett AI, Bochkov ID, Chinnappan D, Cutkosky A, Li J, Geeting KP, Gnirke A, Melnikov A, McKenna D, Stamenova EK, Lander ES, Aiden EL. 2015. Chromatin extrusion explains key features of loop and domain formation in wild-type and engineered genomes. *Proc Natl Acad Sci U S A* **112**:E6456–65.

Schoenfelder S, Fraser P. 2019. Long-range enhancer–promoter contacts in gene expression control. *Nat Rev Genet* **20**:437–455.

Schwarzer W, Abdennur N, Goloborodko A, Pekowska A, Fudenberg G, Loe-Mie Y, Fonseca NA, Huber W, H Haering C, Mirny L, Spitz F. 2017. Two independent modes of chromatin organization revealed by cohesin removal. *Nature* **551**:51–56.

Seitan VC, Faure AJ, Zhan Y, McCord RP, Lajoie BR, Ing-Simmons E, Lenhard B, Giorgetti L, Heard E, Fisher AG, Flicek P, Dekker J, Merkenschlager M. 2013. Cohesin-based chromatin interactions enable regulated gene expression within preexisting architectural compartments. *Genome Res* **23**:2066–2077.

Sen N, Leonard J, Torres R, Garcia-Luis J, Palou-Marin G, Aragón L. 2016. Physical Proximity of Sister Chromatids Promotes Top2-Dependent Intertwining. *Mol Cell* **64**:134–147.

Sexton T, Yaffe E, Kenigsberg E, Bantignies F, Leblanc B, Hoichman M, Parrinello H, Tanay A, Cavalli G. 2012. Three-dimensional folding and functional organization principles of the Drosophila genome. *Cell* **148**:458–472.

Sheiko SS, Borisov OV, Prokhorova SA, Möller M. 2004. Cylindrical molecular brushes under poor solvent conditions: microscopic observation and scaling analysis. *Eur Phys J E Soft Matter* **13**:125–131.

Shintomi K, Inoue F, Watanabe H, Ohsumi K, Ohsugi M, Hirano T. 2017. Mitotic chromosome assembly despite nucleosome depletion in Xenopus egg extracts. *Science* **356**:1284–1287.

Shintomi K, Takahashi TS, Hirano T. 2015. Reconstitution of mitotic chromatids with a minimum set of purified factors. *Nat Cell Biol* **17**:1014–1023.

Sofueva S, Yaffe E, Chan W, Georgopoulou D, Rudan MV, Mira‐Bontenbal H, Pollard SM, Schroth GP, Tanay A, Hadjur S. 2013. Cohesin‐mediated interactions organize chromosomal domain architecture. *EMBO J* **32**:3119–3129.

Steffensen S, Coelho PA, Cobbe N, Vass S, Costa M, Hassan B, Prokopenko SN, Bellen H, Heck MM, Sunkel CE. 2001. A role for Drosophila SMC4 in the resolution of sister chromatids in mitosis. *Curr Biol* **11**:295–307.

Stigler J, Çamdere GÖ, Koshland DE, Greene EC. 2016. Single-Molecule Imaging Reveals a Collapsed Conformational State for DNA-Bound Cohesin. *Cell Rep* **15**:988–998.

Strunnikov AV, Hogan E, Koshland D. 1995. SMC2, a Saccharomyces cerevisiae gene essential for chromosome segregation and condensation, defines a subgroup within the SMC family. *Genes Dev* **9**:587–599.

Sullivan NL, Marquis KA, Rudner DZ. 2009. Recruitment of SMC by ParB-parS organizes the origin region and promotes efficient chromosome segregation. *Cell* **137**:697–707.

Sumner AT. 1991. Scanning electron microscopy of mammalian chromosomes from prophase to telophase. *Chromosoma* **100**:410–418.

Takemoto A, Kimura K, Yokoyama S, Hanaoka F. 2004. Cell cycle-dependent phosphorylation, nuclear localization, and activation of human condensin. *J Biol Chem* **279**:4551–4559.

Terakawa T, Bisht S, Eeftens JM, Dekker C, Haering CH, Greene EC. 2017. The condensin complex is a mechanochemical motor that translocates along DNA. *Science* **358**:672–676.

Tran NT, Laub MT, Le TBK. 2017. SMC Progressively Aligns Chromosomal Arms in Caulobacter crescentus but Is Antagonized by Convergent Transcription. *Cell Rep* **20**:2057–2071.

Trask BJ, Allen S, Massa H, Fertitta A, Sachs R, van den Engh G, Wu M. 1993. Studies of metaphase and interphase chromosomes using fluorescence in situ hybridization. *Cold Spring Harb Symp Quant Biol* **58**:767–775.

Traut TW. 1994. Physiological concentrations of purines and pyrimidines. *Mol Cell Biochem* **140**:1–22.

Umbarger MA, Toro E, Wright MA, Porreca GJ, Baù D, Hong S-H, Fero MJ, Zhu LJ, Marti-Renom MA, McAdams HH, Shapiro L, Dekker J, Church GM. 2011. The three-dimensional architecture of a bacterial genome and its alteration by genetic perturbation. *Mol Cell* **44**:252–264.

Vian L, Pękowska A, Rao SSP, Kieffer-Kwon K-R, Jung S, Baranello L, Huang S-C, El Khattabi L, Dose M, Pruett N, Sanborn AL, Canela A, Maman Y, Oksanen A, Resch W, Li X, Lee B, Kovalchuk AL, Tang Z, Nelson S, Di Pierro M, Cheng RR, Machol I, St Hilaire BG, Durand NC, Shamim MS, Stamenova EK, Onuchic JN, Ruan Y, Nussenzweig A, Levens D, Aiden EL, Casellas R. 2018. The Energetics and Physiological Impact of Cohesin Extrusion. *Cell* **173**:1165–1178.e20.

Vietri Rudan M, Barrington C, Henderson S, Ernst C, Odom DT, Tanay A, Hadjur S. 2015. Comparative Hi-C reveals that CTCF underlies evolution of chromosomal domain architecture. *Cell Rep* **10**:1297–1309.

Walther N, Hossain MJ, Politi AZ, Koch B, Kueblbeck M, Ødegård-Fougner Ø, Lampe M, Ellenberg J. 2018. A quantitative map of human Condensins provides new insights into mitotic chromosome architecture. *J Cell Biol* **217**:2309–2328.

Wang X, Brandão HB, Le TBK, Laub MT, Rudner DZ. 2017. Bacillus subtilis SMC complexes juxtapose chromosome arms as they travel from origin to terminus. *Science* **355**:524–527.

Wang X, Hughes AC, Brandão HB, Walker B, Lierz C, Cochran JC, Oakley MG, Kruse AC, Rudner DZ. 2018. In Vivo Evidence for ATPase-Dependent DNA Translocation by the Bacillus subtilis SMC Condensin Complex. *Mol Cell* **71**:841–847.e5.

Wang X, Le TBK, Lajoie BR, Dekker J, Laub MT, Rudner DZ. 2015. Condensin promotes the juxtaposition of DNA flanking its loading site in Bacillus subtilis. *Genes Dev* **29**:1661–1675.

Wang X, Montero Llopis P, Rudner DZ. 2013. Organization and segregation of bacterial chromosomes. *Nat Rev Genet* **14**:191–203.

Wang X, Tang OW, Riley EP, Rudner DZ. 2014. The SMC condensin complex is required for origin segregation in Bacillus subtilis. *Curr Biol* **24**:287–292.

Wendt KS, Yoshida K, Itoh T, Bando M, Koch B, Schirghuber E, Tsutsumi S, Nagae G, Ishihara K, Mishiro T, Yahata K, Imamoto F, Aburatani H, Nakao M, Imamoto N, Maeshima K, Shirahige K, Peters J-M. 2008. Cohesin mediates transcriptional insulation by CCCTC-binding factor. *Nature* **451**:796–801.

Wilhelm L, Bürmann F, Minnen A, Shin H-C, Toseland CP, Oh B-H, Gruber S. 2015. SMC condensin entraps chromosomal DNA by an ATP hydrolysis dependent loading mechanism in Bacillus subtilis. *Elife* **4**. doi:10.7554/eLife.06659

Woodward J, Taylor GC, Soares DC, Boyle S, Sie D, Read D, Chathoth K, Vukovic M, Tarrats N, Jamieson D, Campbell KJ, Blyth K, Acosta JC, Ylstra B, Arends MJ, Kranc KR, Jackson AP, Bickmore WA, Wood AJ. 2016. Condensin II mutation causes T-cell lymphoma through tissue-specific genome instability. *Genes Dev* **30**:2173–2186.

Wutz G, Várnai C, Nagasaka K, Cisneros DA, Stocsits RR, Tang W, Schoenfelder S, Jessberger G, Muhar M, Hossain MJ, Walther N, Koch B, Kueblbeck M, Ellenberg J, Zuber J, Fraser P, Peters J-M. 2017. Topologically associating domains and chromatin loops depend on cohesin and are regulated by CTCF, WAPL, and PDS5 proteins. *EMBO J* **36**:3573–3599.

Yamamoto T, Schiessel H. 2017. Osmotic mechanism of the loop extrusion process. *Phys Rev E* **96**:030402.

Zawadzka K, Zawadzki P, Baker R, Rajasekar KV, Wagner F, Sherratt DJ, Arciszewska LK. 2018. MukB ATPases are regulated independently by the N- and C-terminal domains of MukF kleisin. *Elife* **7**:e31522.

Zhang N, Kuznetsov SG, Sharan SK, Li K, Rao PH, Pati D. 2008. A handcuff model for the cohesin complex. *J Cell Biol* **183**:1019–1031.

Supplementary Figures

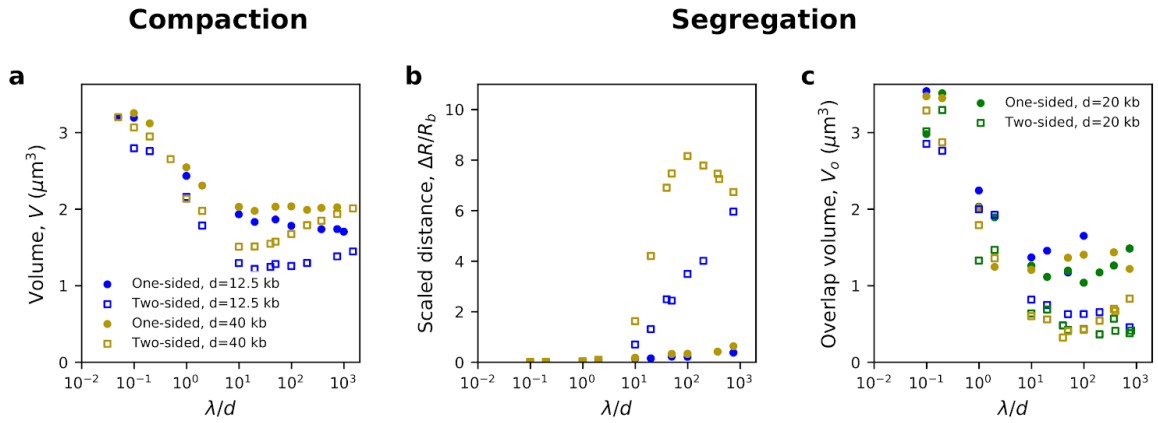

Figure 2 - figure supplement 1. Measures of compaction and segregation with different densities of LEFs. **(a)** Volumetric compaction of individual chromosomes and **(b)** scaled distance between the backbones of sister chromatids are shown for one-sided and two-sided extrusion (filled circles and open squares, respectively) with LEF densities of 1 per 12.5 kb (blue) and 1 per 40 kb (gold). **(c)** Sister chromatid overlap volume is shown as a supplementary measure of chromatid resolution. Overlap volume decreases with as *λ/d* increases, but the decrease in volume is limited for chromatids compacted by one-sided extrusion (filled circles) as compared to those compacted by two-sided extrusion (open square).

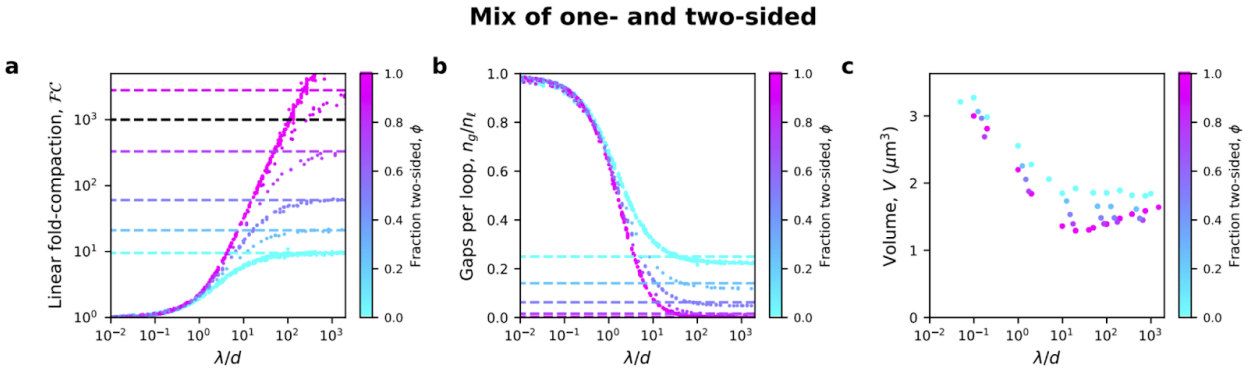

Figure 2 - figure supplement 2. Compaction in model with a mix of one- and two-sided LEFs. **(a)** Strong linear compaction can only be achieved with a high fraction of two-sided LEFs. Colored dashed lines show prediction from mean-field theory (Banigan and Mirny, 2019) for compaction in the limit of large *λ/d,* while black dashed line indicates *FC*=1000, expected for human chromosomes. **(b)** Gaps remain in systems with a one-sided LEFs, as quantified by the number of gaps per loop, n_g/n_l. Dashed lines indicate the expected number of gaps per loop. **(c)** Volumetric compaction for different fractions of two-sided extrusion.

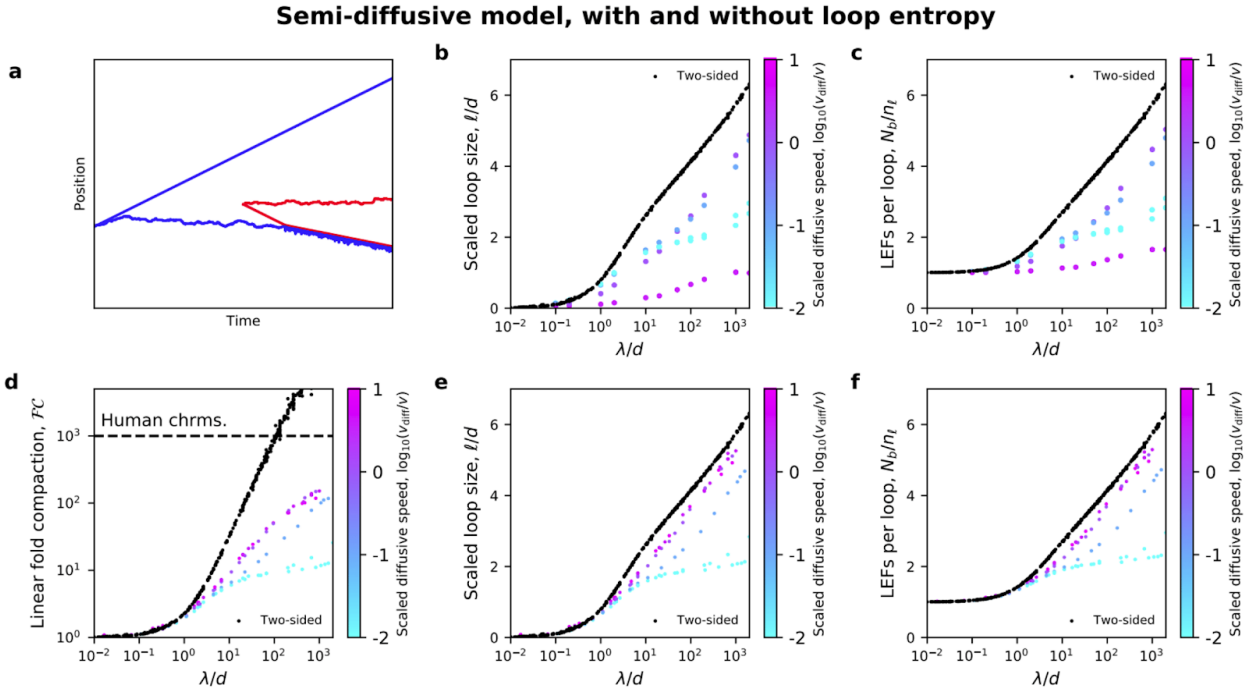

Figure 2 - figure supplement 3. Loop sizes and LEF nesting explain the ineffectiveness of the semi-diffusive model. **(a)** Example trajectory of a semi-diffusive LEF (blue) that is ratcheted open by another LEF (red) that binds within the extruded loop. **(b)** Mean loop sizes, ℓ, are small in the semi-diffusive model because loop growth is opposed by entropy. **(c)** Consequently, the number of LEFs per loop, which quantifies LEF nesting, remains small. **(d)** In a semi-diffusive model that ignores the effects of polymer conformational entropy, a higher degree of linear compaction, *FC*, can be obtained, but *FC*<1000 for λ/d<1000. **(e)** This can occur due to the growth of larger loops, which **(f)** facilitates LEF nesting, and thus Brownian ratcheting. Two-sided extrusion data is shown in black in (b)-(f) for comparison.

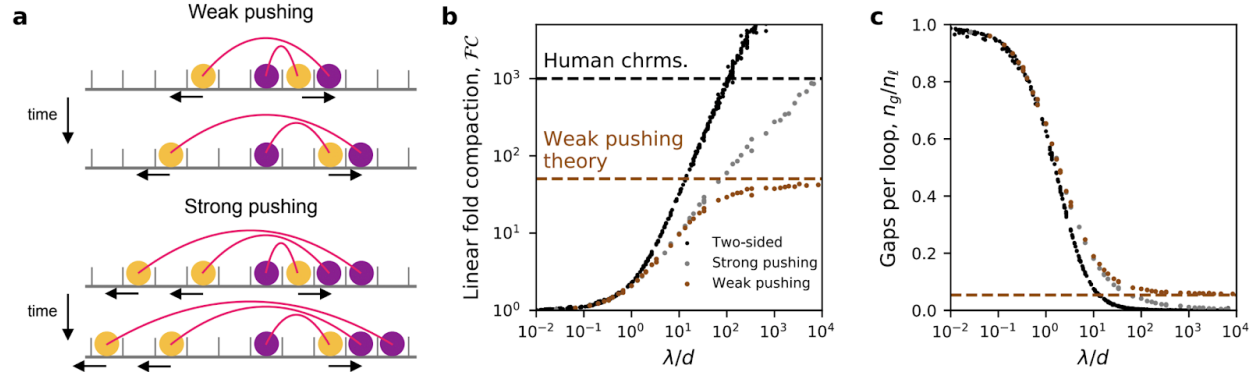

Figure 2 - figure supplement 4. Models in which the active subunits of nested LEFs can push passive LEF subunits. **(a)** Cartoon arch diagrams of “weak” and “strong” pushing models (top two and bottom two panels, respectively). One-sided LEFs are composed of active subunits

(yellow) connected to passive subunits (purple); active subunits translocate in the direction indicated by the arrow along the chromatin polymer (gray), shown as a series of discrete sites. In the weak pushing model, an active LEF subunit can only push a single passive LEF subunit. In the strong pushing model, an active LEF subunit can simultaneously push multiple consecutive passive LEF subunits. See Supplemental File 1 for more details. **(b)** Fold linear compaction shown for the two-sided model (black), the strong pushing model (gray), and the weak pushing model (brown). Purple and brown dashed lines indicate large λ/d predictions from mean-field theory for one-sided and weak pushing models, respectively. **(c)** Number of gaps per loop for the two-sided, strong pushing model, and weak pushing models, with brown dashed line showing mean-field prediction for the weak pushing model.

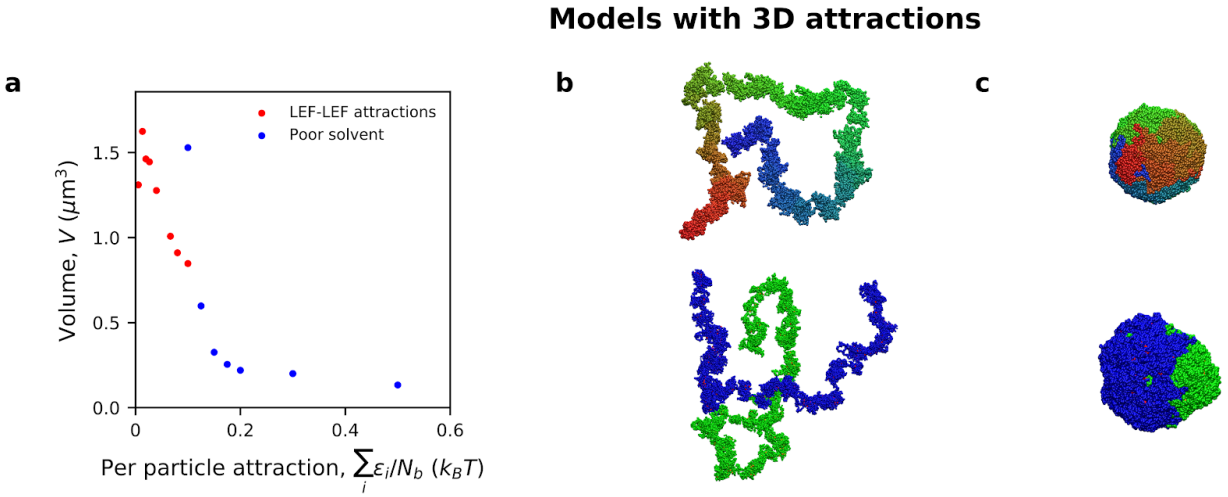

Figure 2 - figure supplement 5. Defective compaction and segregation with 3D attractive interactions. **(a)** Volumetric compaction plotted as a function of average attraction energy per monomer, for simulations with LEF-LEF attractive interactions (red) and attractive interactions between all monomers (*i.e.*, poor solvent conditions; blue). **(b)** Simulation images of chromosome compaction (top) and sister chromatid resolution (bottom) in simulations with LEF-LEF attractions. **(c)** Simulations images of chromosome compaction (top) and sister chromatid resolution (bottom) in simulations with poor solvent.

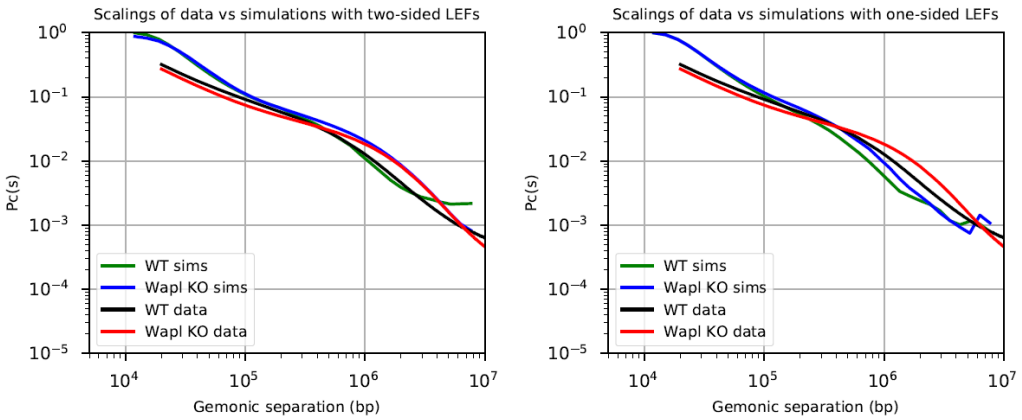

Figure 3 - figure supplement 1. Contact probability as a function of genomic separation (scalings) of data (Haarhuis et al., 2017) and simulations, with on the left simulations of two-sided extrusion and on the right for one-sided extrusion. We use the scalings to determine the values of λ and d that best match experimental observations. The simulations that are used in the main text for WT and Wapl KO conditions are shown in the middle panels, with 1 monomer = 2 kb. The parameter values for WT simulations are λ=d=200 kb and for Wapl KO simulations λ=2 Mb, d=200 kb.

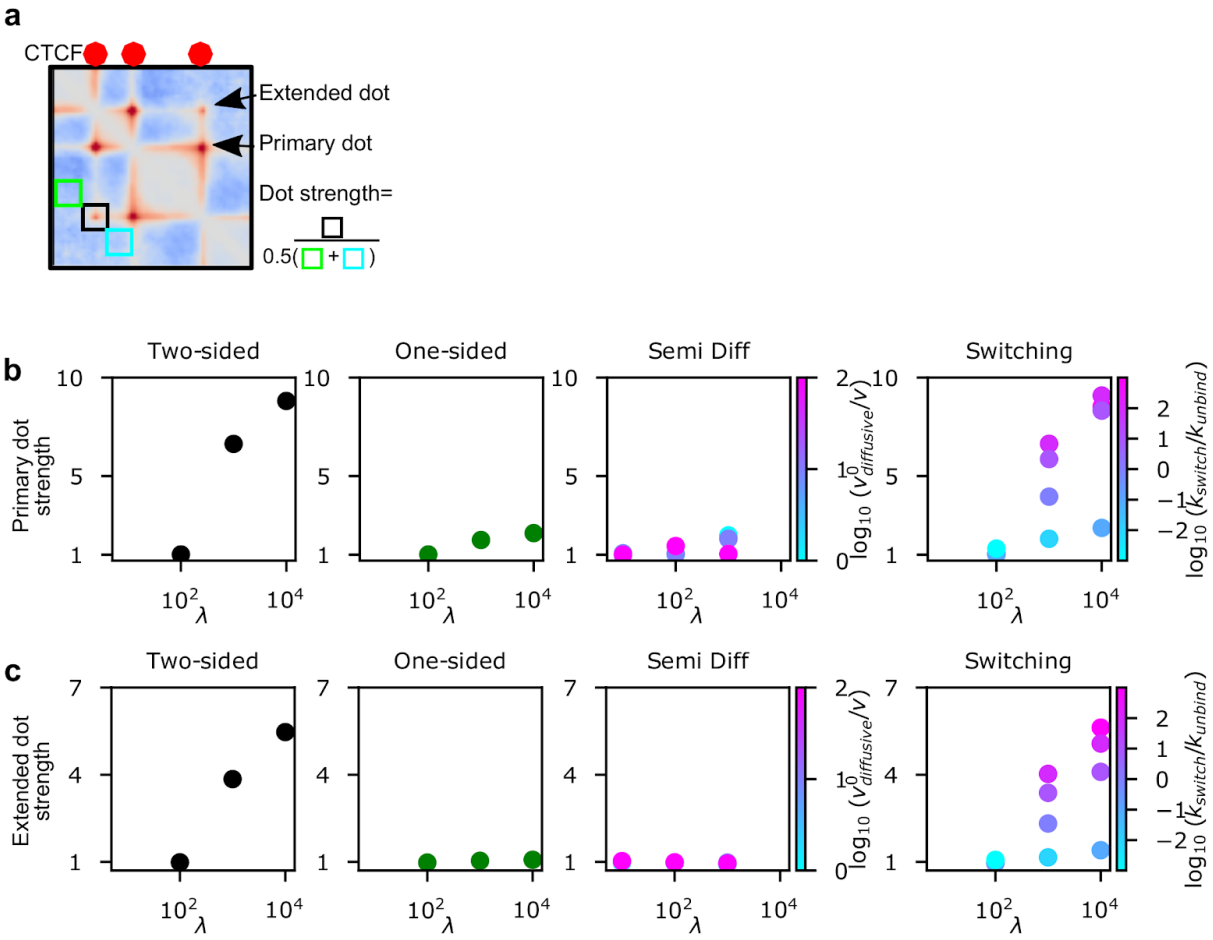

Figure 3 - figure supplement 2. **(a)** The definition of dot strength and primary and secondary dots. The divergent color scale of the contact map emphasizes that dot strengths are computed on contact maps after computing observed-over-expected (**Methods**). **(b)** Strength of primary dots for for increasing processivity at a constant LEF separation, d=200 kb. **(c)** Strength of extended dots for increasing processivity at a constant LEF separation, d=200 kb.

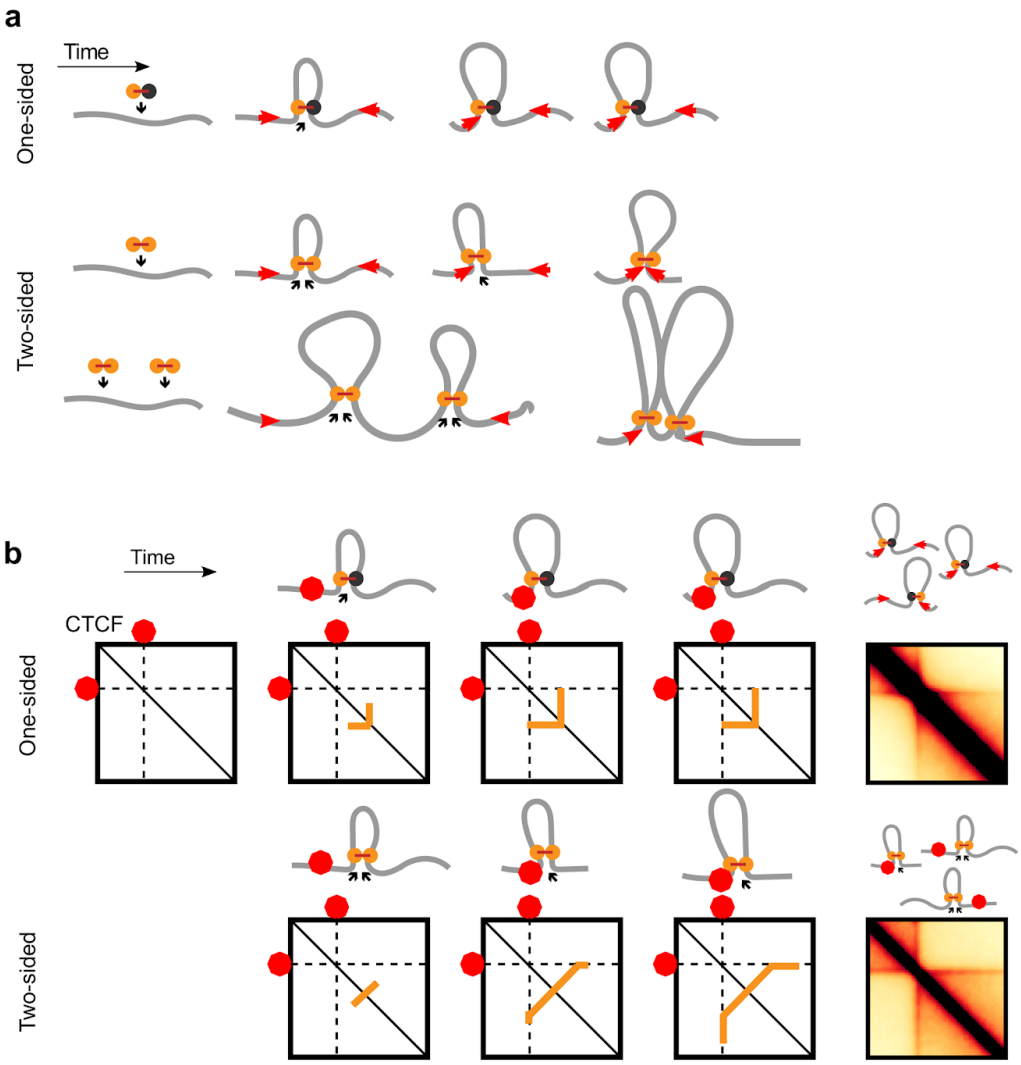

Figure 3 - figure supplement 3. **(a)** One-sided LEFs leave a gap between the passive LEF subunit and a barrier, unless they are loaded at a barrier (top row). Two-sided LEFs, on the other hand, can pair barriers while loading between barriers in two possible ways; a single two-sided LEF can pair two barriers (middle row), or barriers can be paired through the collective extrusion of multiple LEFs (bottom row). **(b)** Illustration of stripe formation by one- and two-sided LEFs.

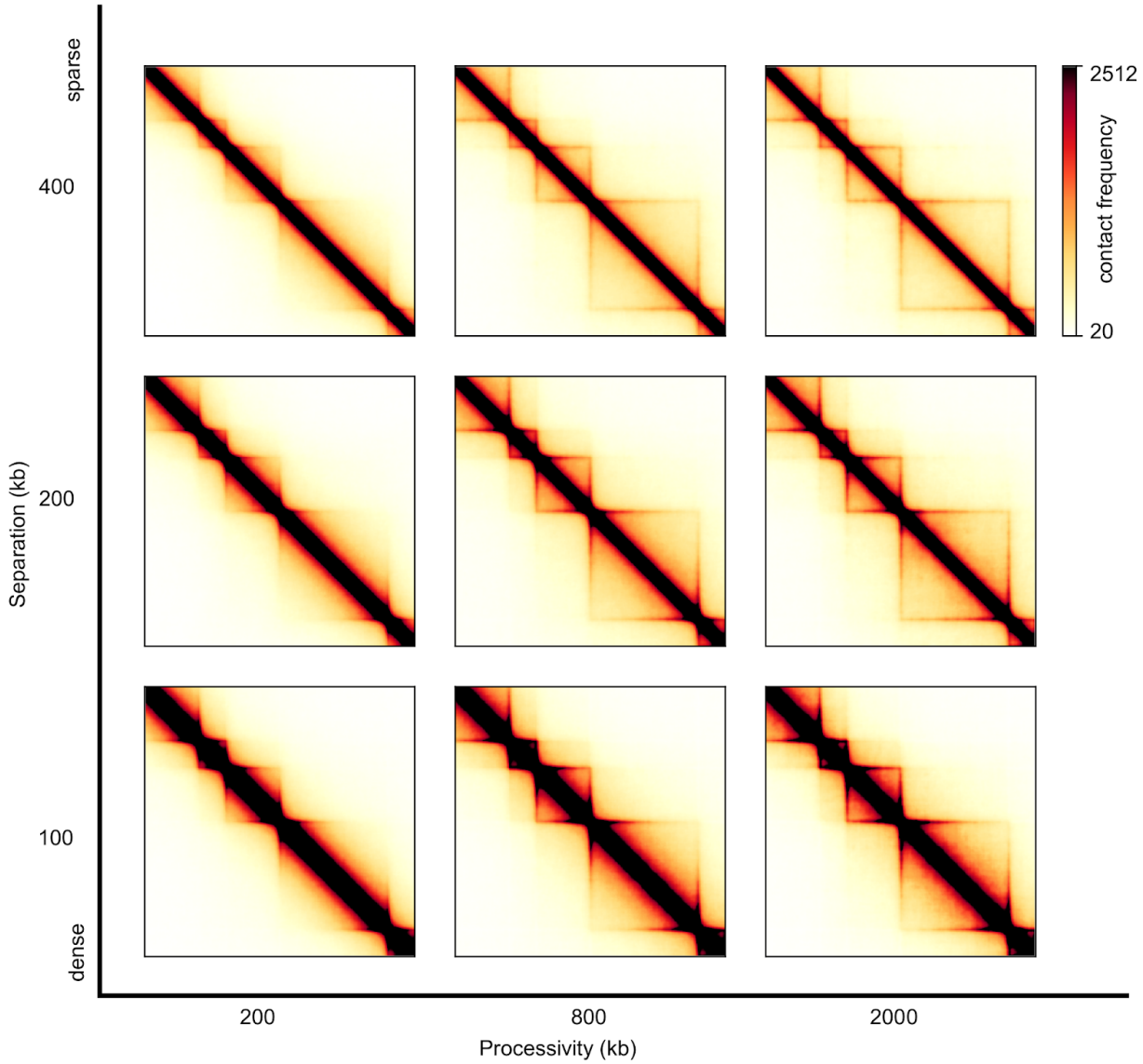

Figure 3 - figure supplement 4. Sweep of the separation between LEFs, *d*, and the processivity of LEFs, for one-sided LEFs. A processivity of λ=100 gives scalings that best match wild-type conditions, while a processivity of λ=1000 results in scalings that best match Wapl KO conditions (**Figure 3 figure supplement 1**).

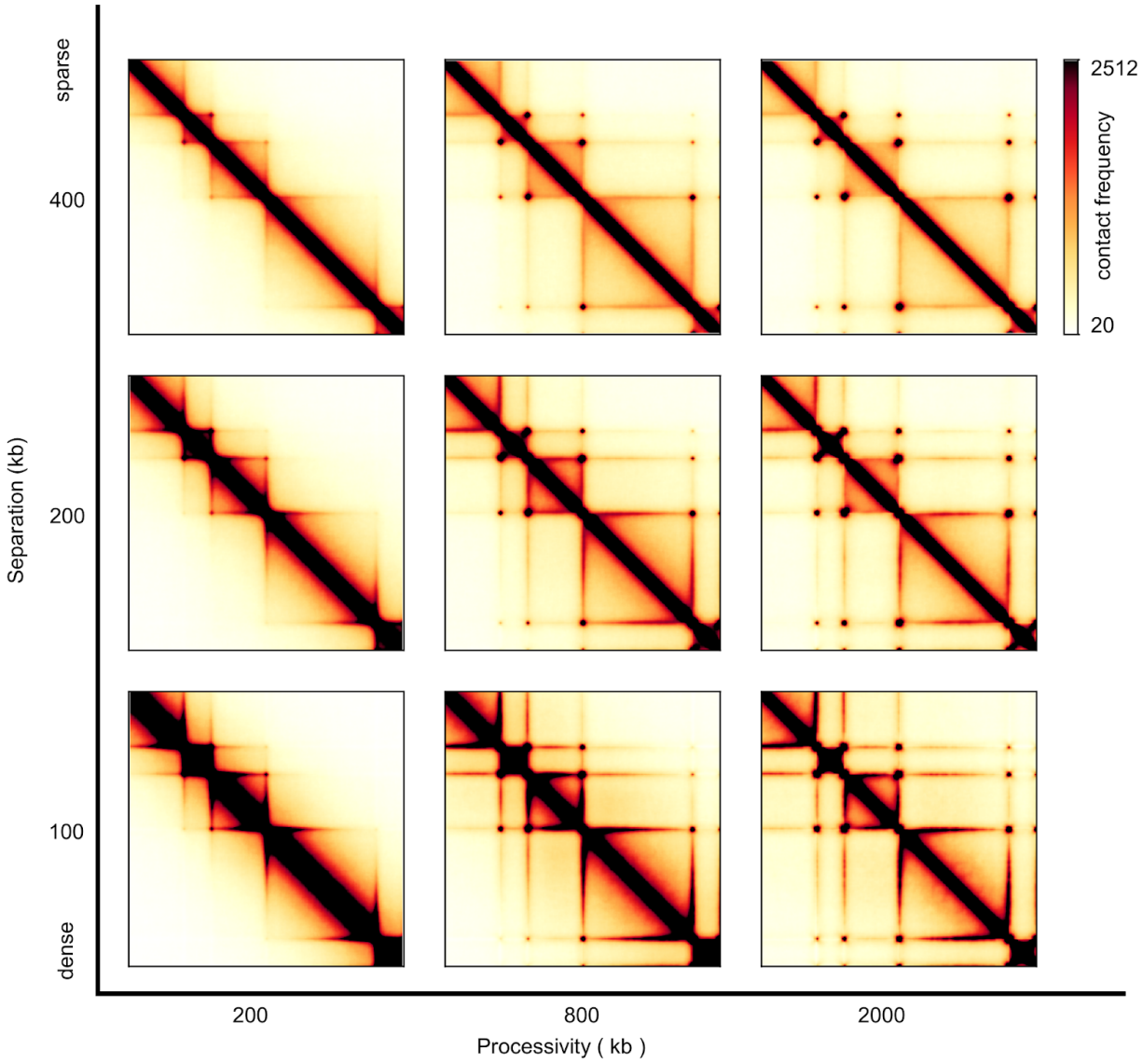

Figure 3 - figure supplement 5. Sweep of the separation between LEFs, *d*, and the processivity of LEFs, *λ*, for two-sided LEFs

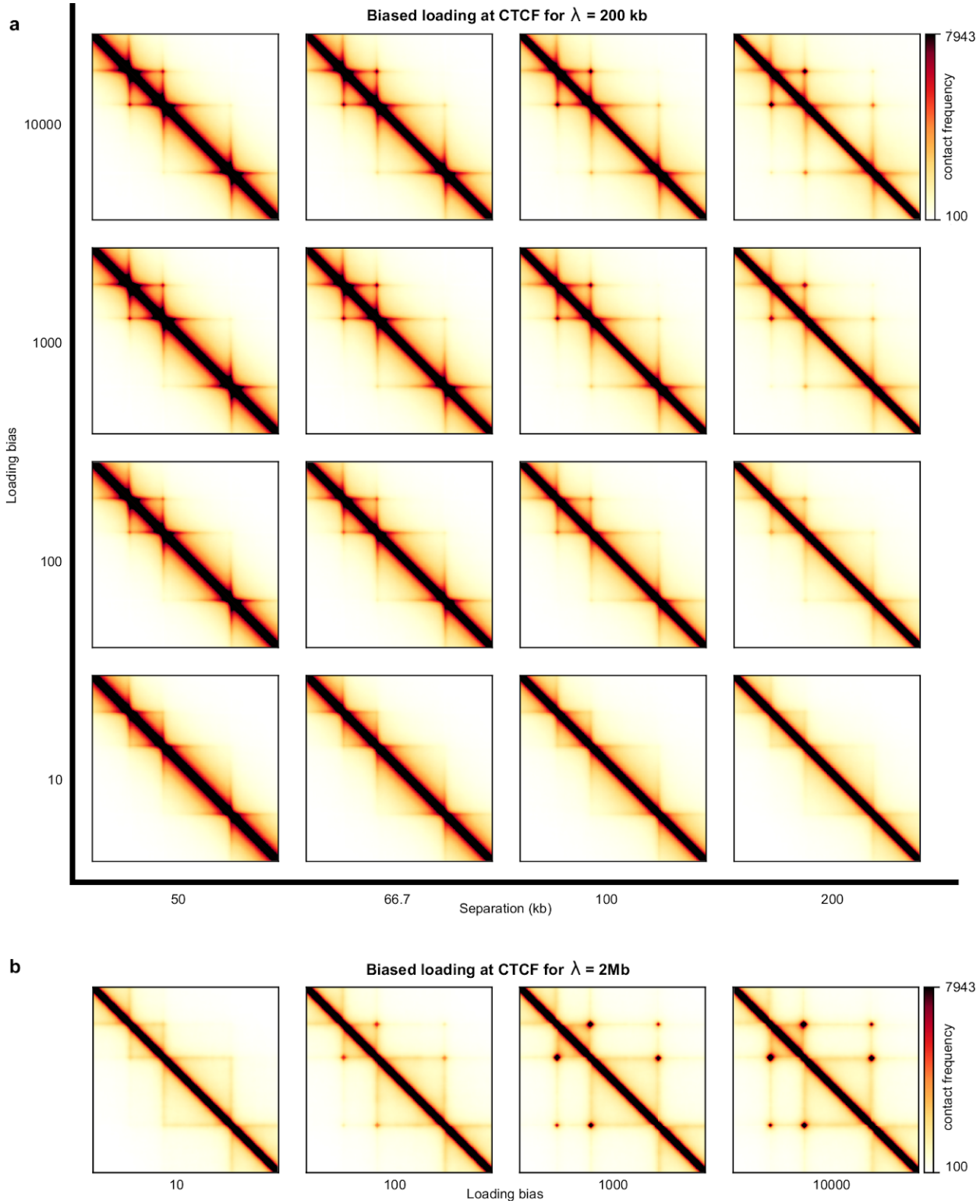

Figure 3 - figure supplement 6. **(a)** Sweep of the separation between LEFs, *d*, for one-sided extruders that load 1000 times more likely at a CTCF site as compared to an arbitrary site within the TAD, where each CTCF site has two loading sites. For the smallest TAD (which consists of 100 monomers, 200 kb), this loading bias implies that at most 95% of all LEFs loads at a

boundary. For the largest TAD (which has a size of 200 monomers, 400 kb), at most 90% of the LEFs loads at a boundary. Note that, once a boundary occupied, a LEF is forced to load somewhere else, therefore we only give an upper estimate for the fraction of LEFs loaded at a boundary. The processivity λ=200 kb for all panels. **(b)** Sweep of the loading bias for λ=2 Mb.

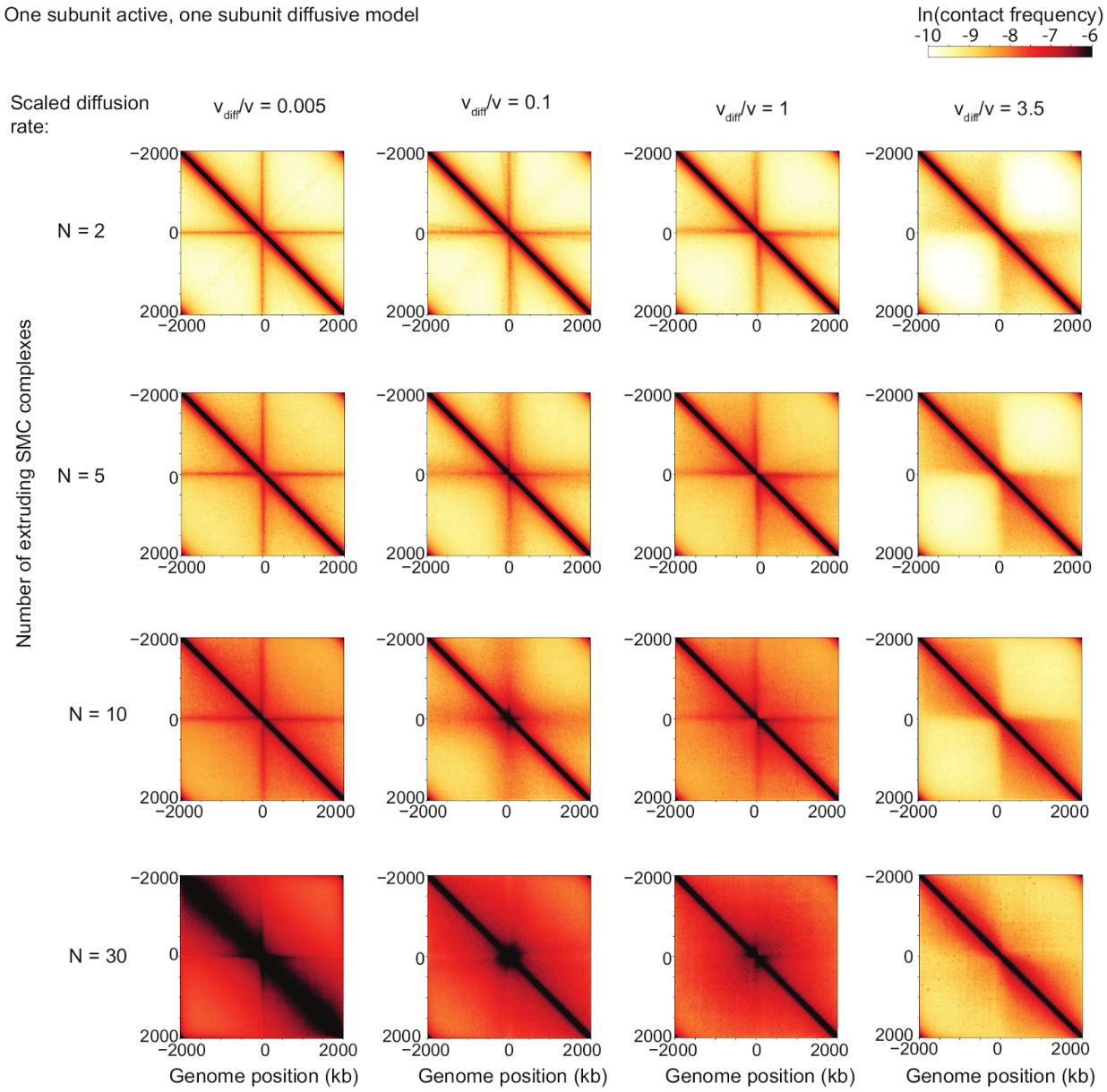

Figure 4 - figure supplement 1. Sweep of the diffusive stepping rate and the number of LEFs for bacterial chromosomes. Scaled diffusive stepping rate increases from left to right, and number of LEFs (i.e. extruding SMC complexes) increases from top to bottom.

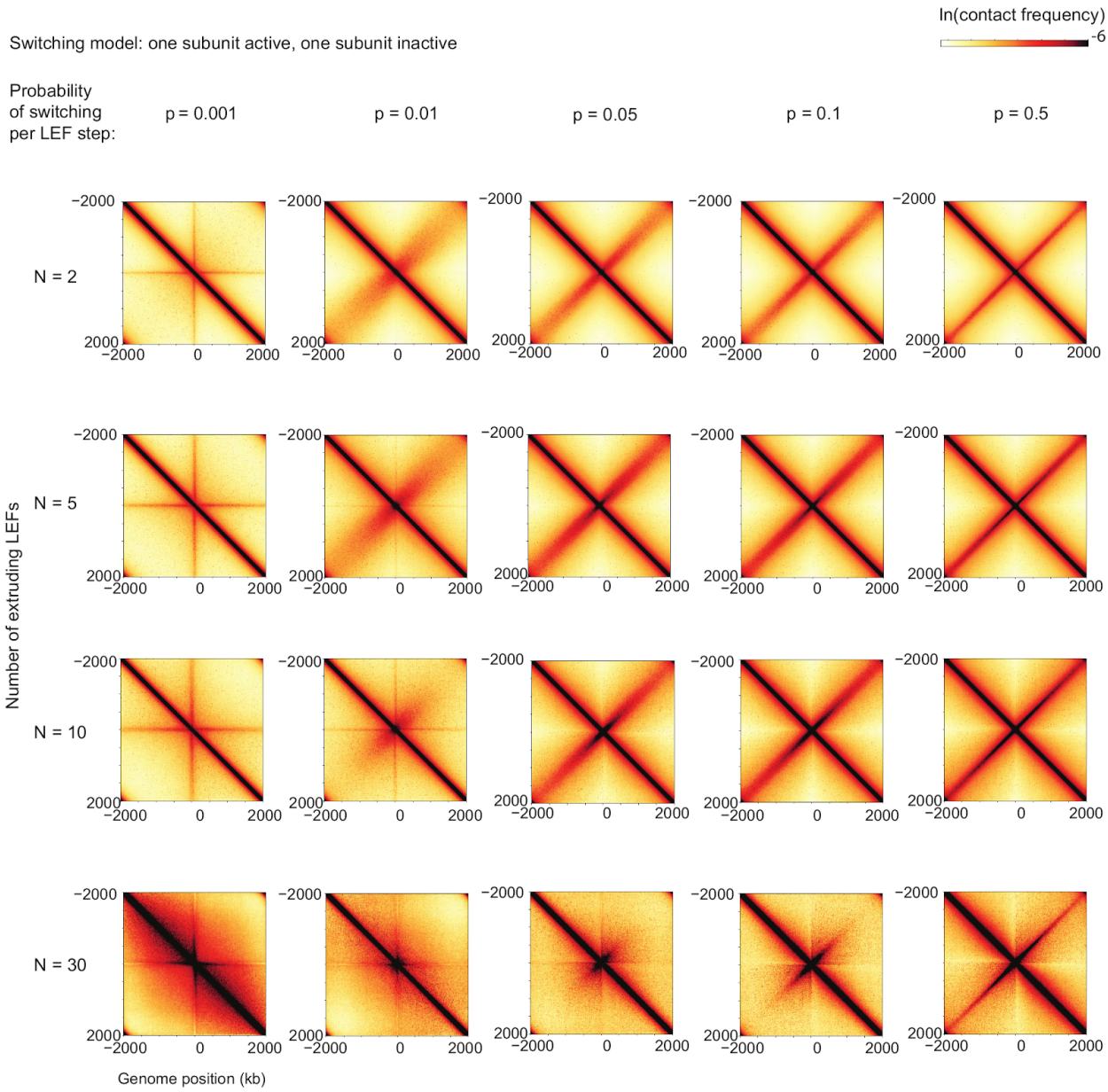

Figure 4 - figure supplement 2. Contact maps from simulations for scaled switching rates and numbers of LEFs for bacterial chromosomes. Switching probability per active translocation step increases from left to right and number of LEFs increases from top to bottom. Note that switching probabilities are given in simulation step units; from left to right, these correspond to units of $k_{switch}L/v$ of 4, 40, 200, 400, 2000; in units of switching rate, k_{switch}, from left to right these correspond to 0.001 s^{-1}, 0.01 s^{-1}, 0.05 s^{-1}, 0.1 s^{-1} and 0.5 s^{-1} for *B. subtilis.*

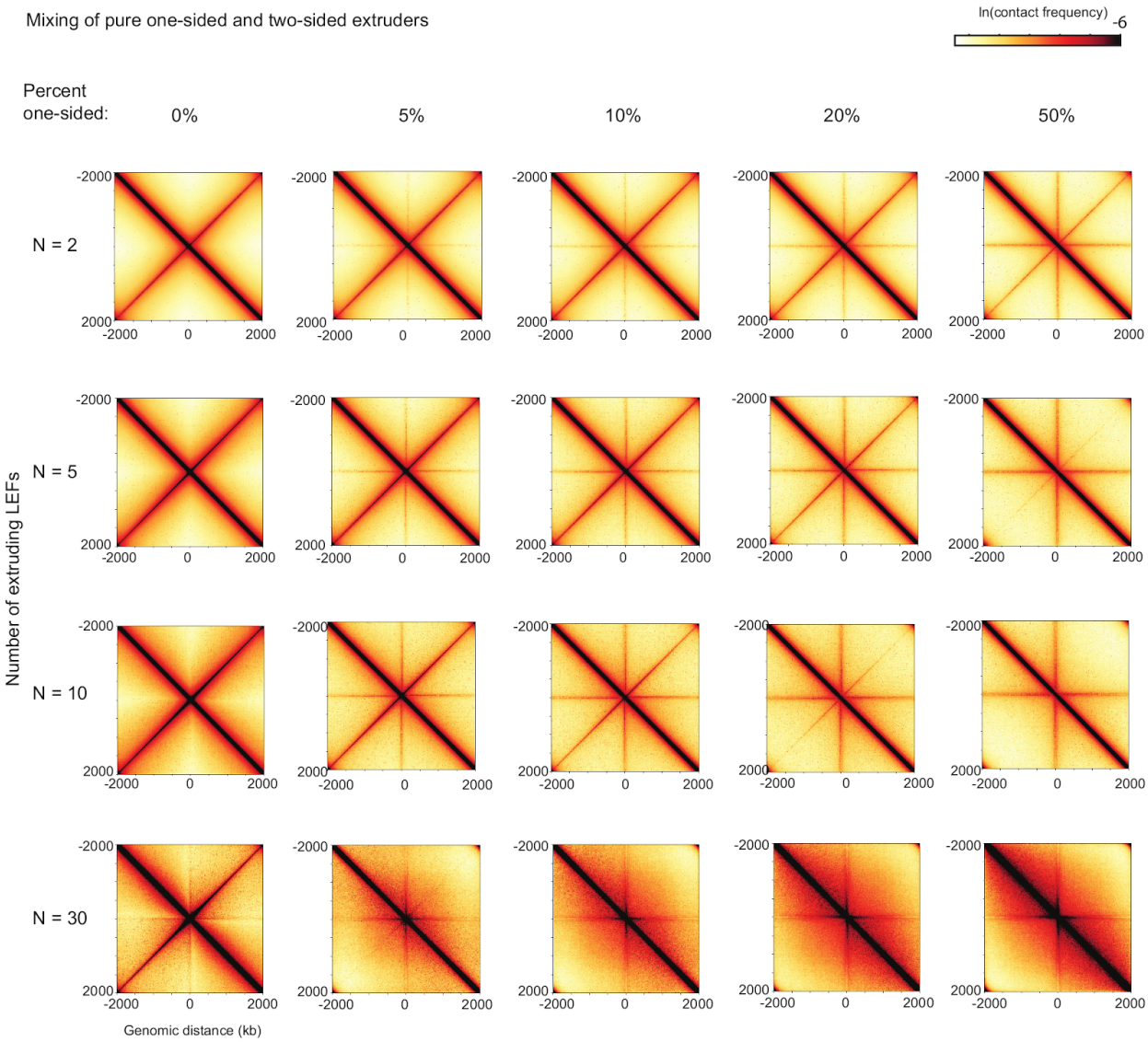

Figure 4 - figure supplement 3. Contact maps from simulations for different mixes of one- and two-sided LEFs and numbers of LEFs for bacterial chromosomes. Fraction of one-sided LEFs increases from left to right, with 0% indicating the case of pure two-sided extrusion. Number of LEFs increases from top to bottom. Note that in these simulations, each LEF is designated as either one- or two-sided each time it is loaded onto the chromosome.

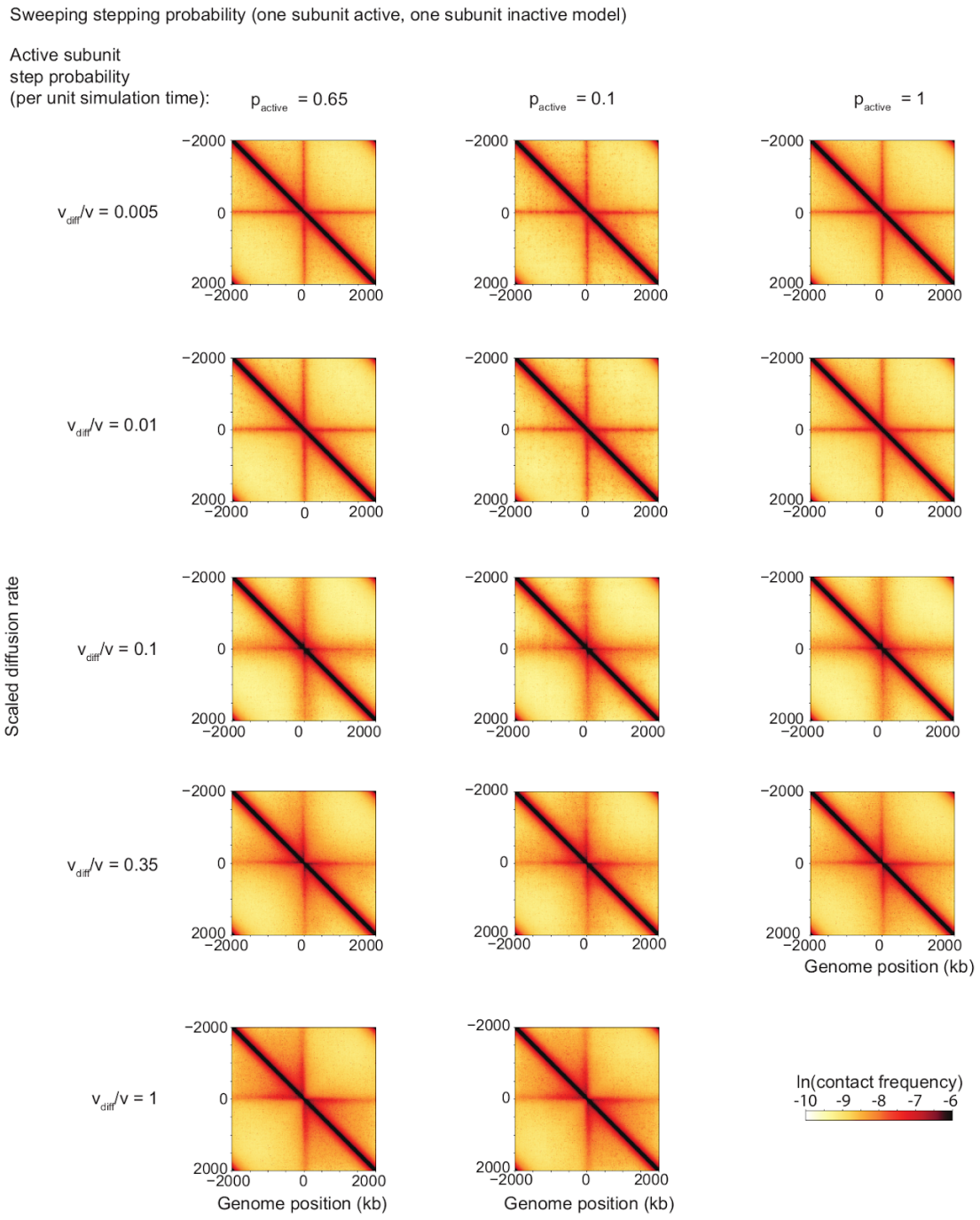

Figure 4 - figure supplement 4. Contact maps from simulations for different values of the LEF stepping probability per simulation step, with *N*=5 LEFs on each chromosome. These results indicate that the scaled diffusion rate, v_{diff}/v is the invariant quantity giving the contact maps their shape in the case of the model of a semi-diffusive LEF.

Chromosome organization by one-sided and two-sided loop extrusion: Supplemental File 1

Edward J. Banigan*, Aafke A. van den Berg*, Hugo B. Brandão*,
John F. Marko, and Leonid A. Mirny

October 22, 2019

*These authors contributed equally

Contents

1 LEF pushing models

1.1 Descriptions of the "strong" and "weak" pushing models

We consider two variations of "pushing" models, in which passive subunits of a loop-extruding factor (LEF) may be pushed by the active subunit of another LEF. As in the other one-sided extrusion models, LEFs are comprised of one active subunit and one passive subunit. When an active subunit of the first LEF encounters a passive subunit, the active subunit may continue translocation by forcing the passive subunit off of its chromatin polymer lattice site and onto the adjacent site, in the direction of active translocation. In the "weak" pushing model, an active subunit can push a single passive subunit onto adjacent unoccupied sites (Figure 2 - figure supplement 4 a, top). In the "strong" pushing model, if multiple passive subunits are adjacent to each other, an active subunit behind the consecutive chain of adjacent passive subunits may directionally push the passive subunits, provided that there is an unoccupied site at the other end of the chain (Figure 2 - figure supplement 4 a, top).

1.2 Mean-field theoretical calculation for the weak pushing model

Using the mean-field theory previously developed for loop extrusion in the limit of large λ/d [1], we can calculate the maximum attainable linear fold compaction in the weak pushing model (there is no compaction limit for the strong pushing model, because all gaps can be closed for sufficiently large λ/d). Specifically, this calculation assumes that the processivity, λ, is large ($\lambda \gg d$) and the system is in steady state. To determine the fraction, f, of chromatin that is compacted into loops, we must determine the frequency of gaps, which remain if adjacent LEFs are divergently oriented (*i.e.*, $\leftarrow\rightarrow$). As described below, we may then compute the equivalent fraction of LEFs that are effectively two-sided, and thus, the associated maximum attainable linear fold compaction.

1.2.1 Review of mean-field theory for loop extrusion

In the pure one-sided model, there is one gap for every four loops, which leads to the equation:

$$N_p \ell + \frac{N_p}{4} g = L, \tag{1}$$

where N_p is the number of parent LEFs (*i.e.*, LEFs found at the bases of chromatin loops), ℓ is the mean length of a loop, $g = d$ is the mean gap size, and L is the length of the chromatin polymer.

Two additional equations will be needed to solve the weak pushing model. From Eq. 1, we can write:

$$f = \frac{4\ell}{4\ell + g} = 1 - \frac{N_p}{4(N_p + N_c)}, \tag{2}$$

where N_c is the total number of nested child LEFs. In addition, by solving the equations for the steady-state binding/unbinding kinetics of LEFs, we find:

$$N_c = \frac{f - \alpha}{1 - f} N_p, \tag{3}$$

where α is the fraction of parent LEFs that have a child LEF nested within.

From these equations, as described in [1] we find $f = (3 + 4\ln 4)/(4 + 4\ln 4) = 0.895$. Since linear fold compaction is defined as:

$$\mathcal{FC} = \frac{1}{1 - f}, \tag{4}$$

we have $FC \approx 10$.

The theory can be extended to compute linear compaction for systems that include two-sided or effectively two-sided LEFs. If a fraction, ϕ, of LEFs are (effectively) two-sided, Eq. 1, relating loops, gaps, and polymer length becomes:

$$N_p \ell + \frac{N_p (1 - \phi)^2}{4} g = L. \tag{5}$$

The maximum fraction compacted is then given by:

$$f = \frac{3 + 2\phi - \phi^2 + 4\ln(4(1-\phi)^{-2})}{4 + 4\ln(4(1-\phi)^{-2})}. \tag{6}$$

1.2.2 Application of mean-field theory to the weak pushing model

In the weak pushing model, some gaps left by one-sided extrusion may be closed if at least one of the two "parent" LEFs adjacent to the gap has a nested "child" LEF that is oriented so that its active subunit translocates toward the passive subunit of the parent LEF. To compute the fraction compacted, f, we modify Eq. 1 to properly describe the frequency of unlooped gaps along the chromosome because some gaps may be closed by nested child LEFs.

We begin by computing the probability that a particular gap will be closed by a nested LEF. Because we consider a "weak" pushing model in which an active subunit may only push a single passive subunit (Figure 2 - figure supplement 4 a, top), we only need to consider the top level of LEF nesting. Each parent LEF has a probability α of having a nested child LEF. The child LEF has a 50% chance of being oriented so that it actively extrudes toward the passive subunit of the parent LEF. This configuration closes unlooped gaps. Thus, each LEF in a *potentially* gapped configuration does not close the gap with probability $1-\alpha/2$. Since each potential gap is bordered by two parent LEFs, we have the following equation for gaps and loops:

$$N_p\ell + \frac{N_p}{4}(1-\alpha/2)^2 g = L. \tag{7}$$

Paralleling the analysis in [1], we can rewrite this equation as:

$$f = 1 - \frac{N_p}{4(1-\alpha/2)^{-2}(N_p + N_c)}, \tag{8}$$

and use Eq. 3 to find $\alpha = 2(2\sqrt{3} - 3) = 0.928$. By substituting into Eq. 7 and comparing to Eq. 5, we find that weak pushing corresponds to an effective two-sided fraction of $\phi = 2\sqrt{3} - 3 = 0.464$. This leaves an average of $n_g/n_\ell = (1/4)(1-\alpha/2)^2 = 0.072$ gaps per loop (Figure 2 - figure supplement 4 c, brown dashed line). Substituting into Eq. 6, we find:

$$f = \frac{\text{arccosh}7 + 4\sqrt{3} - 6}{1 + \text{arccosh}7} = 0.980, \tag{9}$$

which corresponds to $\mathcal{FC} = 51$-fold linear compaction (Figure 2 - figure supplement 4 b, brown dashed line).

2 Linear compaction by LEFs that can traverse each other

In the main text, we considered a model in which LEFs may traverse each other, *i.e.*, they do not act as barriers to each other. This is one possible many-LEF theoretical model for the Z-loops observed in [2]. We may compute linear compaction, $\mathcal{FC}$, as defined in Eq. 4, by computing the fraction of chromatin that is extruded into loops. Since LEFs are essentially invisible to each other in this model, we may compute loop coverage by randomly placing loops of size λ (the processivity) on a polymer of length L. We will first compute the fraction of the polymer that is not extruded into loops and then subtract this result from 1.

First consider a randomly chosen loop on the polymer and a random infinitesimal region of length du. The probability that this infinitesimal region is not covered by the particular loop $p = (L-\lambda)/L$. Since LEF (and thus, loop) positions are independent of each other in this model, the probability that the region du is not covered by *any* of the N loops is p^N. Integrating over the entire polymer, we find the total average uncovered length:

$$\langle u \rangle = \int_0^L du \left(\frac{L-\lambda}{L}\right)^N = L\left(\frac{L-\lambda}{L}\right)^N. \tag{10}$$

Therefore, the fraction extruded into loops is:

$$f = 1 - \frac{\langle u \rangle}{L} = 1 - \left(\frac{L-\lambda}{L}\right)^N = 1 - e^{-\lambda N/L}. \tag{11}$$

Using Eq. 4 and noting that $d = L/N$, fold compaction grows exponentially with λ/d:

$$\mathcal{FC} = (1 - f)^{-1} = e^{\lambda/d}. \tag{12}$$

1000-fold linear compaction in this model is achieved for $\lambda/d = 6.9$.

3 Generating Hi-C-like contact maps analytically

We devised a method of quickly generating Hi-C-like contact maps assuming the polymer is an equilibrium Gaussian chain. Contact maps can be rapidly generated from a list of SMC complex positions. This analytical method allows us to generate Hi-C-like maps quickly, circumventing the need to perform a more computationally intensive 3D Brownian or molecular dynamics (MD) polymer simulation. In Fig. 1, we provide an overview of the method for calculating contact probability between two genome loci. We treat the cases in which SMC complexes do not form pseudoknots and SMC-mediated physical contacts between two monomers of the polymer chain have a root-mean-squared distance similar to the monomer length. To compute Hi-C-like contact maps, we compute the effective genomic distance between any two points on the chain. The effective distance is the harmonic mean of the two shortest paths that can be taken between the two points within a looped segment (see Fig. 1). We present our findings in the context of generating bacterial Hi-C maps, and we validate the method by direct comparison to an MD simulation of a 3D polymer.

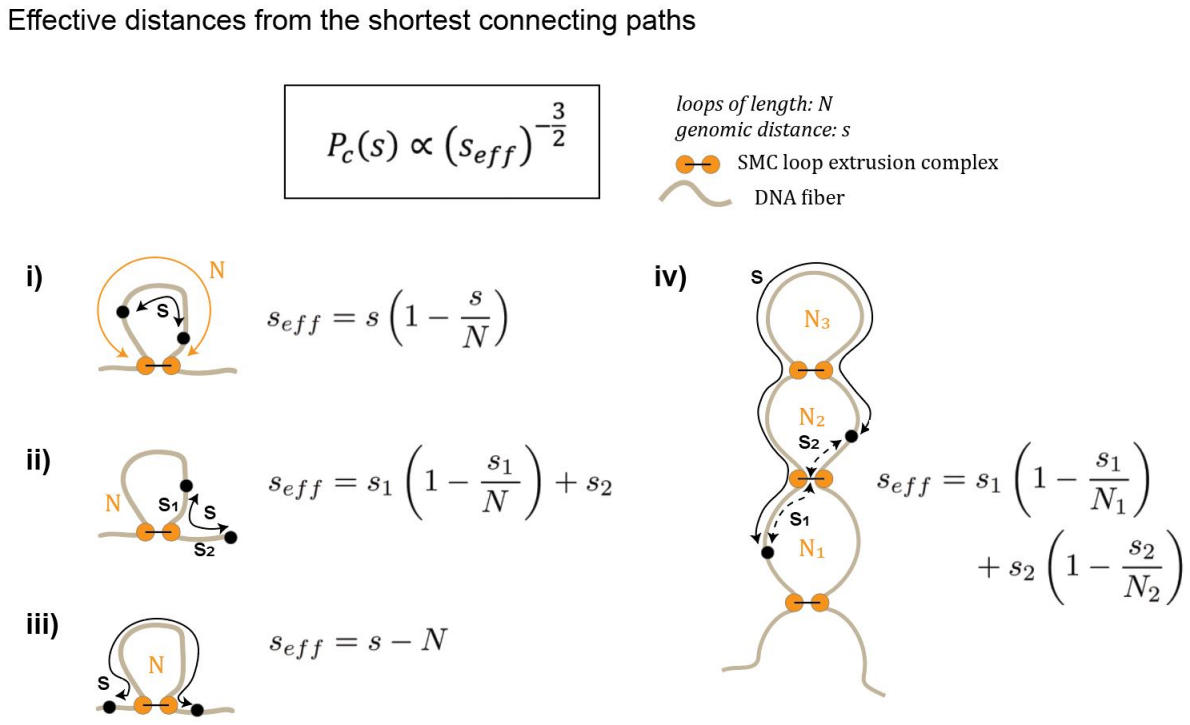

Figure 1: Generating Gaussian chain contact maps analytically from loop configurations. The contact probability $P_c(s)$ is calculated by converting the true genomic distance, s, to its effective genomic distance s_{eff}. For example, in (i), the effective genomic distance is simply harmonic mean distance between the two paths in a loop (*i.e.*, $s_{\text{eff}} = \left(\frac{1}{s} + \frac{1}{N-s}\right)^{-1} = s\left(1 - \frac{s}{N}\right)$). Diagrams (i)-(iv) schematically illustrate the types of transformations used to calculate contact probability given a loop diagram.

3.1 Contact probability of a linear chain

A Gaussian chain in one dimension with N segments of mean square length b^2, has a configurational probability density given by:

$$\begin{aligned} P(r_1, ..., r_N) &= A \exp\left(\frac{r_1^2}{2b^2}\right) \exp\left(\frac{-|r_2 - r_1|^2}{2b^2}\right) ... \exp\left(\frac{-|r_N - r_{N-1}|^2}{2b^2}\right) \\ &= A \prod_{i=1}^{N} g(r_i - r_{i-1}), \end{aligned} \tag{13}$$

where g is defined to be the Gaussian function, and r_0 is set to the origin:

$$g(r_i - r_{i-1}) r_0 = \exp\left(\frac{-|r_i - r_{i-1}|^2}{2b^2}\right); \; r_0 = 0. \tag{14}$$

The normalization factor A can be calculated by integrating over all r_i by making a change of variables:

$$A^{-1} = \int_{-\infty}^{\infty} dx_1 ... \int_{-\infty}^{\infty} dx_N \prod_{i=1}^{N} g(x_i), \tag{15}$$

$$x_i = r_i - r_{i-1} \;\; \forall i \in [1, N]. \tag{16}$$

The Jacobian of this transformation is unity, since this is an upper triangular matrix of ones on the diagonal. Thus, we get:

$$A^{-1} = \prod_{i=1}^{N} \int_{-\infty}^{\infty} dx_i \exp\left(\frac{-x_i^2}{2b^2}\right) = \left(2\pi b^2\right)^{N/2} \tag{17}$$

by using the identity:

$$\int_{-\infty}^{\infty} \exp\left(-ax^2\right) dx = \sqrt{\frac{\pi}{a}}. \tag{18}$$

To calculate the cyclization probability of the linear chain of N segments, we first calculate $P(r_N)$ and set $r_N = 0$. $P(r_N)$ is calculated by integrating over the distribution of all "internal" steps $\{r_1, ..., r_{N-1}\}$. This calculation is more easily solved using the convolution theorem and Fourier transform pairs defined by the convention below:

$$\begin{aligned} \int_{-\infty}^{\infty} g(x) g(t - x) dx &= \mathcal{F}^{-1}[\mathcal{F}(g(x)) \mathcal{F}(g(t - x))] \\ &= \mathcal{F}^{-1}[\tilde{G}(k) \cdot \tilde{G}(k)] \end{aligned} \tag{19}$$

where the Fourier transforms are defined by:

$$\begin{aligned} \mathcal{F}\left[g(x)\right] = \tilde{G}(k) &= \int_{-\infty}^{\infty} g(x) \exp\left(-ik \cdot x\right) dx \\ \mathcal{F}^{-1}\left[\tilde{G}(k)\right] &= \frac{1}{2\pi} \int_{-\infty}^{\infty} \tilde{G}(k) \exp\left(ik \cdot x\right) dk. \end{aligned} \tag{20}$$

Recognizing that $P(r_N)$ is a series of nested convolutions, we get:

$$\begin{aligned}
P(r_N) &= \int_{-\infty}^{\infty} dr_1 ... \int_{-\infty}^{\infty} dr_{N-1} P(r_1, ..., r_N) \\
A^{-1}P(r_N) &= \int_{-\infty}^{\infty} dr_1 ... \int_{-\infty}^{\infty} dr_{N-1} g(r_1)g(r_2 - r_1)...g(r_N - r_{N-1}) \\
&= \int_{-\infty}^{\infty} dr_{N-1} ... \int_{-\infty}^{\infty} \left[\int_{-\infty}^{\infty} dr_2 \left[\int_{-\infty}^{\infty} dr_1 g(r_1)g(r_2 - r_1) \right] g(r_3 - r_2) \right] ...g(r_N - r_{N-1}) \\
&= \mathcal{F}^{-1}\mathcal{F}\left[...\mathcal{F}^{-1}\left[\mathcal{F}\left[\mathcal{F}^{-1}[\mathcal{F}(g(r_1)) \cdot \mathcal{F}(g(r_2 - r_1))] \right] \mathcal{F}(g(r_3 - r_2)) \right] ... \right] \mathcal{F}\left(g(r_N - r_{N-1})\right) \\
&= \mathcal{F}^{-1}\left[\mathcal{F}(g(r_1))\mathcal{F}(g(r_2 - r_1))...\mathcal{F}(g(r_N - r_{N-1})) \right] \\
&= \mathcal{F}^{-1}\left[\tilde{G}(k)^N \right].
\end{aligned} \tag{21}$$

In the case of the Gaussian g defined above :

$$\begin{aligned}
\tilde{G}(k) &= \sqrt{2\pi b^2} \exp\left(-\frac{k^2 b^2}{2} \right) \\
\tilde{G}(k)^N &= \left(2\pi b^2\right)^{N/2} \exp\left(-\frac{N k^2 b^2}{2} \right) \\
A^{-1}P(r_N) &= \mathcal{F}^{-1}\left[\tilde{G}(k)^N \right] \\
&= \frac{1}{2\pi} \int_{-\infty}^{\infty} dk \left(2\pi b^2\right)^{N/2} \exp\left(-\frac{N k^2 b^2}{2} \right) \exp\left(ik \cdot r_N \right) \\
&= \left(2\pi b^2\right)^{N/2} \sqrt{\frac{1}{2\pi N b^2}} \exp\left(\frac{-r_N^2}{2N b^2} \right),
\end{aligned} \tag{22}$$

so,

$$P(r_N) = \sqrt{\frac{1}{2\pi N b^2}} \exp\left(\frac{-r_N^2}{2N b^2} \right). \tag{23}$$

Setting $N = s$, where s is the chain contour length in numbers of monomers, the final contact probability of a linear Gaussian chain in 1D is:

$$P_c(s) = P(r_N = 0) = \left(2\pi b^2 s\right)^{-\frac{1}{2}}, \tag{24}$$

and in 3D it is:

$$P_c(s) = \left(2\pi b^2 s\right)^{-\frac{3}{2}}. \tag{25}$$

This recovers standard results in polymer physics, and the classical $-\frac{3}{2}$ scaling coefficient for Gaussian polymer chains.

3.2 Contact probability within a loop (circular chain)

In the case of contacts within a circular chain (*i.e.*, a loop; Fig. 1 i), the chain configuration probability is built similarly, but is conditioned on the fact that the last chain segment must return to the first segment:

$$P(r_1, ..., r_N) = B \left[\prod_{i=1}^{N} g(r_i - r_{i-1}) \right] g(r_N - r_0). \tag{26}$$

Again, this equation can be solved for the normalization factor B using the Convolution Theorem and Fourier transforming procedure as above.

$$B^{-1} = \int_{-\infty}^{\infty} dr_1 ... \int_{-\infty}^{\infty} dr_{N-1} P(r_1, ..., r_N) = \frac{1}{\sqrt{N+1}} \left(2\pi b^2\right)^{N/2}. \tag{27}$$

The distance probability distribution for the s^{th} segment is given by:

$$P(r_s) = \prod_{i=1;i\neq s}^{N} \int_{-\infty}^{\infty} dr_i P(r_1, ..., r_N). \tag{28}$$

These integrals can also be solved by recognizing that we can use the Convolution Theorem separately by splitting the equation into two parts:

$$\begin{aligned} B^{-1}P(r_s) &= \left[\prod_{i=1}^{s} \int_{-\infty}^{\infty} dr_i g(r_i - r_{i-1})\right] \left[\prod_{i=s+1}^{N} \int_{-\infty}^{\infty} dr_i g(r_i - r_{i-1}) g(r_N - r_0)\right] \\ &= \mathcal{F}^{-1}\left[\mathcal{F}(g(r_1))...\mathcal{F}(g(r_s - r_{s-1}))\right] \mathcal{F}^{-1}\left[\mathcal{F}(g(r_N - r_0))...\mathcal{F}(g(r_{s+1} - r_s))\right] \\ &= \mathcal{F}^{-1}\left[\tilde{G}(k)^s\right] \mathcal{F}^{-1}\left[\tilde{G}(k)^{N-s}\right] \\ &= \left(2\pi b^2\right)^{s/2} \sqrt{\frac{1}{2\pi s b^2}} \exp\left(\frac{-r_s^2}{2sb^2}\right) \cdot \left(2\pi b^2\right)^{(N-s)/2} \sqrt{\frac{1}{2\pi(N-s)b^2}} \exp\left(\frac{-r_s^2}{2(N-s)b^2}\right) \\ &= \left(2\pi b^2\right)^{N/2} \frac{1}{2\pi b^2 \sqrt{s(N-s)}} \exp\left(-\frac{N r_s^2}{2b^2 s(N-s)}\right) \end{aligned} \tag{29}$$

So, we get for $P(r_s)$:

$$P(r_s) = \frac{\sqrt{N+1}}{2\pi b^2 \sqrt{s(N-s)}} \exp\left(-\frac{N r_s^2}{2b^2 s(N-s)}\right). \tag{30}$$

Thus, the contact probability of the s^{th} segment (in 1D) is:

$$P_c = P(r_s = 0) = \frac{1}{2\pi b^2} \frac{\sqrt{N+1}}{\sqrt{s(N-s)}}. \tag{31}$$

In 3D, the solution is:

$$P_c = P(r_s = 0)^3 = \left(\frac{\sqrt{N+1}}{2\pi b^2 \sqrt{s(N-s)}}\right)^3 \approx \left(\frac{1}{2\pi b^2 \sqrt{s(1-s/N)}}\right)^3 = \left(\frac{1}{2\pi b^2 \sqrt{s_{\text{eff}}}}\right)^3. \tag{32}$$

Interestingly, the genomic distance s is replaced by the harmonic mean of the two paths within the loop. We can thus define an effective genomic distance s_{eff} as $s_{\text{eff}} = s\,(1 - s/N)$.

3.3 Contact probability between a loop and a linear segment

For a loop (circular chain) of total length N, connected to a linear chain segment of total length L, (Fig. 1 ii) the spatial distribution (in 1D) is given by:

$$P(r, s, L, N) = C \int_{-\infty}^{\infty} dr_s P_{\text{linear}}(r - r_s, L) P_{\text{circular}}(r_s - r_0, s, N). \tag{33}$$

The solution to this equation is:

$$P(r, s, L, N) = C(2\pi)^{\frac{L}{2}-1} b^{L-2} \sqrt{\frac{N+1}{NL + s(N-s)}} e^{-\frac{Nr^2}{2b^2(NL+s(N-s))}}, \tag{34}$$

where

$$C = (2\pi)^{\frac{1}{2}-\frac{L}{2}} \sqrt{\frac{N}{N+1}} b^{1-L}. \tag{35}$$

Then, the spatial distribution is:

$$P(r, s, L, N) = \frac{1}{\sqrt{2\pi b^2}} \sqrt{\frac{1}{L + s(1 - \frac{s}{N})}} e^{-\frac{r^2}{2b^2(L+s(1-s/N))}}, \tag{36}$$

and the contact probability as a function of s, N, L (in 1D) is thus:

$$P_c(r, s, L, N) = \frac{1}{\sqrt{2\pi b^2}} \sqrt{\frac{1}{L + s(1 - \frac{s}{N})}} = \frac{1}{\sqrt{2\pi b^2}} \sqrt{\frac{1}{s_{\text{eff}}}}. \tag{37}$$

Here, the effective genomic distance $s_{\text{eff}} = L + s\,(1 - s/N)$.

3.4 Contact probability between chain segments with intervening loops

The contact probability of a chain with intervening loops (*i.e.*, loops that do not enclose the two points of interest) is simply calculated by ignoring the intervening loop. For instance, in a linear chain segment with one intervening loop of length N (Fig. 1 iii), the effective contact probability is $s_{\text{eff}} = s - N$.

3.5 Contact probability between two connected loops

For the contact probability between any two connected loops (as in Fig. 1 iv):

$$P(r, s_1, N_1, s_2, N_2) = E \int_{-\infty}^{\infty} dr_{s_1} P_{\text{circular}}(r_{s_1} - r_0, s_1, N_1) P_{\text{circular}}(r - r_{s_1}, s_2, N_2). \tag{38}$$

Similarly to the previous sections, this calculation yields:

$$P_c(s_1, N_1, r_l, L, s_2, N_2) = \frac{(2\pi b^2)^{-1/2}}{\sqrt{s_1(1 - s_1/N_1) + s_2(1 - s_2/N_2)}} = \frac{(2\pi b^2)^{-1/2}}{\sqrt{s_{\text{eff}}}} \tag{39}$$

In this case, the effective genomic distance is $s_{\text{eff}} = s_1(1 - s_1/N_1) + s_2(1 - s_2/N_2)$.

3.6 Comparing semi-analytically generated contact maps to polymer molecular dynamics

We can readily generalize the above results to any configuration of loops on a polymer chain provided that the loops do not form pseudoknots. The 3D contact probability can be calculated between any two points of the polymer chain by:

$$P_c(s_{\text{eff}}) = \left(\frac{1}{2\pi b^2}\right)^3 \left(\frac{1}{s_{\text{eff}}}\right)^{3/2}, \tag{40}$$

where s_{eff} is obtained using the rules derived above. In summary, s_{eff} is the effective shortest path between two points on the chain (computed by the sum of linear segments plus the harmonic means of "looped"/circular chain segments). The above rules can be used to calculate the "exact" looped Gaussian chain contact maps for any individual configuration of SMC complex positions on the polymer chain. However, we can better approximate a Hi-C map (which is an average over a population of cells, each with a different configuration of SMC complexes) by subsampling from the full distribution of SMC configurations. An example of a map generated from such a subsampling method (which we refer to as the semi-analytical method) is shown below, and it is compared to the contact map generated by an equivalent 3D polymer MD simulation.

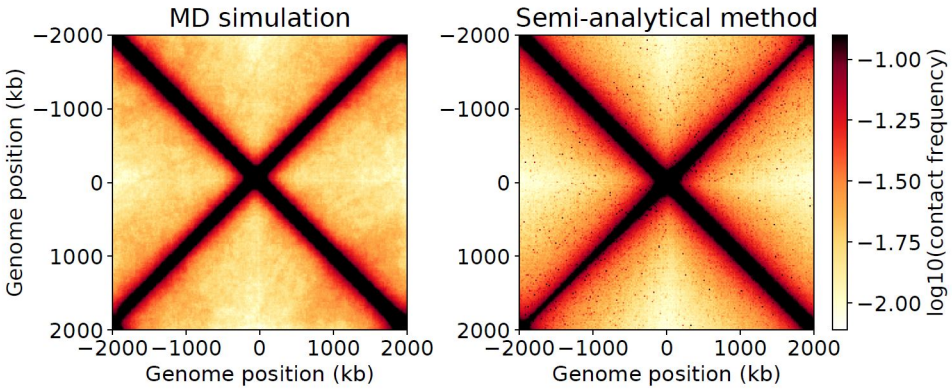

These maps were generated for a circular chromosome of length 4000 monomers (where 1 monomer = 1 kb), with a single SMC complex loading site near the *ori* (position 0 kb). A total of 10 SMC complexes were randomly loaded on the chromosome, and they performed loop extrusion as outlined in the Methods section in the main text. Contact maps were generated semi-analytically by using the SMC complex positions directly, or computed by real 3D contacts in an MD simulation with a cutoff contact-radius of 6 monomer lengths. As seen above, the two calculated maps are visually very similar.

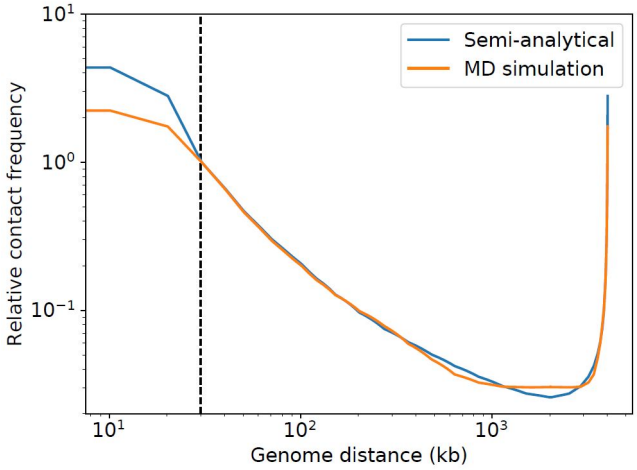

The differences between the semi-analytical and MD-simulated maps occur primarily at short genomic distances (< 30 kb), where excluded volume interactions and the 3D polymer "contact radius" play a role. However, for most of the genome, the semi-analytical and MD-simulation methods yield almost indistinguishable results for a short, bacterial chromosome as evidenced by the genome-wide contact probability curve.

References

[1] Banigan EJ and Mirny LA. 2019. Limits of chromosome compaction by loop-extruding motors. *Phys Rev X* **9**:031007.

[2] Kim E, Kerssemakers J, Shaltiel IA, Haering CH, Dekker C. 2019. DNA-loop extruding condensin complexes can traverse one another. *bioRxiv* doi:10.1101/682864.